

# Coherent Control in Cavity QED

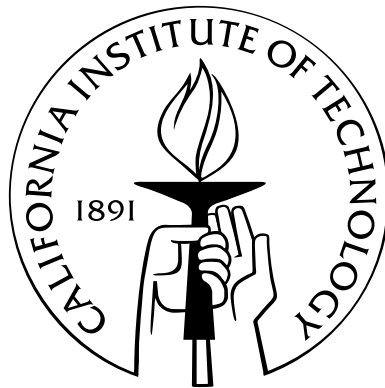
Thesis by

Tracy E. Northup

In Partial Fulfillment of the Requirements

for the Degree of

Doctor of Philosophy



California Institute of Technology

Pasadena, California

2008

(Defended May 22, 2008)

© 2008

Tracy E. Northup

All Rights Reserved

# Acknowledgements

I would first like to thank my advisor, Jeff Kimble, for the wonderful opportunities of the past six years. I am deeply grateful for the chance to work in such an exciting field, and I have learned a great deal both from him and from the diverse group of researchers he has assembled. His vision of what it means to be a scientist and his enthusiasm for pursuing challenging research problems have been an inspiring part of my education.

The strong sense of community within the Quantum Optics group has been an important part of my time at Caltech, and I would like to express my thanks to all of the group members. I have worked with an amazing set of colleagues on the cavity QED experiments: Kevin Birnbaum, Andreea Boca, David Boozer, Theresa Lynn, Russell Miller, and Dalziel Wilson. They have taught me by example how to be an experimentalist — and to have a lot of fun in the process, even on experiments that have sometimes seemed overwhelming. I want to stress that the recent achievements in lab 11 would not have been possible without Dave's insight and analysis.

Outside the lab, I am grateful to a circle of friends who have made southern California feel like home; my two Pleasant Street roommates, Mary Dunlop and Paige Randall, deserve special mention. From further distances, the support and encouragement of my parents, my brother, and Tetsu Takekoshi have always meant a great deal to me.

# Abstract

Advances in cavity quantum electrodynamics (QED) have allowed us to trap single cesium atoms within the field of a small optical resonator and to observe their strongly coupled interaction. However, in order to take advantage of this interaction as a resource for quantum information, we need to develop new techniques for control of the atom-cavity system. This thesis presents a series of experiments with the common goal of coherent control.

We have demonstrated the cooling of the center-of-mass motion of a trapped atom to its vibrational ground state along the cavity axis, and we have quantified the reversible nature of the process which maps a coherent state at the cavity input onto an atomic state. A new optical pumping method which exploits incoherent Raman transitions now allows us to prepare a trapped atom in any desired Zeeman state. I detail the technical steps which have enabled these results, including a conditional loading scheme which confirms the presence of at most one atom in the cavity. I outline our current efforts to characterize ground state population transfer via Raman transitions, which we hope will provide the basis for entanglement generation between atomic Zeeman states and photon polarization states. Two separate projects to construct new cavities and vacuum chamber systems are also discussed in the framework of future experiment design.

# Contents

<b>Acknowledgements</b>	<b>iii</b>
<b>Abstract</b>	<b>iv</b>
<b>1 Introduction</b>	<b>1</b>
1.1 A single trapped atom . . . . .	2
1.2 My history in the group . . . . .	7
1.3 Overview . . . . .	10
<b>2 Cooling to the ground state of axial motion</b>	<b>11</b>
2.1 In situ cooling: motivation and background . . . . .	11
2.2 Experimental setup . . . . .	13
2.2.1 Lasers . . . . .	14
2.2.2 Output path and detection . . . . .	18
2.2.3 Analog and digital control . . . . .	19
2.3 Demonstration of ground-state cooling . . . . .	21
2.4 Resolved second-order sideband cooling . . . . .	30
<b>3 A light-matter interface: quantifying coherence</b>	<b>33</b>
3.1 Reversible state transfer between light and a single trapped atom . . . . .	34
3.2 Pulse combinations . . . . .	43
3.3 Timing . . . . .	45
3.4 Phase stability . . . . .	47
3.5 Remote programming capabilities . . . . .	48

3.6	Mapping single photons . . . . .	49
<b>4</b>	<b>Atom preparation: optical pumping and conditional loading</b>	<b>53</b>
4.1	Optical pumping via incoherent Raman transitions . . . . .	54
4.1.1	Introduction . . . . .	55
4.1.2	Experimental apparatus . . . . .	57
4.1.3	Coherent and incoherent Raman transitions . . . . .	60
4.1.4	Measuring the population distribution . . . . .	61
4.1.5	Optical pumping scheme . . . . .	62
4.1.6	Conclusion . . . . .	65
4.1.7	Transition rate for incoherent Raman transitions . . . . .	66
4.2	Optimizing optical pumping . . . . .	69
4.3	Trapping and detecting multiple atoms . . . . .	73
4.3.1	Cavity loading . . . . .	73
4.3.2	Raman-based determination of atom number . . . . .	75
4.3.3	Simulations . . . . .	81
4.3.4	Optimizing atom loading . . . . .	82
4.3.5	Atom detection with Raman and lattice light . . . . .	85
4.4	Conditional feedback to the experiment timing . . . . .	87
<b>5</b>	<b>Toward atom-photon entanglement</b>	<b>91</b>
5.1	Atom-photon entanglement scheme . . . . .	91
5.2	Rabi flops . . . . .	94
5.2.1	Theory . . . . .	94
5.2.2	Rabi flopping measurements . . . . .	98
5.3	Zeeman to hyperfine mapping . . . . .	102
5.3.1	936 nm Raman transitions from the side of the cavity . . . . .	102
5.3.2	852 nm Raman transitions from the side of the cavity . . . . .	104
5.3.3	Raman transitions using a transverse field . . . . .	105
5.3.4	Microwave transitions . . . . .	108
5.4	Fast pulses from the side of the cavity . . . . .	110

<b>6</b>	<b>A new generation of cavities</b>	<b>116</b>
6.1	Active feedback to atomic motion . . . . .	116
6.1.1	Characterizing the active-feedback cavity . . . . .	117
6.1.2	Difficulties in implementation . . . . .	124
6.1.2.1	A nickel-plated cavity mount . . . . .	124
6.1.2.2	Complexity of the stabilization network . . . . .	125
6.1.2.3	A dearth of transits . . . . .	126
6.1.3	Technical improvements . . . . .	127
6.2	An asymmetric cavity system . . . . .	129
6.2.1	Cavity redesign . . . . .	130
6.2.2	Controlling birefringence . . . . .	132
6.2.3	Cavity length . . . . .	133
6.2.4	Rethinking passive stabilization . . . . .	134
6.2.5	Vacuum chamber . . . . .	137
6.2.6	Current project status . . . . .	141
<b>7</b>	<b>In search of the perfect mirror</b>	<b>142</b>
7.1	New mirrors for a new cavity . . . . .	142
7.2	The nuts and bolts of mirror testing . . . . .	143
7.2.1	A portable testing apparatus . . . . .	144
7.2.2	Cavity construction and alignment . . . . .	146
7.2.2.1	Reflected spots . . . . .	147
7.2.2.2	Mirror cleaning . . . . .	147
7.2.2.3	Measurement laser . . . . .	148
7.2.2.4	Cavity input power . . . . .	149
7.2.2.5	Loss partitioning . . . . .	150
7.2.2.6	Design of cavity mounts . . . . .	151
7.2.3	A simpler solution: self-locking cavity ringdown . . . . .	151
7.2.3.1	A breadboard setup for cavity-locked lasers . . . . .	152
7.2.3.2	Scattering losses in air . . . . .	154

7.3	Results of the coating runs . . . . .	155
7.3.1	REO . . . . .	155
7.3.2	ATF . . . . .	158
7.4	Single-sided cavity calculations . . . . .	159
7.5	Outlook . . . . .	162
	<b>Bibliography</b>	<b>163</b>

# List of Figures

1.1	Cavity QED coupling rates . . . . .	3
1.2	Vacuum-Rabi splitting: cavity transmission vs. probe detuning . . . . .	4
1.3	Photograph of an assembled cavity . . . . .	5
2.1	Physics cavity linewidth at Raman wavelengths . . . . .	16
2.2	Raman field nulling scan . . . . .	20
2.3	Schematic of the ground state cooling experiment . . . . .	23
2.4	State discrimination histogram . . . . .	25
2.5	Observation of red sideband suppression . . . . .	27
2.6	Variation of cooling parameters . . . . .	29
2.7	Observation of second-order sideband cooling . . . . .	31
3.1	Quantum state transfer between two systems . . . . .	35
3.2	Schematic of the reversible state transfer experiment . . . . .	37
3.3	Timing diagram . . . . .	39
3.4	Transfer probability vs. arrival time . . . . .	41
3.5	Photon generation ratios vs. relative phase . . . . .	42
3.6	Pulse generation diagram . . . . .	46
3.7	Output path to map photons back into the cavity . . . . .	50
4.1	Schematic of the optical pumping experiment . . . . .	57
4.2	Level diagram for the $D2$ line in cesium . . . . .	58
4.3	Cesium ground state spectrum in a magnetic field . . . . .	59
4.4	Raman spectrum for an unpumped initial state . . . . .	62
4.5	Power spectra of incoherent and coherent Raman signals . . . . .	63

4.6	Raman spectra for optical pumping into $ 3, 0\rangle$ and $ 3, 1\rangle$ . . . . .	64
4.7	Rate of population transfer for incoherent Raman transitions . . . . .	70
4.8	Optical pumping as a function of applied magnetic field . . . . .	72
4.9	Raman-based atom number determination: sample traces . . . . .	77
4.10	Raman-based atom number determination: histogram . . . . .	78
4.11	Fit of photon count histogram to a sum of Gaussians . . . . .	79
4.12	Photon count histograms as a function of 1 ms time bin . . . . .	80
4.13	Time evolution of the $N$ -atom populations. . . . .	81
4.14	Optimizing atom loading: beam combinations . . . . .	84
4.15	Optimizing atom loading: intensities and detunings . . . . .	85
4.16	Atom detection with Raman and lattice light: histogram . . . . .	86
4.17	Conditional loading: histogram . . . . .	89
5.1	Scheme for generation of atom-photon entanglement . . . . .	93
5.2	Rabi flops at $\Omega = 138$ kHz and $\Omega = 12.3$ kHz . . . . .	98
5.3	Ramsey interferometry . . . . .	99
5.4	Rabi flops on resonance and red-detuned . . . . .	100
5.5	Spin echo . . . . .	102
5.6	$\Delta m = \pm 1$ Raman transitions from the side of the cavity . . . . .	103
5.7	Effectiveness of optical pumping in an off-axis magnetic field . . . . .	105
5.8	Raman spectrum in an off-axis magnetic field . . . . .	106
5.9	Individual and paired Rabi flops on $ 3, 0\rangle \rightarrow  4, \pm 1\rangle$ . . . . .	107
5.10	Coherent mapping from Zeeman to hyperfine states . . . . .	108
5.11	Rabi flops using microwaves . . . . .	109
6.1	Lab 1 cavity inside the lower vacuum chamber . . . . .	117
6.2	Lower and upper vacuum chamber in lab 1 . . . . .	118
6.3	A sample “upgoer” atom transit . . . . .	119
6.4	Histogram of recorded transit arrival times . . . . .	120
6.5	Simulated distribution of transit arrival times . . . . .	121
6.6	Measured upgoer height as a function of probe intensity . . . . .	123

6.7	Mini-GAS cavity suspension mount . . . . .	136
6.8	Accelerometer measurements of the mini-GAS suspension . . . . .	137
6.9	Vacuum chamber design for a new asymmetric cavity . . . . .	138
7.1	Mirror mount assembly for test cavities . . . . .	146
7.2	Self-locking cavity ringdown setup . . . . .	153
7.3	Fraction of incident intensity reflected from an empty cavity . . . . .	161

# List of Tables

2.1	Propagation losses in the lab 11 output path . . . . .	19
3.1	Series of pulse combinations for reversible state transfer . . . . .	44
3.2	Path efficiencies in mapping a photon back into the cavity . . . . .	51
5.1	Atom-photon correlations . . . . .	113
6.1	Parameters for the lab 1 active-feedback cavity . . . . .	124
6.2	Maximum baking temperatures for vacuum chamber components . . .	140
7.1	Summary of REO coating runs . . . . .	157

# Chapter 1

## Introduction

The interaction between a single atom and the mode of an optical cavity constitutes a quantum interface between light and matter: through the coupling between the light field and the atomic dipole, the atom and cavity exchange single energy quanta. The field of cavity quantum electrodynamics (QED) is thus an exciting platform from which to explore the dynamics of fundamental quantum processes in the laboratory. Cavity QED is also an excellent candidate system for the emerging field of quantum information science [1]. In this context, the light-matter quantum interface could be harnessed to transfer information between nodes and channels of a quantum network [2]. Atoms trapped within cavities would function as “quantum nodes” where information could be processed and stored, then mapped to the output cavity mode and coupled into the “quantum channel” of an optical fiber for distribution to other nodes.

Our light-matter interface is of course also a real-world experimental system, and in order to investigate quantum processes, we need to demonstrate control over the system’s many degrees of freedom. For example, while the Jaynes-Cummings model of cavity QED [3] treats the atom as a two-level system, the cesium atoms in our laboratory have a multiplicity of hyperfine and Zeeman ground states, each of which couples differently to a cavity; in order to understand our system in terms of a simple model, we would like to prepare the atom reliably in a single ground state. An atom also possesses external degrees of freedom, which describe its center-of-mass motion within the cavity. As the cavity mode has spatial structure, the coupling of an atom

to the cavity depends upon its precise location; we would like to be able to cool the atom's vibrational motion (that is, to localize it at the antinode of a trapping potential). In the context of quantum information science, we would like to store information in two ground states of the atom, and so we need the capability to drive unitary transformations in this state space. Finally, we would like to explore the process of mapping quantum states between photons and atoms, a building block for future quantum networks.

This thesis describes recent progress in all of these directions: internal state preparation, center-of-mass ground state cooling, and a coherent mapping of photonic to atomic states.

## 1.1 A single trapped atom

The Jaynes-Cummings interaction Hamiltonian describes the coupling of a two-level atom to a single cavity mode [3]:

$$\hat{H}_{int} = \hbar g(\hat{a}^\dagger \hat{\sigma} + \hat{a} \hat{\sigma}^\dagger), \quad (1.1)$$

where  $\hat{a}^\dagger$  and  $\hat{a}$  are photon creation and annihilation operators,  $\hat{\sigma}^\dagger$  and  $\hat{\sigma}$  are atomic raising and lowering operators, and  $g$  is the (spatially dependent) coupling strength. Here we have made the rotating wave approximation, as the cavity field is near-resonant with the atomic transition. When we include terms for excitations in the atom and cavity modes as well as for a classical probe field at frequency  $\omega_p$ , then we have the Jaynes-Cummings Hamiltonian, written here in the reference frame of the probe:

$$\hat{H}_{JC} = \hbar \Delta_a \hat{\sigma}^\dagger \hat{\sigma} + \hbar \Delta_c \hat{a}^\dagger \hat{a} + \hbar g(\hat{a}^\dagger \hat{\sigma} + \hat{a} \hat{\sigma}^\dagger) + \epsilon \hat{a} + \epsilon^* \hat{a}^\dagger, \quad (1.2)$$

where  $\omega_a$  and  $\omega_c$  are the atom and cavity frequencies,  $\Delta_a = \omega_a - \omega_p$ ,  $\Delta_c = \omega_c - \omega_p$ , and  $\epsilon$  is the probe field drive strength.

In the absence of a probe ( $\omega_p = 0$ ,  $\epsilon = 0$ ), we can diagonalize this Hamiltonian to find the exact eigenstates and eigenvalues of the system. We work in the tensor

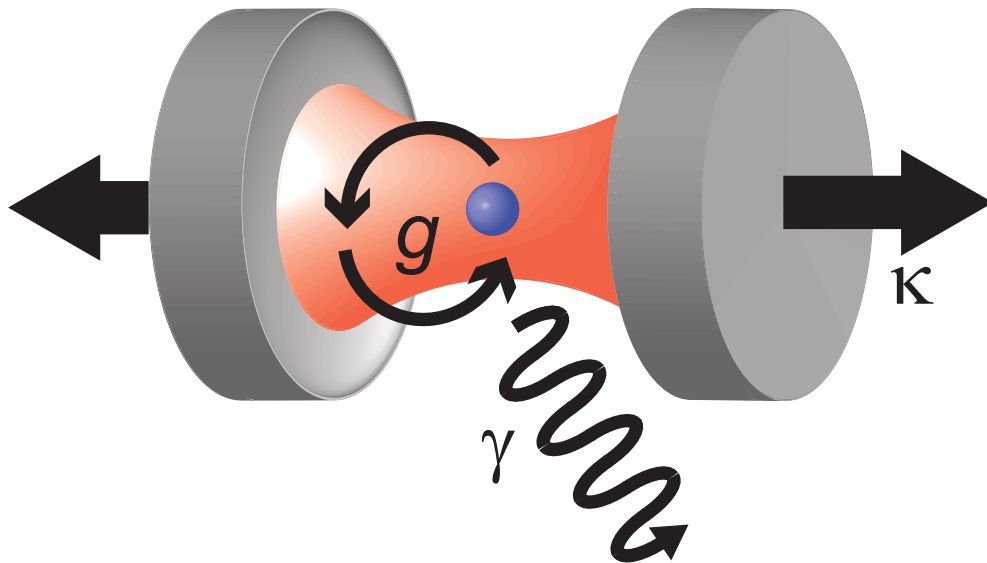


Figure 1.1: Coupling rates for a model cavity QED system. Atom and cavity couple coherently to one another at rate  $g$ . There are two incoherent mechanisms: the cavity field decays at rate  $\kappa$ , and the atom decays spontaneously at rate  $\gamma$ .

product basis where  $|g, n\rangle$  and  $|e, n-1\rangle$  are  $n$ -excitation states with an atom in the ground (excited) state and  $n$  ( $n-1$ ) photons in the cavity. The interaction term couples each pair of  $n$ -excitation states, leading to eigenstates and eigenvalues

$$|\pm_n\rangle = (\delta \pm \sqrt{4g^2n + \delta^2})|g, n\rangle + 2g\sqrt{n}|e, n-1\rangle,$$

$$E_{\pm n} = \frac{\hbar}{2}(2n\omega_c - \delta \pm \sqrt{4g^2n + \delta^2}),$$

where  $\delta = \omega_c - \omega_a$ , and  $|\pm_n\rangle$  is unnormalized. For the on-resonant case  $\delta = 0$ ,  $|\pm_n\rangle$  form the Jaynes-Cummings ladder of eigenstates, with the anharmonic dressed state splitting  $2\hbar g\sqrt{n}$  between  $E_{\pm n}$  at each rung of the ladder. A more realistic model for our system adapts the Jaynes-Cummings Hamiltonian to include multiple Zeeman and hyperfine states of the atom and two polarization modes of the cavity [4, 5].

To complete our cavity QED model, we need to include dissipation, through which the atom and cavity couple irreversibly to the environment. Dissipation can occur either through spontaneous emission, at rate  $\gamma$ , or cavity transmission, at rate  $\kappa$ . Figure 1.1 provides a schematic depiction of the three relevant coupling rates

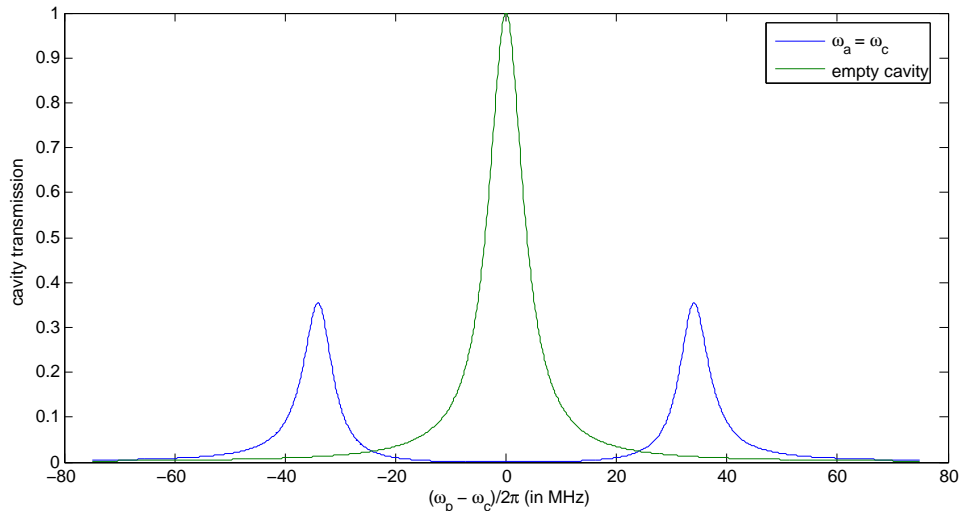


Figure 1.2: Steady-state transmission of the atom-cavity system as a function of probe detuning in the weak driving limit. Parameters are  $g = 2\pi \times 33.9$  MHz,  $\kappa = 2\pi \times 3.8$  MHz,  $\gamma = 2\pi \times 2.6$  MHz,  $\omega_a = \omega_c$ . The cavity transmission is normalized to the maximum empty cavity transmission; empty cavity transmission as a function of probe detuning is plotted for comparison.

$\{g, \kappa, \gamma\}$ . Mathematically, we can treat dissipation by incorporating the Jaynes-Cummings Hamiltonian into a master equation  $\dot{\rho} = \mathcal{L}\rho$  for the density matrix of the system, where  $\mathcal{L}$  is the Liouvillian superoperator [6]:

$$\mathcal{L} = -i[H_{JC}, \rho] + \kappa(2\hat{a}\rho\hat{a}^\dagger - \hat{a}^\dagger\hat{a}\rho - \rho\hat{a}^\dagger\hat{a}) + \gamma(2\hat{\sigma}\rho\hat{\sigma}^\dagger - \hat{\sigma}^\dagger\hat{\sigma}\rho - \rho\hat{\sigma}^\dagger\hat{\sigma}). \quad (1.3)$$

For a restricted basis set, the master equation can be solved numerically to find the steady state density matrix and expectation values of various operators. In the weak driving limit, in which the system is restricted to  $n = \{0, 1\}$ , the master equation can be solved analytically [7].

Figure 1.2 depicts the weak driving solution for the steady-state intracavity photon number, proportional to the cavity transmission, as a function of probe frequency  $\omega_p$  ( $\omega_a = \omega_c$ ) for the parameters in our current cavity QED experiment. Note that the frequencies of the two peaks correspond to the eigenvalues  $E_{\pm 1}/\hbar = \pm g$ , while the linewidth of each peak is approximately  $\frac{\kappa + \gamma}{2}$ . When  $g \gg \kappa, \gamma$ , the two-peaked structure — known as the vacuum-Rabi splitting — is well-resolved. Our experiments

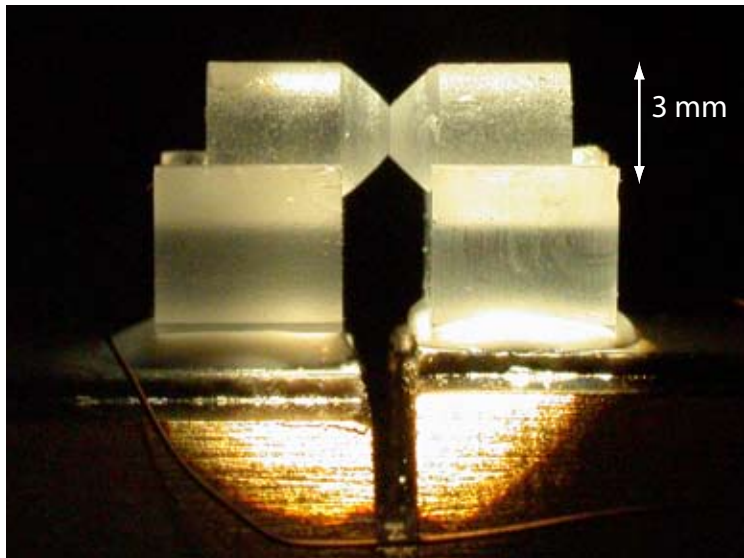


Figure 1.3: Photograph of the most recent cavity constructed for use in the lab 1 experiment. The cavity mirrors, fabricated on BK7 substrates, are only  $9.2 \mu\text{m}$  apart; the mirror faces are 1 mm in diameter, with a 10 cm radius of curvature, and coned so that they can be brought close together. The substrates are held in BK7 v-blocks glued to shear-mode piezoelectric transducers, with a copper mounting block beneath.

operate in this *strong coupling* regime, where coherent coupling dominates dissipative rates.

We construct the optical cavities that we use in the lab from high-finesse mirrors [8]; an example cavity is shown in Figure 1.3. In order to meet the strong coupling criterion, we want to maximize  $g$ , the scalar product of the atomic dipole and the electric field within the cavity:

$$g = \vec{\mu} \cdot \vec{E} = \mu \sqrt{\frac{\hbar\omega_a}{2\epsilon_0 V_m}}, \quad (1.4)$$

where  $V_m$ , the cavity mode volume, is proportional to the cavity length and to the square of the mode waist. Thus, we should minimize the mode volume by building short cavities and using mirrors with a small radius of curvature. However, the full-width half-maximum (FWHM) linewidth of a cavity is given by the ratio of its free

spectral range to finesse [9]:

$$2(\kappa/2\pi) = FWHM = \frac{FSR}{\mathcal{F}} = \frac{c}{2d\mathcal{F}}, \quad (1.5)$$

where  $d$  is the cavity length. Thus, as we build smaller cavities, the requirements on the mirror quality become increasingly stringent in order to maintain  $g \gg \kappa$ .

The cavity sits on a vibration isolation stack inside an ultra-high-vacuum (UHV) chamber. We collect  $\sim 10^6$  cold cesium atoms from background vapor in a magneto-optical trap (MOT) inside a “source” chamber, then apply an interval of polarization-gradient cooling to bring atom temperatures to around  $10 \mu\text{K}$  [10]. The atoms are released, fall under gravity through a differential pumping tube into the “cQED” chamber, and are collected a few millimeters above the cavity in a second MOT, where they undergo another stage of polarization-gradient cooling. When the atoms are released a second time, some of them fall between the cavity mirrors and transit the standing-wave cavity mode. From Figure 1.2, we see that in the strong coupling regime, the transmission of a probe laser on resonance with the empty cavity will be suppressed in the presence of a single atom. These atom signals, first observed via heterodyne detection in 1996 [11], are known in lab parlance as “downgoers” due to their shape as a function of time; the width of each dip corresponds to the time it takes the falling atom to traverse the cavity mode (tens of  $\mu\text{s}$ ). Conversely, a probe laser tuned to one of the vacuum-Rabi sidebands at  $w_p = \pm g$  would be transmitted by the cavity only in the presence of an atom, and these signals are known as “upgoers.”

In order to trap the falling atoms, a standing wave far-off-resonant trap (FORT) [10] provides a series of conservative potential wells along the cavity axis. As the atoms fall through the gap between the mirrors, they are cooled into the wells by a pair of lasers driving cesium transitions from the side of the cavity. After a brief interval, the suppression of a resonant probe laser is used to confirm the presence of a trapped atom.

A watershed in the development of cavity QED in our research group was the successful trapping of atoms initially for  $\tau \sim 30 \text{ ms}$  in 1999 [12], followed by  $\tau =$

2–3 s in the spring of 2003, where these extended lifetimes were enabled by a state-insensitive FORT at 935.6 nm [13]. In the next few years, single trapped atoms were then used to create a single-atom laser [14, 15], to generate a deterministic source of single photons [16], and to map out the vacuum Rabi splitting of a single atom [17]. Additionally, when multiple atoms were loaded into the FORT, it was possible to observe them leaving the trap one by one [18]. Meanwhile, the ability to drive coherent Raman transitions between cesium hyperfine ground states, based on ideas developed by then-graduate-student David Boozer, offered promising new prospects [19].

## 1.2 My history in the group

When I arrived at Caltech in June 2002, I joined Theresa Lynn, Kevin Birnbaum, and visiting graduate student Dominik Schrader in lab 1. At the time, the two Kimble group cavity-QED experiments were pursuing different strategies for trapping atoms within optical cavities. In lab 11, Joe Buck and Jason McKeever were cooling atoms into a FORT, struggling to improve the short trapping lifetimes demonstrated in 1999 [12]. Meanwhile in lab 1, Christina Hood and Theresa had demonstrated an “atom-cavity microscope” in which the atom’s strong coupling to the cavity field provided a trapping force [20, 21]. Theresa and Kevin now hoped to build upon this result by applying active feedback to the intracavity field in order to control the atom’s motion within the trap in real time.

Theresa and Kevin had begun a complete rebuild of the lab 1 experiment in 2000, after a series of failures in the previous system. They patiently taught me the fundamentals of experimental cavity QED as we constructed a new set of diode lasers and servos, coupled light into the new cavity, and characterized atom transits through the cavity mode. In order to control the atomic motion in real time, we planned to feed the detected signal at the cavity output into a field-programmable gate array (FPGA), which would then determine the strength of probe light at the cavity input. Unfortunately, numerical simulations carried out in parallel with our work in the

lab indicated that we would be unlikely to observe significant improvements in the lifetime of the atom in the cavity under the action of feedback [22, 23]. Moreover, the experimental system itself presented unforeseen technical challenges. After Theresa’s graduation in 2003, Kevin and I worked together on the feedback experiment through the fall of 2004, but at that point it was decided to cancel the project.

Instead, the lab 1 cavity and vacuum chamber would be rebuilt again with three specific aims: to design an asymmetric, “single-sided” cavity, i.e., with one mirror more transmissive than the other, in order to improve data collection and explore new quantum information schemes; to address problems of birefringent stress that had plagued all previous cavity-building efforts; and to improve the background pressure in the vacuum chamber in the hope of achieving longer atom storage times. As Kevin shifted his efforts in his final year to theory for the lab 11 experiment, I took charge of this new project, focusing in particular on designing and assembling a new vacuum chamber and obtaining new cavity mirrors. I supervised two Caltech undergraduates, Yat Shan Au and Travis Bannerman, as they worked on various aspects of this project during their junior and senior years; Cambridge SURF student Toby Burrows also joined us for the summer of 2005. New graduate students Andrey Rodionov and Dalziel Wilson arrived in lab 1 that summer, and Dal assumed responsibility for the lab the following year.

Meanwhile, during 2004 I also began my transition to lab 11, where Andreea Boca and Russell Miller had assumed responsibility for the experiment and David Boozer and Kevin were working on the corresponding theory. Following the work of Carmichael and Tian [24] and of Parkins et al. [25, 26, 27], Christina Hood had predicted a “photon blockade” effect due to the anharmonicity of the Jaynes-Cummings ladder [21], and guided by Kevin’s numerical simulations, we set out to observe this effect in the lab 11 cavity [28, 4, 29]. Specifically, by probing on the lower vacuum-Rabi sideband, we were able to demonstrate that once a photon had entered the cavity, the atom-cavity system blocked the transmission of a second photon. Kevin realized that by measuring the second-order correlation function  $g^2(\tau)$  along the “dark” axis of our cavity, that is, orthogonal to the axis of our probe beam, we could observe

highly sub-Poissonian statistics and photon antibunching.

Kevin, Andreea, and Dave all graduated in the spring of 2005, and Andreea and Dave continued their work on the cavity QED experiment as postdocs. We turned to the question of cooling the center-of-mass motion of the intracavity atoms, which we hoped would both extend the trap storage times and allow us to access the quantum regime for the atom's external degrees of freedom. By introducing a new pair of Raman lasers at 945.6 nm, we were able to demonstrate resolved sideband cooling to the atom's vibrational ground state along the cavity axis [30]. This was also an important application of a new, efficient state-detection scheme, in which we could identify whether an atom was in the  $F = 3$  or  $F = 4$  hyperfine manifold.

Since the single photon generation experiment a few years earlier [16], we had been interested in the reverse process: mapping the information in a photonic state into the cavity, onto the hyperfine ground states of a trapped atom. After all, one advantage of using a cavity to generate single photons on demand was that the output photons were created in a well-defined optical mode, and thus were ideal carriers for quantum information in quantum networking schemes [2]. By using pulses of attenuated laser light to provide a phase-coherent input of photons, we were able to characterize the reversible nature of this process in our cavity — that is, the interplay between coherent and incoherent transfer mechanisms [31].

We have made a number of attempts over the past few years to prepare atoms in a particular Zeeman level via optical pumping, but these attempts have met with only limited success. In mid-2007, we implemented a new Raman-based optical pumping scheme, which has the advantage that we can prepare atoms in any desired Zeeman state [32]. After Andreea's departure that summer, Russ and I characterized the effectiveness of this method in the lab. We also implemented a new conditional loading process for our experiment, allowing us now to load multiple atoms into the cavity with every MOT drop, then heat the extra atoms out of the trap until only one remains. In principle, this will allow us in the future to carry out experiments with exactly one atom present, with possible extensions to higher atom number.

Most recently, we have been exploring the possibility for generating atom-photon

entanglement, and specifically, entanglement between the atom's hyperfine ground state and the polarization of an output cavity photon. This project has included a series of Rabi flopping measurements aimed at characterizing the underlying mechanisms for decoherence in our experiment. We have also developed and demonstrated a technique for mapping superpositions of Zeeman states within a hyperfine manifold onto superpositions of states between hyperfine manifolds, with the goal of measuring atom entanglement directly through state detection.

### 1.3 Overview

Chapter 2 of this thesis focuses on our implementation of ground-state cooling. Our central result is the nearly complete suppression of the red vibrational sideband of a Raman spectrum after cooling; I also present more recent results from second-order sideband cooling at 936 nm. This chapter contains a summary of the current experimental setup in lab 11, including recent changes to the apparatus.

Chapter 3 presents the results of our reversible state transfer experiment as well as several technical developments necessary for its implementation.

In Chapter 4, we return to the topic of Raman transitions: first in the context of our new optical pumping scheme, which relies on incoherent Raman transitions, and then in a discussion of conditional loading, where Raman transitions allow us to determine the intracavity atom number in real time.

With these techniques for atom preparation in hand, in Chapter 5 I present our Rabi flopping and decoherence measurements, and the results of our effort to map Zeeman to hyperfine states. I discuss the outlook for entanglement generation and for the use of microwaves in our experiment.

In Chapters 6 and 7, I return to the work of my first three years in lab 1. I discuss technical insights gleaned from this experience and highlight what in hindsight seem to be useful lessons for those assembling new cavity QED experiments.

## Chapter 2

# Cooling to the ground state of axial motion

### 2.1 In situ cooling: motivation and background

While measurements in Ref. [13] established a lifetime of 2–3 seconds for atoms trapped in the FORT, these were atoms “in the dark,” i.e., only interrogated once after a variable time  $t$  to determine if they were still present. Subsequent experiments have required the trapped atom to interact repeatedly with fields applied either along the cavity axis or from the side of the cavity. In this case, lifetimes have in practice been limited to hundreds of milliseconds due to heating of the atom by the applied fields.

In order to counterbalance these heating processes, one can imagine some method for cooling the atom in situ after it has been loaded into the trap: cooling intervals could then be interleaved as often as necessary between experimental cycles. Interleaved cooling would allow more cycles to occur before the atom was eventually heated out of the trap; ideally, the interrogation time would be limited only by the intrinsic FORT lifetime. In addition, cooling would localize the atom’s center-of-mass motion within a single FORT well. As the atom-cavity coupling  $g$  is spatially dependent, an atom moving within a potential well sees a periodically modulated coupling whose amplitude is proportional to temperature. Effective cooling would thus restrict the range of  $g$  values that the atom could sample.

One means of cooling a trapped atom is by driving a series of Raman transitions that successively lower the atom's vibrational quantum number  $n$ , a process known as sideband cooling. Resolved sideband cooling — in which the vibrational trap frequency  $\omega_a$  is much greater than the Raman transition linewidth  $\Omega$ , so that  $n$ -changing transitions can be independently addressed — was first demonstrated for trapped ions [33, 34] and subsequently extended to neutral atoms trapped in optical lattices [35, 36, 37]. Over the past several years, David Boozer has developed a powerful set of Raman techniques for use in the lab 11 cavity QED experiment. By introducing a second 935.6 nm laser along the cavity axis, phase-locked and polarized perpendicular to the FORT but detuned from it by the cesium ground state hyperfine splitting  $\Delta_{HF}/2\pi = 9.2$  GHz, we can drive Raman transitions between the  $F = 3$  and  $F = 4$  cesium ground states. Thus, the FORT provides both an optical trap for atoms and one arm of a Raman pair. The FORT-Raman pair can be used to prepare an atom in a desired internal state, to measure the magnetic field at the atom's location, and finally, to cool its center-of-mass motion [19]. Because the spatial structure of both beams is defined by the cavity mode, the two standing waves are automatically superimposed upon one another, and the Rabi frequency (proportional to the product of the two field intensities) is the same at the bottom of each FORT well. (The second beam in this configuration will be referred to hereafter as the “Raman beam.”)

The theory of Raman cooling as well as measurements in which cooling is shown to extend the mean lifetime can be found in Dave's thesis [19]. This cooling procedure was also successfully incorporated into the vacuum-Rabi splitting experiment [17], and Fourier-transformed data of  $g^{(2)}(\tau)$  from this experiment demonstrated a shift in the distribution of axial vibrational frequencies in the presence of cooling [29]; the shift was due to the anharmonic character of the FORT well, which means that the trap frequency depends upon the atom's kinetic energy. However, the fact that the Raman and FORT beams are spatially superimposed, though convenient for other applications, makes it difficult to achieve effective cooling. If the relative phase between a FORT and a Raman antinode is given by  $\alpha$ , then in the harmonic approximation at the bottom of a FORT well, the Rabi frequencies for transitions

between vibrational levels  $n, n \pm 1, n \pm 2$  are given by

$$\begin{aligned}\Omega_{n \rightarrow n} / \Omega_\rho &= 1/2 + (1/2 - \eta^2(2n + 1)) \cos 2\alpha, \\ \Omega_{n \rightarrow n \pm 1} / \Omega_\rho &= -\eta \sqrt{n \pm 1} \sin 2\alpha, \\ \Omega_{n \rightarrow n \pm 2} / \Omega_\rho &= -\eta^2 \sqrt{n \pm 1} \sqrt{n \pm 2} \cos 2\alpha,\end{aligned}$$

where  $\eta$  is the Lamb-Dicke parameter and  $\Omega_\rho$  is the (radially dependent) Rabi frequency at the FORT antinode [38]. As  $\alpha = 0$  for the FORT-Raman configuration, we cannot drive couplings between vibrational states  $n$  and  $n - 1$ . Cooling must take place on  $n \rightarrow n - 2$  transitions, which are suppressed by  $\eta^2 \approx 0.0025$  in our experiments.

In order to access  $n \rightarrow n - 1$  transitions, we introduced a new Raman configuration in the cavity in early 2006. The FORT still provided a trapping potential at  $\lambda_F = 936$  nm (a standing wave with  $n_F = 90$  half-wavelengths inside the cavity) but no longer contributed to the Raman process; Raman coupling now took place 10 nm away at  $\lambda_R = 945.6$  nm, the next longitudinal mode of the cavity ( $n_R = 89$  half-wavelengths), using a pair of phase-stable lasers tuned  $\pm \Delta_{HF}/2$  above and below the cavity resonance. As  $\lambda_R \neq \lambda_F$  and  $n_R$  and  $n_F$  have no common denominator,  $\alpha$  takes a different (nonzero) value for every well. Transitions from  $n \rightarrow n - 1$  are possible in each well, though cooling is more effective in certain wells (i.e., one-quarter and three-quarters of the way along the cavity, where  $\alpha \approx \pi/4, 3\pi/4$ ).

## 2.2 Experimental setup

Phase stability between the FORT and Raman lasers in previous experiments was provided by an electronic phase lock: an optical beat note between the two lasers was used to generate an error signal, which was then fed back to the Raman laser current and the piezoelectric transducer controlling the length of the external laser cavity [19]. However,  $\sim 500$  kHz noise observable on the phase lock beat note at  $\Delta_{HF}$  presented serious problems, especially as the  $n \pm 1$  vibrational sidebands of the FORT

were 530 kHz on either side of the carrier and could not be separated from this noise. In setting up the pair of 946 nm diode lasers for Raman cooling, we have instead chosen a master-slave configuration, with one laser injection-locked to a frequency sideband of the other; frequency sidebands at  $\Delta_{HF}$  are applied with a fiber-coupled electro-optic modulator (EOM) from EOSPACE Inc. In his thesis, Russ Miller will describe the specifics of this injection lock, which has since been transferred to the FORT-Raman 936 nm pair.

The lab 11 experimental apparatus is described in detail in Jason McKeever’s thesis [39]; here I summarize the essential components and enumerate recent developments. At the heart of the experiment is the high-finesse optical cavity, constructed by Jun Ye and David Vernooy and enclosed in a two-chamber vacuum system [40]. As we are now two generations of graduate students removed from the original assembly of this system, we treat the cavity and chamber with a great deal of caution and a bit of superstition. A valve controls the flow of cesium into the upper chamber and is opened for a few hours before we attempt to load atoms into the cavity. Surrounding the vacuum chamber are ion pumps, cameras, assorted optics for coupling light in and out of the chamber, and coils to generate magnetic gradient and bias fields for the atoms.

### 2.2.1 Lasers

We use a collection of home-built diode lasers to cool, trap, and probe cesium atoms and to transfer population between their internal states. The central laser in this scheme is the “master laser” on the southwest corner of the optical table. For the purpose of frequency stabilization, this laser is locked to a  $\sim 30$  cm transfer cavity that is subsequently locked to cesium, and specifically, to the crossover between the  $F = 4 \rightarrow F' = 4$  and  $F = 4 \rightarrow F' = 5$   $D2$  resonances in a vapor cell via modulation transfer spectroscopy. (For reference, a diagram of the cesium  $D2$  spectrum can be found in Figure 4.2.) A pair of acousto-optic modulators (AOMs) is used to shift the master laser into resonance with either the  $F = 4 \rightarrow F' = 4$  or  $F = 4 \rightarrow F' = 5$

transition and to shutter the beam on and off. After a series of optical filters, light from the laser is then coupled into the physics cavity; we often refer to this laser as the “probe laser” because it is used to interrogate the atom-cavity system. It has never been necessary to mode-match the probe efficiently into the cavity, and the most recent measurement (in March 2006) found the probe input coupling to be 12.5%.

Light from the master laser is also sent through optical fiber to injection-lock a “slave laser,” an 852 nm diode laser without an external grating. This slave laser provides the red-detuned  $F = 4 \rightarrow F' = 5$  trapping light for MOTs in the upper and lower chamber, which can be shifted to a different frequency and intensity setting for polarization-gradient cooling [29]. Along a separate path, the slave laser also provides blue-detuned  $F = 4 \rightarrow F' = 4$  light that is then circularly polarized and enters the cavity from the side to generate orthogonal standing waves. In tandem with the  $F = 3$  light described below, these “lattice beams” are used to cool falling atoms into the FORT and to prepare the internal states of trapped atoms.

On the north side of the table, a “repump laser” is locked to the  $F = 3$  cesium resonance. Its primary function is to generate beams for both MOTs on the  $F = 3 \rightarrow F' = 4$  transition that can recycle atoms to the  $F = 4$  manifold. In addition, it is the source of an  $F = 3 \rightarrow F' = 3$  lattice beam collinear with the one described above ( $\Omega_3$  and  $\Omega_4$  in Figure 2.3(b)). The current-modulated repump laser was locked to the saturated absorption spectrum of a cesium vapor cell through 2006. At that time, we replaced the cesium lock with a phase lock to the master laser, for purposes described in Chapter 3.

For the experiment described in this chapter, we introduced a frequency-shifted beam from the probe laser path that was resonant with the  $F = 4 \rightarrow F' = 4$  transition. This beam was coupled into optical fiber that carried it to the side of the cavity ( $\Omega'_4$ , Figure 2.3(b)). Focused into the cavity with a cylindrical lens, it can now be used in combination with the  $\Omega_4$  lattice beam to pump a trapped atom into the  $F = 3$  manifold; in the absence of a magnetic field, alternating the two beams is necessary to avoid a dark state in the  $F = 4$  manifold [4, 19].

At 836 nm, our one store-bought diode laser (thus referred to as the “New Focus

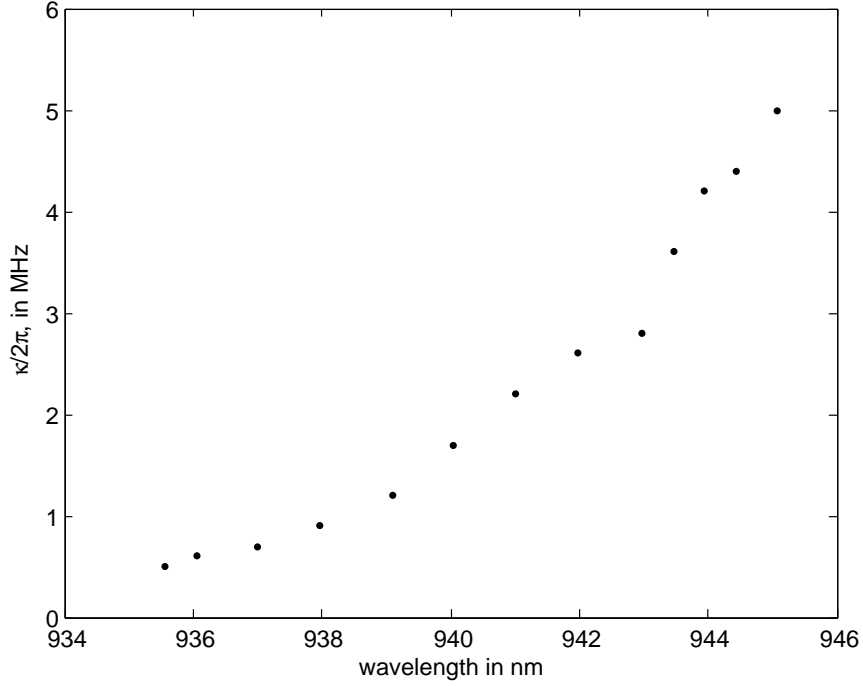


Figure 2.1: Measured physics cavity linewidths between the two Raman wavelengths of 935.6 nm and 945.6 nm

laser”) is resonant with the cavity mode two free spectral ranges away from the cesium resonance. It is used to provide active feedback to maintain the cavity length via a Pound-Drever-Hall lock in transmission [41]. The New Focus laser frequency is stabilized by a reflection lock to the transfer cavity; the physics cavity is then locked to a frequency sideband of the New Focus laser. The sideband lock allows us to tune the sideband frequency manually, so that we can adjust the physics cavity frequency  $\omega_c$  with respect to the cesium resonance  $\omega_a$ . The sidebands, applied with a highly tunable traveling-wave modulator, are usually between 300 and 800 MHz in frequency, and the transmission lock is derived from a 4 MHz modulation of this signal.

The probe laser and New Focus laser are combined at the cavity input with the FORT laser at 936 nm. While Jason’s thesis mentions that the FORT was frequency-modulated and locked to the physics cavity, this lock has been since discontinued and the EOM removed, as it was found to be unnecessary: since the FORT cavity linewidth is so wide ( $\kappa_F/2\pi = 0.8$  GHz), once the laser is tuned into resonance, its

slow transmission drifts can be corrected manually on the timescale of hours. In fact, changes in intracavity power due to amplitude drift at the cavity input can be more substantial than those due to frequency drift and would not be corrected by a frequency lock. More recently, we have implemented a feedback loop to directly stabilize the FORT power in transmission using a liquid-crystal variable oscillator (LCVO).

At the side of the lab, a second  $F = 3$  diode laser with its own cesium lock sits on a honeycomb breadboard. In 2005, we rebuilt this laser so that it provided separate beams on the  $F = 3 \rightarrow F' = 3$  and  $F = 3 \rightarrow F' = 4$  transitions, each with switching capabilities. The beams were recombined and coupled onto orthogonal axes of a polarization-maintaining fiber. As with the  $F = 4 \rightarrow F' = 4$  beam above, they were brought in from the side of the cavity and used in several optical pumping attempts (Chapter 4). Despite our best efforts to stabilize the diode and isolate the assembly from air currents, this laser has always been difficult to work with, probably because it does not benefit from the vibration isolation of an optical table.

The final lasers in our experiment, the 946 nm Raman pair, have already been discussed above. It was not originally known whether the cavity would support a mode at the new Raman wavelength, as the coating curve for the cavity mirrors falls off steeply in this vicinity [42]. In order to measure the cavity linewidth as a function of wavelength, we increased the wavelength of the old Raman laser in 1 nm steps from its original value of  $\lambda_F$ . We used the sidebands of the New Focus locking laser, set to 1 GHz, as a meterstick in order to obtain the cavity linewidth  $\kappa$  from the scope trace at each wavelength. The linewidth data are plotted in Figure 2.1; at our wavelength of interest,  $\kappa_R/\kappa_F = 6 \text{ GHz}/0.8 \text{ GHz}$ , and the finesse at  $\lambda_R$  decreases proportionally from  $\mathcal{F}_F = 2200$  to  $\mathcal{F}_R = 300$ .<sup>1</sup>

---

<sup>1</sup>The values given here for  $\kappa_R$  and  $\kappa_F$  are drawn from Section 2.3 rather than the data in Figure 2.1. In particular, a subsequent measurement determined that  $\kappa_F = 0.8$  rather than 0.5 as shown above.

## 2.2.2 Output path and detection

At the cavity output, a half-waveplate at 852 nm and a polarizing beamsplitter cube (PBS) are used to select output light along one of the cavity’s two birefringent axes.<sup>2</sup> At the rejected port of the PBS, a New Focus DC-125 MHz detector monitors the FORT transmission. Unfortunately, this scheme cuts our detection efficiency in half for unpolarized photon generation and prevents us from examining orthogonal output polarizations simultaneously. Because we have some well-founded hesitation about dismantling the output path of a working experiment, we have left it in place until now but have plans for a rebuild in the near future.

After the PBS, the cavity output is collimated, and an angle-tuned mirror separates the 836 nm light for the cavity lock. A series of four dichroic mirrors and two interference filters suppresses the remaining 836 nm and 936 nm light in the path before the light is finally coupled into optical fiber. In December 2005, we measured the propagation efficiency  $p_{table}$  to be 66% before fiber coupling, with losses attributed to individual elements listed in Table 2.1. This measurement is roughly consistent with the values of  $p_{path} = p_{couple}p_{table} = 32\%$  and  $40\%$  given in Refs. [16, 29], where  $p_{couple}$  includes fiber coupling losses; in November 2006, we improved the fiber alignment, which boosted  $p_{path}$  from 30% to 50%. The dichroic elements are relatively ineffective at suppressing FORT light — each dichroic removes less than half of incident light at 936 nm — and should probably be removed from future beam paths, as they are also not perfect at 852 nm. Each interference filter, on the other hand, has a measured suppression of  $10^4$  at 936 nm. It is interesting to note that given the measured FORT propagation losses at each step of the path, we would still expect the FORT power to saturate our detectors, while in fact we see fewer than 5 photon counts/second due to 936 nm light. It must be true that optimizing the probe coupling into fiber at 852 nm results in very poor FORT fiber coupling. We believe that this is due to refraction in the PBS cube at the cavity output, which causes light at the two wavelengths to

---

<sup>2</sup>The cavity supports two orthogonal linear modes, with a frequency splitting between the modes roughly equal to  $\kappa$ . The most recent measurements of this frequency splitting can be found in Ref. [29]. Chapter 6 provides a discussion of birefringence in the context of cavity design.

Path element(s)	Propagation losses, in percent
first mirror	0
angle-tuned splitter	3
second mirror	2
third mirror + lens	1
iris + half-waveplate + lens + dichroic 1	1
dichroics 2 + dichroic 3	10
first interference filter	10
second interference filter	17
dichroic 4	3

Table 2.1: Measured propagation losses at 852 nm in the lab 11 cavity output path. Some path elements are grouped together because of the practical difficulty of inserting a detector between them.

follow slightly different paths.

Once the cavity light is coupled into single-mode fiber, a fiber beamsplitter carries it to two single-photon-counting modules (Perkin-Elmer SPCM–AQR). We record TTL logic pulses from the SPCMs using a P7888 four-channel data acquisition card; these cards are also currently in use in lab 2 and in the microtoroid experiment. A heterodyne detection path, while still in place on the optical table, has been used in recent years only for alignment purposes, in cases where we were concerned about the possibility of too much incident light on the SPCMs.

### 2.2.3 Analog and digital control

Analog and digital timing control signals for the experiment are generated by an ADwin-Gold system (Jäger Computergesteuerte Messtechnik GmbH). The ADwin has an internal 40 MHz CPU; we map a series of instructions into its RAM from a PC via USB connection, and it then runs continuously until the next program is loaded. Dave has written a straightforward user interface that compiles our timing programs into the (less intuitive) ADbasic language that the system requires. In Chapter 4, I describe recent modifications to our timing programs that allow us to condition the experiment on the presence of at most one atom in the cavity.

Most of the experiment timing is digital, but the analog outputs of the ADwin are

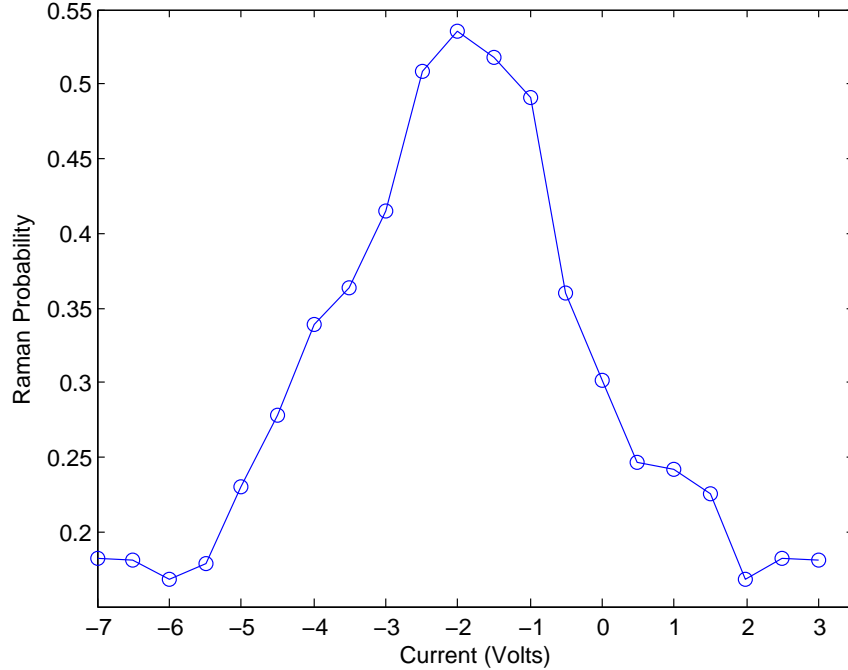


Figure 2.2: Probability to drive Raman transitions as a function of control voltage for the magnetic bias field along the “fed from above” axis, where the conversion factor is 0.97 Gauss/V. The peak indicates a local field minimum.

used to provide control voltages for the bias coil current supplies, which determine the magnetic fields at the cavity. In order to have control over the magnetic field that an atom experiences during an experiment, we first need to adjust the bias coil currents in order to null the ambient fields seen by the atom. Here we rely on the fact that when the fields are nulled, the Raman transition frequencies between all Zeeman sublevels are degenerate. Thus, for a given atom in an unknown Zeeman state, the probability to drive a Raman transition is greatest in a nulled field [19]. If we record the Raman transition probability as a function of bias coil current (that is, as a function of ADwin control voltage) along each axis, we can then associate the maximum transition probability with a local field minimum.

An example of a Raman field nulling scan along one axis is shown in Figure 2.2. During the measurement, fields along the other two axes are fixed at their nominal null values. As these initial values may not be accurate, it is sometimes necessary to iterate the nulling procedure a few times in order to find the field minimum along all

three axes. This was at first a rather time-consuming process, as we would increment the bias coil current by hand. Once we switched to an ADwin control program that automatically scanned the current and stamped the data records accordingly, the situation improved greatly, and we are now able to null the magnetic fields within approximately half an hour. We find that for experiments requiring sensitive control of magnetic fields, it is best to null the fields within a few days of data collection to avoid any surprising drifts. The axial bias field value seems to be the most stable, while the current through the “fed from below” coil is the most likely to need adjustment.

### 2.3 Demonstration of ground-state cooling

The following section has been adapted from Ref. [30].

Localization to the ground state of axial motion is demonstrated for a single, trapped atom strongly coupled to the field of a high-finesse optical resonator. The axial atomic motion is cooled by way of coherent Raman transitions on the red vibrational sideband. An efficient state detection scheme enabled by strong coupling in cavity QED is used to record the Raman spectrum, from which the state of atomic motion is inferred. We find that the lowest vibrational level of the axial potential with zero-point energy  $\hbar\omega_a/2k_B = 13 \mu K$  is occupied with probability  $P_0 \simeq 0.95$ .

Single atoms strongly coupled to the fields of high-quality optical resonators are of fundamental importance in Quantum Optics and, more generally, can be used for many tasks in quantum information science, including the implementation of scalable quantum computation [43, 44] and the realization of distributed quantum networks [2, 45]. In recent years, significant experimental progress to develop tools suitable for these tasks has been made by employing optical forces to localize individual atoms within optical cavities in a regime of strong coupling [12, 13, 17, 46, 47, 48, 49], as well as by combining trapped ions with optical cavities [50, 51]. Scientific advances thereby enabled include the observation of the vacuum-Rabi spectrum for an individual atom [17] and vacuum-stimulated cooling [48].

Although great strides are being made with atoms localized and strongly coupled

to the fields of optical cavities, it has not previously been possible to access the quantum regime for the atomic center-of-mass motion in cavity QED. Qualitatively new phenomena have been predicted in this regime for which a quantized treatment is required for both the internal (i.e., the atomic dipole and cavity field) and external (i.e., atomic motion) degrees of freedom, as was first recognized in the seminal work of Refs. [52, 53, 54] and in the years since [55, 56, 57, 58, 59, 60, 61, 62, 63, 64, 65, 66]. Examples include the transfer of quantized states of atomic motion to quantum states of light, and conversely [64, 65, 66], as well as for measurements that surpass the standard quantum limit for sensing atomic position [55, 56].

Our effort towards quantum control of atomic motion in cavity QED follows the remarkable set of achievements for trapped ions [34] and atoms in optical lattices [35, 36, 37], for which such control has led to the creation of manifestly quantum states of motion and to the manipulation of quantum information. A first step in many of these investigations has been the capability to cool to the ground state of motion for single trapped atoms or ions.

Here we report localization to the ground state of motion for one atom trapped in an optical cavity in a regime of strong coupling [49]. Resolved sideband cooling to the ground state is accomplished with a coherent pair of intracavity Raman fields. To deduce the resulting state of atomic motion, we introduce a scheme for recording Raman spectra by way of the interaction of the atom with a resonant cavity probe. Our scheme is the cavity QED equivalent of state detection in free space by quantum-jump spectroscopy [34] and achieves a confidence level for state discrimination  $> 98\%$  in  $100 \mu\text{s}$ . From the Raman spectra, we infer that the lowest vibrational level  $n = 0$  of the axial potential is occupied with probability  $P_0 \simeq 0.95$  for one trapped atom.

A schematic of the experiment is given in Figure 2.3. At the heart of the system is the Fabry-Perot cavity formed by mirrors ( $M_1, M_2$ ). The cavity length is stabilized to  $l_0 = 42.2 \mu\text{m}$  using an independent locking laser, such that a  $TEM_{00}$  mode is resonant with the  $6S_{1/2}, F = 4 \rightarrow 6P_{3/2}, F' = 5$  transition of the  $D2$  line in Cs. The resulting atom-cavity coupling gives a maximum single-photon Rabi frequency of  $2g_0/2\pi = 68 \text{ MHz}$  for  $(F = 4, m_F = \pm 4) \rightarrow (F' = 5, m'_F = \pm 5)$ . The decay

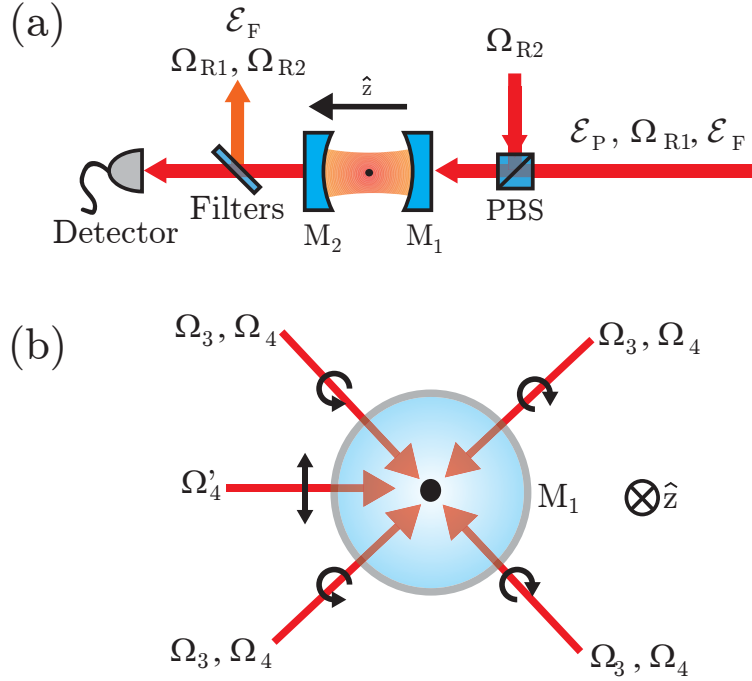


Figure 2.3: Schematic of the experiment. The cavity is represented (a) from the side and (b) along its axis, with a trapped atom indicated as a dot at the cavity center. Shown are the various beams used in the experiment: linearly polarized probe  $\mathcal{E}_P$ , FORT  $\mathcal{E}_F$ , pumping  $\Omega'_4$ , and Raman beams  $\Omega_{R1,R2}$ , as well as the circularly polarized lattice beams  $\Omega_{3,4}$ .

rates are  $\gamma/2\pi = 2.6$  MHz for the  $6P_{3/2}$  excited states, and  $\kappa/2\pi = 4.1$  MHz for the cavity field.<sup>3</sup> Because  $g_0 \gg (\gamma, \kappa)$ , our system is in the strong coupling regime of cavity QED [49], with critical photon and atom numbers  $n_0 \equiv \gamma^2/(2g_0^2) \approx 0.0029$  and  $N_0 \equiv 2\kappa\gamma/g_0^2 \approx 0.018$ .

Atoms are trapped by an intracavity far-off-resonant trap (FORT) at  $\lambda_F = 935.6$  nm, which is driven by a linearly polarized input field  $\mathcal{E}_F$  and is resonant with a  $TEM_{00}$  mode of the cavity with linewidth  $\kappa_F/2\pi = 0.8$  GHz. At  $\lambda_F$ , states in the ground  $F = 3, 4$  and excited state  $F' = 5$  manifolds experience nearly equal trapping potentials. For states in the  $F = 3, 4$  manifolds, this potential is independent of  $m_F$  and has a peak value of  $U_F/h = -41$  MHz, while for states in the  $F' = 5$

<sup>3</sup>This value for  $\kappa/2\pi$  differs from the 3.8 MHz rate found elsewhere in this thesis, which is based on a more recent measurement. As discussed in detail in Ref. [29], we have seen as much as 20% variation in measured cavity linewidths using different techniques. Some of this variation may be due to input light which is not polarized along one of the cavity's birefringent axes and thus couples to both cavity modes.

manifold it has a weak dependence on  $m'_F$  [13, 17]. The standing-wave structure of the FORT forms independent wells where atoms may be trapped. Near the bottom of a FORT well the potential is approximately harmonic, with axial and radial vibrational frequencies  $\omega_a/2\pi = 530$  kHz,  $\omega_r/2\pi = 4.5$  kHz.

To load atoms into the FORT, we release a cloud of cold atoms located  $\sim 3$  mm above the cavity [13]. As the atoms fall through the cavity, we apply 5 ms of  $\Omega_3$ ,  $\Omega_4$  light by way of two pairs of counterpropagating  $\sigma_+ - \sigma_-$  polarized beams; see Figure 4.1(b). These beams are blue detuned by +10 MHz from the  $F = 3 \rightarrow F' = 3$  and  $F = 4 \rightarrow F' = 4$  transitions respectively, and cool the falling atoms via polarization gradient cooling [67]. We adjust the powers<sup>4</sup> of these beams so that the probability of loading at least one atom is  $\sim 0.3$  per cloud drop.

Raman coupling between the  $F = 3$  and  $F = 4$  manifolds is generated by driving a cavity mode at  $\lambda_R = 945.6$  nm with a pair of beams  $\Omega_{R1,R2}$  that are phase-locked,  $\text{lin} \perp \text{lin}$  polarized, and have a relative detuning  $\omega_{R1} - \omega_{R2} = \Delta'_{HF} + \delta_R$ , where  $\Delta'_{HF}/2\pi = 9.19261$  GHz is the Cs hyperfine splitting<sup>5</sup> and  $\delta_R$  is the Raman detuning. This cavity mode has a linewidth  $\kappa_R/2\pi = 6$  GHz, and the Raman beams are tuned such that  $\Omega_{R1(R2)}$  lies  $\Delta'_{HF}/2$  above (below) cavity resonance. Since  $\Omega_{R1,R2}$  drive a different mode of the cavity than  $\mathcal{E}_F$ , atoms trapped in different FORT wells see different Raman powers. If the relative spatial phase along the cavity axis between the FORT and the Raman pair at the bottom of a given well is  $\alpha$ , then an atom at this potential minimum sees a Raman power proportional to  $\cos^2 \alpha$ .

We set the optical power transmitted on resonance through the cavity for  $\Omega_{R1,R2}$  to  $P_{R1} = P_{R2} = 140 \mu\text{W}$ , which gives a Rabi frequency<sup>6</sup>  $\Omega_0/2\pi = 200$  kHz for atoms with  $\alpha = 0$ . The ac-Stark shift due to these beams adds a correction to the FORT potential of  $U_R/2\pi = 0.84$  MHz. To avoid heating the atom by switching  $U_R$ , we

<sup>4</sup> For loading, the total power in the four lattice beams is  $50I_4^{\text{sat}}$  for  $\Omega_3$  and  $\Omega_4$ , where  $I_4^{\text{sat}} \sim 3.8$  mW/cm<sup>2</sup>. For detection, the  $\Omega_3$  intensity is  $5I_4^{\text{sat}}$ .

<sup>5</sup> $\Delta'_{HF}$  for a trapped atom is slightly reduced compared to its free space value  $\Delta_{HF}$ , because the FORT potential for the  $F = 3$  manifold is slightly weaker than for  $F = 4$ . For our FORT, the correction is  $\Delta'_{HF} - \Delta_{HF} = -21$  kHz.

<sup>6</sup>Here  $\Omega_0$  is the Rabi frequency for the transition  $F = 3, m = 0, n = 0 \rightarrow F = 4, m = 0, n = 0$ , where the quantization axis is along the cavity axis.

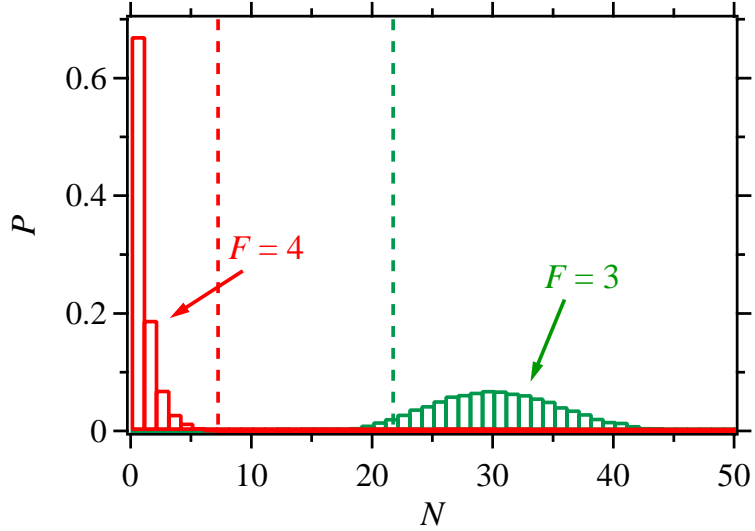


Figure 2.4: Histogram of counts recorded during  $100 \mu\text{s}$  probing intervals for  $N_e = 30$ . The left (right) curve is the probability  $P$  of detecting a number of counts  $N$  for an atom prepared in the  $F = 4$  ( $F = 3$ ) state. The dashed lines indicate detection thresholds at  $N = 0.25N_e$  and  $N = 0.75N_e$ .

leave  $\Omega_{R1,R2}$  on all the time, but usually keep them far-detuned ( $\delta_R/2\pi = 85 \text{ MHz}$ ) from Raman resonance. To drive Raman transitions, we change  $\omega_{R2}$  to bring the pair into Raman resonance, whereas to fine-tune  $\delta_R$  we vary  $\omega_{R1}$ .

Because the intensity of the Raman pair is spatially varying, the Raman coupling can connect states with different vibrational quantum numbers. The form of this motional coupling is simple for atoms near the bottom of a FORT well where the axial and radial motions decouple, allowing us to consider the effect of the Raman coupling on the axial motion alone. In this harmonic limit, we can define a set of Fock states  $\{|n\rangle\}$  for the axial motion. For transitions from  $F = 3, m = 0$  to  $F = 4, m = 0$  and to first order in  $\eta$ , the Rabi frequency for an  $n \rightarrow n$  transition is  $\Omega_{n \rightarrow n} = (1/2)(1 + \cos 2\alpha)\Omega_0$ , while for an  $n \rightarrow n - 1$  transition,  $\Omega_{n \rightarrow n-1} = \eta\sqrt{n} \sin 2\alpha \Omega_0$ , where  $\eta = (2\pi/\lambda_R)\sqrt{\hbar/2m\omega_a} = 0.056$  is the Lamb-Dicke parameter for axial motion. Note that the  $n \rightarrow n - 1$  transition is strongest for atoms with  $\alpha = \pi/4$ .

The spatial dependence of the Raman coupling, together with the fact that the axial motion of the atom is in the Lamb-Dicke limit, allows us to implement Raman sideband cooling [34]. We tune the Raman pair to the red axial sideband

( $\delta_R = -525$  kHz  $\simeq -\omega_a$ ) and apply the  $\Omega_4$  lattice beams. An atom that starts in  $F = 3$  is coherently transferred by  $\Omega_{R1,R2}$  to  $F = 4$ , where it is incoherently repumped to  $F = 3$  by  $\Omega_4$ . The coherent transfer lowers the axial vibrational quantum number  $n$  by one, while the incoherent repumping usually leaves  $n$  unchanged since  $n$ -changing transitions are Lamb-Dicke suppressed. Thus, the beams continually lower  $n$ , cooling the atom to the axial ground state. Also, the  $\Omega_4$  light provides Sisyphus cooling [67] in the radial direction.

Strong atom-cavity coupling enables a versatile detection scheme for determining if an atom is present in the cavity, and if so, if it is in the  $F = 3$  or  $F = 4$  manifold. In 100  $\mu$ s we measure the atomic hyperfine state with a confidence level of  $> 98\%$ . The scheme involves driving the cavity with a 100  $\mu$ s pulse of resonant  $F = 4 \rightarrow F' = 5$  probe light  $\mathcal{E}_P$ . If an  $F = 3$  atom is present (or if the cavity is empty), then the light is transmitted, while if an  $F = 4$  atom is present, then the light is blocked because of strong coupling [17]. We set the  $\mathcal{E}_P$  intensity such that on average  $N_e$  photons are detected<sup>7</sup> per probing interval with no atom in the cavity. As shown in Figure 2.4, if the number  $N$  of detected photons is such that  $N < 0.25N_e$ , we assume an  $F = 4$  atom is present; if  $N > 0.75N_e$ , we assume an  $F = 4$  atom is not present; otherwise, the measurement is inconclusive ( $< 2\%$  of the time) and we ignore the result. Whenever we detect the atomic state, we perform two such measurements: the first with  $\mathcal{E}_P$  to find out if an  $F = 4$  atom is present, the second with  $\mathcal{E}_P$  together with  $\Omega_3$  as a repumper, to detect an atom, regardless of its internal state.

We measure the Raman transfer probability  $P_4$  for a given  $\delta_R$  by preparing an atom in  $F = 3$ , applying a Raman pulse, and then detecting the atomic state using the above scheme (with  $N_e \sim 22$ ). For each measurement cycle (or trial), we first Raman-sideband cool the atom for an interval  $\Delta t_c$ . Next, we pump it into  $F = 3$  by alternating 1  $\mu$ s pulses of  $\Omega_4$  lattice light with 1  $\mu$ s pulses of  $\Omega'_4$  linearly polarized resonant  $F = 4 \rightarrow F' = 4$  light from the side of the cavity (10 pulses of each). After the atom is pumped to  $F = 3$ , we apply a  $\Delta t_R = 500$   $\mu$ s Raman pulse, which

---

<sup>7</sup>The probability for a photon starting out within the cavity to be recorded by our detectors is  $e \sim 0.06$ .

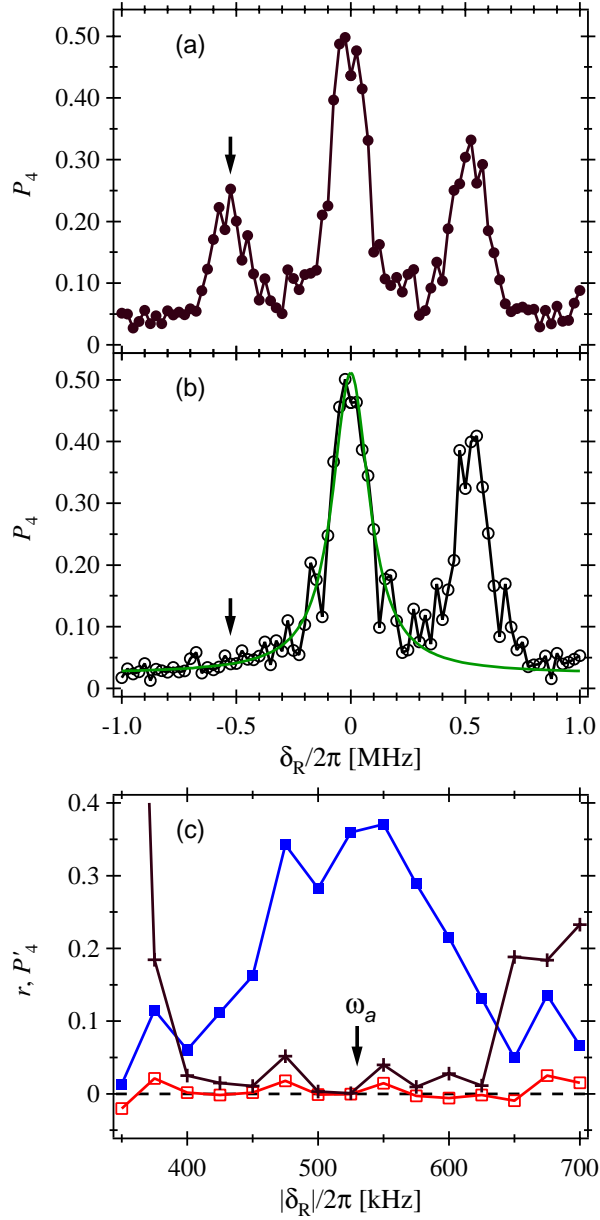


Figure 2.5: Population  $P_4$  in the  $F = 4$  state vs. Raman detuning  $\delta_R/2\pi$ . The data in (a) are taken with  $\Delta t_c = 250 \mu\text{s}$  of cooling, and an  $\Omega_4$  total 4-beam intensity  $I_4 = 5I_4^{\text{sat}}$ ; those in (b) with  $\Delta t_c = 5$  ms of cooling, and  $I_4 = 0.5I_4^{\text{sat}}$  (on average,  $\sim 33$  atoms per data point). The arrow marks the detuning used for sideband cooling. (c) Zoom-in on the two sideband regions for the data in (b), with detuning axis folded around  $\delta_R = 0$ . The red ( $\square$ ) and blue ( $\blacksquare$ ) sidebands, and their ratio  $r$  (+), are shown after subtracting a Lorentzian fit to the carrier [superimposed in (b)].

sometimes transfers it to  $F = 4$ . Finally, we measure the atomic state and check if the atom is still present. For each atom we fix the absolute value of the Raman

detuning  $|\delta_R|$ , and alternate trials at  $+|\delta_R|$  with trials at  $-|\delta_R|$  (299 trials each). By combining data from atoms with different values of  $|\delta_R|$ , we map out a Raman spectrum. Note that because the initial Zeeman state of the atom is random, all allowed  $F = 3 \rightarrow F = 4$  Zeeman transitions contribute to these spectra.

Two example Raman spectra are plotted in Figure 2.5. For the curve in Figure 2.5(a), we cool for  $\Delta t_c = 250 \mu\text{s}$ ; for the curve in Figure 2.5(b), for  $\Delta t_c = 5 \text{ ms}$ . These scans are performed after nulling the magnetic field to within  $\sim 40 \text{ mG}$ ; the widths of the peaks are set by the splitting of different Zeeman levels due to the residual magnetic field. For the curve in panel (a), we see peaks at the carrier ( $\delta_R = 0$ ), as well as at the blue/red sidebands ( $\delta_R/2\pi \simeq \pm 530 \text{ kHz} = \pm \omega_a$ ). Already we note a sideband asymmetry, indicating that a significant fraction of the population is in the  $n = 0$  vibrational state. For the (b) data, the red sideband at  $\delta_R/2\pi \simeq -530 \text{ kHz}$  is suppressed such that it cannot be distinguished from the background and contribution from off-resonant excitation of the carrier.

The ratio  $r$  of transfer probabilities for the red and blue sideband gives information about the temperature of the atom. For a two-state atom in a thermal state, this ratio  $r_0$  at  $|\delta_R| = \omega_a$  is related to the mean vibrational quantum number  $\bar{n}$  by  $r_0 = \bar{n}/(\bar{n}+1)$  [34]. In Figure 2.5c, we plot  $r$  as a function of  $|\delta_R|$  for the  $\Delta t_c = 5 \text{ ms}$  data. As shown in Figure 2.5b, we fit a Lorentzian curve to the carrier, then subtract its contribution from both the red and the blue sideband data, as shown in Figure 2.5(c). We find  $r_0 \simeq \bar{n} = 0.01 \pm 0.05$ , and the ground state population  $P_0 = 1/(\bar{n} + 1) = 0.99 \pm 0.05$ , where the error bars reflect fluctuations in the data around  $|\delta_R| = \omega_a$ . If instead we subtract the constant background of  $P_4^B = 0.024$  but not the carrier's Lorentzian tail, we find  $r_0 \simeq \bar{n} = 0.05 \pm 0.04$ , and  $P_0 = 0.95 \pm 0.04$ . Finally, if we use the raw data from Figure 2.5b with no subtractions, we obtain  $r_0 = 0.10 \pm 0.03$ ,  $\bar{n} = 0.12 \pm 0.04$  and  $P_0 = 0.89 \pm 0.03$ . Because the atom is not a two-state system and the motional state is not known to be thermal, these estimates are approximate.

The axial cooling rate and asymptotic value of  $\bar{n}$  depend on  $\delta_R$ , on the  $\Omega_{R1,R2}$  Rabi frequencies, and on the power and detuning of  $\Omega_4$ . We have performed computer simulations to help us choose optimal values for these parameters. A common feature

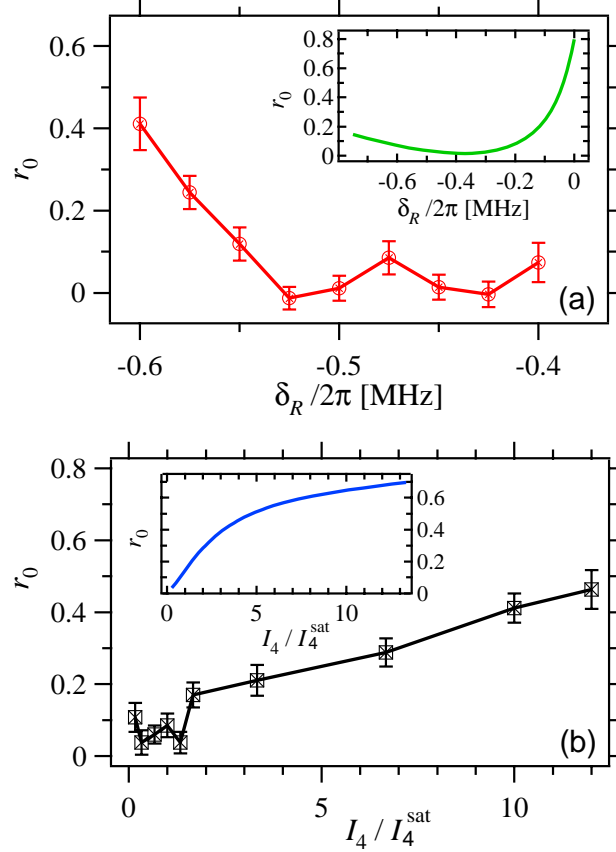


Figure 2.6: Varying cooling parameters. The sideband ratio  $r_0$  is shown as a function of (a) the Raman detuning  $\delta_R$  employed for cooling and (b) the  $4 \rightarrow 3$  repumping intensity  $I_4$ . Insets show the results from a simple calculation for a 2-state atom trapped in a FORT well with  $\alpha = \pi/4$ .

of both our theoretical and experimental investigations is the robustness of  $\bar{n}$  under variations of the cooling parameters. As an example<sup>8</sup>, in Figure 2.6 we plot the measured sideband ratio  $r_0$  at  $\delta_R/2\pi = -500$  kHz  $\simeq -\omega_a$  as a function of (a) the detuning  $\delta_R$  used for sideband cooling, and (b) the recycling intensity  $I_4$ . The sideband asymmetry is maintained over a range of at least 200 kHz in detuning, and of two orders of magnitude in the intensity  $I_4$  of the  $\Omega_4$  beams. The insets give results from a 2-state calculation of  $r_0$ , displaying similar insensitivity to the exact values of  $\delta_R$  and  $I_4$ .

We use two methods for estimating the mean energy  $E_r$  for radial motion. The

<sup>8</sup>Unless otherwise noted, the settings for this measurement are:  $I_4 = 0.3I_4^{\text{sat}}$ ,  $\Delta t_c = 5$  ms,  $\delta_R = -500$  kHz,  $\Delta t_R = 50$   $\mu$ s;  $P_4^B = 0.065$  was subtracted before computing  $r_0$ .

first method involves adiabatically lowering the FORT depth to zero, so that only the  $U_R$  trapping potential remains, and measuring the probability that the atom survives the process [68]. If we assume a thermal state for the radial motion, this method limits  $E_r \lesssim 200 \mu\text{K}$ . The second method relies on the fact that radial motion would shift and/or broaden the axial sidebands in our Raman spectra. By applying a small axial bias field, we can resolve motional sidebands of transitions between specific Zeeman levels; the positions and widths of these sidebands also limit  $E_r \lesssim 200\mu\text{K}$ . However, the Sisyphus cooling we use radially has been previously shown to reach temperatures of  $\sim 1 \mu\text{K}$  [67], which corresponds to  $n_{rad} \simeq 4$  for an atom in our FORT. A possibility for improved determination of the radial “temperature” is to monitor the transmission of the cavity probe field, as in Ref. [17]. Note that the ratio of radial to axial trapping frequencies ( $\simeq 0.01$ ) is such that any modulation of the axial frequency due to radial motion would be adiabatic. As a result, we expect that an atom cooled to the axial ground state does not change its state due to radial motion.

In conclusion, we have demonstrated cooling to the ground state of axial motion for single cesium atoms strongly coupled to the field of a small optical resonator. Together with existing capabilities for strong coupling of the internal degrees of freedom, control over the external center-of-mass motion in cavity QED enables a new set of phenomena to be explored at the light-matter interface. For example, arbitrary states of atomic motion can be prepared from the ground state by coherent Raman transitions [34], then mapped to the electromagnetic field by way of the strong atom-field coupling [64, 65, 66]. Investigations of sensing atomic motion at the standard quantum limit and feedback control now become feasible [55, 56, 69].

## 2.4 Resolved second-order sideband cooling

As discussed in Section 2.1, it is possible to cool trapped atoms on the second-order red sideband using the FORT-Raman pair. Although this method is less efficient, there are many experiments in which we rely on the FORT-Raman pair to drive Raman transitions whose Rabi frequency is well-independent, such as the Rabi flopping

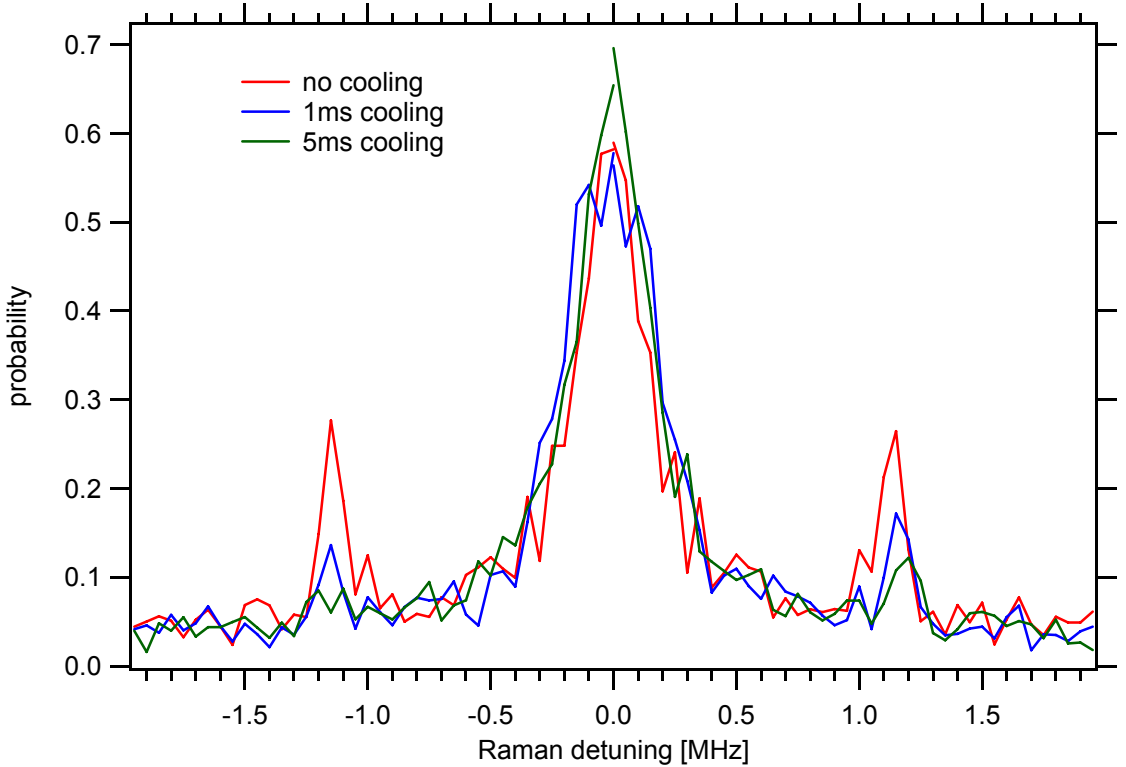


Figure 2.7: Population  $P_4$  in the  $F = 4$  state vs. Raman detuning  $\delta_R/2\pi$ , after second-order sideband cooling. Cooling intervals of (a) 0 ms, (b) 1 ms, and (c) 5 ms are applied using the FORT-Raman pair.

measurements in Chapter 5. It is useful in these situations to be able to cool the atoms, even if we cannot achieve the ground-state cooling described in Section 2.3. (Ideally, our lab would have a pair of Raman lasers at 946 nm for ground-state cooling and a separate FORT-Raman pair for well-independent transitions. At the moment, however, we have only three lasers: dedicated FORT and Raman lasers, and a third injection-locked laser whose wavelength must be adjusted manually in order to move between the two configurations.)

In the past, we were unable to observe resolved-sideband cooling using the FORT-Raman pair because of  $\sim 500$  kHz noise inherent to the phase lock between the lasers. With the replacement of the phase lock by an injection lock during the ground state cooling experiment, this noise was no longer an issue. In the spring of 2007, we measured Raman spectra similar to those presented in Figure 2.5, but in this case with cooling at 936 nm; these data are shown in Figure 2.7. After initial preparation

in  $F = 3$ , atoms are cooled with an applied pulse of the FORT-Raman pair, tuned 1.150 MHz red of resonance to the  $n \rightarrow n - 2$  vibrational sideband, in conjunction with a  $F = 4 \rightarrow F' = 4$  repump. In order to measure the Raman transfer probability for a given detuning, we use the same technique as in the previous section; that is, for each atom at detuning  $\delta$ , we apply a 500  $\mu\text{s}$  Raman pulse, followed by state detection to determine whether that pulse has transferred an atom to  $F = 4$ . For these measurements, the bias fields have been nulled, so all  $|3, m\rangle \rightarrow |4, m\rangle$  transitions are degenerate.

We emphasize two features of the data in Figure 2.7. First, while in the absence of cooling, the red and blue sidebands are roughly symmetric, there is a clear relative suppression of the red sideband after 5 ms of cooling (although the red sideband can still be discerned from the carrier). Second, the widths of both sidebands become narrower, and the center frequencies of the sidebands shift toward higher detunings. This also provides strong evidence for cooling: recall that the FORT potential is sinusoidal and only harmonic in the low-temperature limit. The vibrational frequency spacing at the top of each well is about half the spacing at the bottom, and so the sideband narrowing reflects the fact that we are driving  $n \rightarrow n \pm 2$  transitions for increasingly smaller  $n$ .

Second-order sideband cooling is a promising technique that we hope to incorporate in future experiments, both to localize atoms in the FORT wells and to extend their lifetimes in the trap. However, one caveat is that bias fields must be nulled in order for the cooling to address all Zeeman sublevels, while many of our recent experiments use an axial bias field to split out these sublevels. In principle, one could use an array of RF frequency generators to address the second-order sidebands of all seven  $|3, m\rangle \rightarrow |4, m\rangle$  transitions independently, but that would constitute a new level of complexity for our experiment.

## Chapter 3

# A light-matter interface: quantifying coherence

One of the first experiments conducted in our group with a trapped intracavity atom was to demonstrate that it could generate single photons on demand by means of an adiabatic (dark-state) process [16]. After the ground-state cooling experiment, we turned our attention again to this process, with the idea of mapping cavity-generated photons back onto the atom. In this way, we could exploit an important feature of photon generation within a cavity: the fact that the output photon is created in a well-defined spatial mode. Moreover, the photon generation process is coherent and thus reversible: by running the same adiabatic process backwards, we can in principle achieve state transfer from light (photons) to matter (cesium hyperfine levels).

However, as we began to set up the experiment, we realized that using single photons would restrict our ability to characterize the phase coherence of the process we hoped to demonstrate. Coherence, meanwhile, is at the heart of the quantum information schemes for which this mapping could be employed. We decided instead to explore reversible state transfer by using a pulse of weak coherent light at the cavity input that had roughly the same temporal profile as a cavity-generated photon. From a pair of coherent pulses in sequence, we could then extract important phase information about the transfer process. The results of this experiment are reproduced in Section 3.1. The following sections are then devoted to a more thorough discussion of technical details, including the necessary pulse combinations and timing sequences,

the requirements of phase stability between pairs of laser pulses, and remote serial programming of electronic devices. I conclude by discussing the outlook for mapping single photons to and from the cavity in the future.

### 3.1 Reversible state transfer between light and a single trapped atom

The following section has been adapted from Ref. [31].

We demonstrate the reversible mapping of a coherent state of light with mean photon number  $\bar{n} \simeq 1.1$  to and from the hyperfine states of an atom trapped within the mode of a high-finesse optical cavity. The coherence of the basic processes is verified by mapping the atomic state back onto a field state in a way that depends on the phase of the original coherent state. Our experiment represents an important step towards the realization of cavity QED-based quantum networks, wherein coherent transfer of quantum states enables the distribution of quantum information across the network.

An important goal in quantum information science is the realization of quantum networks for the distribution and processing of quantum information [1], including for quantum computation, communication, and metrology [44, 70, 71, 72]. In the initial proposal for the implementation of quantum networks [2], atomic internal states with long coherence times serve as “stationary” qubits, stored and locally manipulated at the nodes of the network. Quantum channels between different nodes are provided by optical fibers, which transport photons (“flying” qubits) over long distances [73]. A crucial requirement for such network protocols is the reversible mapping of quantum states between light and matter. Cavity quantum electrodynamics (QED) provides a promising avenue for achieving this capability by using strong coupling for the interaction of single atoms and photons [49].

Within this setting, reversible emission and absorption of one photon can be achieved by way of a dark-state process involving an atom and the field of a high-

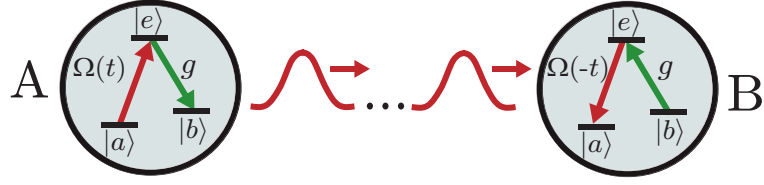


Figure 3.1: Illustration of the protocol of Ref. [2] for quantum state transfer and entanglement distribution from system  $A$  to system  $B$ . By expanding to a larger set of interconnected cavities, complex quantum networks can be realized.

finesse optical cavity. For classical fields, this “STIRAP” process was first considered twenty years ago [74, 75], before being adapted to quantum fields [76] and specifically to the coherent transfer of quantum states between remote locations [2], with many extensions since then [77]. The basic scheme, illustrated in Figure 3.1, involves a three level atom with ground states  $|a\rangle$  and  $|b\rangle$  and excited state  $|e\rangle$ . An optical cavity is coherently coupled to the atom on the  $b \leftrightarrow e$  transition with rate  $g$ , and a classical field  $\Omega(t)$  drives the atom on the  $a \leftrightarrow e$  transition. If the  $\Omega$  field is ramped adiabatically *off*  $\rightarrow$  *on*, then state  $|a, n\rangle$  evolves into  $|b, n+1\rangle$ , and state  $|b, n\rangle$  remains unchanged, where  $|a, n\rangle$ ,  $|b, n\rangle$  denotes a state in which the atom is in ground state  $a$ ,  $b$  and there are  $n$  photons in the cavity. Ramping  $\Omega$  *on*  $\rightarrow$  *off* implements the reverse transformation.

This process can be used to generate single photons by preparing the atom in  $|a\rangle$  and ramping  $\Omega$  *off*  $\rightarrow$  *on*, thereby effecting the transfer  $|a, 0\rangle \rightarrow |b, 1\rangle$  with the coherent emission of a single photon pulse from the cavity [2, 76, 78]. Essential aspects of this process have been confirmed in several experiments [16, 79, 80], including tailoring of the single-photon pulse shape [79].

A distinguishing aspect of this protocol is that it should be *reversible* [2], so that a photon emitted from one system  $A$  can be efficiently transferred to another system  $B$ . Furthermore, it should be possible to map coherent superpositions reversibly between the atom and the field:

$$(c_0|b\rangle + c_1|a\rangle) \otimes |0\rangle \leftrightarrow |b\rangle \otimes (c_0|0\rangle + c_1|1\rangle). \quad (3.1)$$

Over the past decade, single photons have been generated in diverse physical systems [81]; however, most such sources are not reversible in principle, and for those that are, no experiment has verified the reversibility of either the emission or the absorption process.

We report an important advance related to the interface of light and matter by explicitly demonstrating the reversible mapping of a coherent optical field to and from the hyperfine ground states of a single, trapped Cesium atom.<sup>1</sup> Specifically, we map an incident coherent state with  $\bar{n} = 1.1$  photons into a coherent superposition of  $F = 3$  and  $F = 4$  ground states with transfer efficiency  $\zeta = 0.057$ .<sup>2</sup> We then map the stored atomic state back to a field state. The coherence of the overall process is confirmed by observations of interference between the final field state and a reference field that is phase coherent with the original coherent state, resulting in a fringe visibility  $v_a = 0.46 \pm 0.03$  for the adiabatic absorption and emission processes. We thereby provide the first verification of the fundamental primitive upon which the protocol in Ref. [2] is based.

As shown schematically in Figure 3.2(a), our system consists of one Cs atom coupled to a high-finesse Fabry-Perot cavity. The cavity length is tuned so that a  $\text{TEM}_{00}$  mode is near resonance with the  $6S_{1/2}, F = 4 \rightarrow 6P_{3/2}, F = 3'$  transition of Cs at 852.4 nm. The maximum atom-cavity coupling rate is  $g_0/2\pi = 16$  MHz, while the cavity field and the atomic excited state decay at rates  $(\kappa, \gamma)/2\pi = (3.8, 2.6)$  MHz  $\ll g_0$ . Thus, the system is in the strong coupling regime of cavity QED [49].

Atoms are dropped from a magneto-optical trap into the cavity and cooled into a far off-resonant trap (FORT) by a blue-detuned optical lattice (see [49, 30]). The FORT excites another  $\text{TEM}_{00}$  cavity mode at the “magic” wavelength 935.6 nm, creating nearly equal trapping potentials for all states in the  $6S_{1/2}, 6P_{3/2}$  manifolds [13].

---

<sup>1</sup>This mapping could also be demonstrated by absorbing a single-photon state, but we use a coherent state instead, because its phase information allows us to verify explicitly the reversibility of the absorption process.

<sup>2</sup>Since we use a coherent state rather than a coherent superposition of  $n = 0, 1$  Fock states, equation (3.1) only approximately describes our system. For a  $\bar{n} = 0.68$  coherent state (i.e.,  $\bar{n} = 1.1$  at the face of  $M_{\text{in}}$ ), the fraction of the population in the  $n = 0, 1$  subspace is  $\simeq 0.85$ .

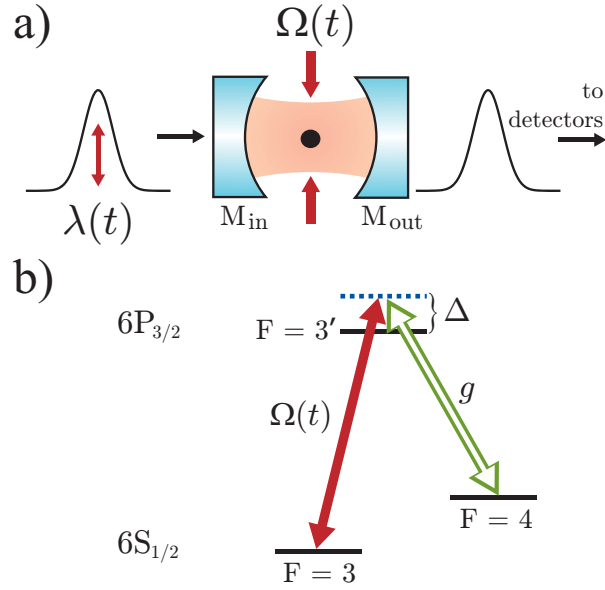


Figure 3.2: (a) Schematic of the experiment. The probe  $\lambda(t)$  resonantly drives the cavity through input mirror  $M_{in}$ ; the classical field  $\Omega(t)$  excites the atom transverse to the cavity axis. Photons emitted from the output mirror  $M_{out}$  are directed to a pair of avalanche photodiodes. (b) Atomic level diagram. Double arrow  $g$  indicates the coherent atom-cavity coupling, and  $\Omega(t)$  is the classical field. The cavity and  $\Omega$  field are blue-detuned from atomic resonance by  $\Delta$ .

An atomic level diagram is shown in Figure 3.2(b); the states used in the current scheme are ground  $F = 3, 4$  and excited  $F = 3'$  manifolds, corresponding to  $|a\rangle, |b\rangle, |e\rangle$  in Figure 3.1. The cavity is tuned to frequency  $\omega_C = \omega_{4-3'} + \Delta$ , where  $\omega_{4-3'}$  is the frequency of the  $4 - 3'$  transition, and  $\Delta/2\pi = 10$  MHz is the cavity-atom detuning. A linearly polarized probe beam<sup>3</sup> drives the cavity at frequency  $\omega_C$  with pumping strength  $\lambda(t)$ . An optical lattice drives the atom transverse to the cavity axis at frequency  $\omega_A = \omega_{3-3'} + \Delta$  to provide a classical field with Rabi frequency  $\Omega(t)$  [16]. The laser source for the optical lattice is phase-locked in Raman resonance with the probe laser, so their relative detuning  $\delta = \omega_A - \omega_C$  is phase-stable and equal to the ground-state hyperfine splitting  $\Delta_{HF} = \omega_{3-3'} - \omega_{4-3'} = (2\pi)(9.193 \text{ GHz})$ .

Our experimental procedure is as follows: after loading an atom into the FORT, we subject it to 2,000 trials lasting a total of 360 ms, where each trial consists of

<sup>3</sup>Our cavity supports two nearly degenerate modes with orthogonal linear polarizations along the  $\hat{x}$  and  $\hat{y}$  axes, where  $\hat{z}$  denotes the cavity axis. The cavity probe drives either the  $\hat{x}$  or the  $\hat{y}$  mode; a polarizer at the cavity output only allows the  $\hat{x}$  component to reach the detectors.

a series of discrete measurements performed on the atom. These measurements are used to quantify the coherence of the absorption process, as well as for calibrations and background monitoring. After these trials, we check that the atom has survived in the trap by attempting to generate 10,000 single photons, which are detected by monitoring the cavity output with two single-photon-counting avalanche photodiodes. We keep only the data from atoms that have survived all the trials. For most of the data that we keep, only a single atom is present in the trap, but occasionally two or more atoms may be loaded. From measurements performed during the 2,000 trials, we determine that at least 80% of the data presented here involve a single atom.

For each trial, we prepare the atom in  $F = 4$  and then drive the system with a series of light pulses, as shown in Figure 3.3. The classical field  $\Omega(t)$  generates pulses  $\Omega_{1,2}$ , and the cavity probe  $\lambda(t)$  generates pulses  $\lambda_{1,2}$ . For any given measurement within a trial, some of these pulses are *on* and the others are *off*. Pulse  $\lambda_1$  is the coherent state that is to be mapped into the atom. The strength of this pulse is set so that there are  $\bar{n} = 1.1$  mode-matched photons at the face of the input mirror  $M_{in}$ . Because of mirror losses [42], if no atom were present, this would give rise to a pulse inside the cavity with  $\bar{n} = 0.68$  photons. The falling edge of pulse  $\Omega_1$  is used to perform the adiabatic absorption of  $\lambda_1$ . The intensity of the lattice light is such that when  $\Omega_1$  is fully *on*, its Rabi frequency is  $\sim 8\gamma$ , a value found to maximize the adiabatic absorption probability. When  $\lambda_1$  is absorbed, some of the atomic population is transferred from  $F = 4$  to  $F = 3$ . With  $\lambda_2$  *off*,  $\Omega_2$  allows us to determine the fraction of the population that has been transferred: if the atom is in  $F = 4$ , then  $\Omega_2$  does nothing, while if the atom is in  $F = 3$ , then the rising edge of  $\Omega_2$  transfers it back to  $F = 4$  and generates a single photon. Finally, with both pulses  $\Omega_2$  and  $\lambda_2$  *on*, we verify that  $\lambda_1$  was absorbed coherently. The  $\Omega_2$ ,  $\lambda_2$  pulses act together to generate a field inside the cavity; if  $\lambda_1$  was absorbed coherently, then the amplitude of this field will depend on the relative phase  $\theta$  between  $\lambda_1$ ,  $\lambda_2$ .

This dependence can be understood by considering a simple model in which  $\Omega_2$  and  $\lambda_2$  act independently. With  $\lambda_2$  *off* and  $\Omega_2$  *on*, the  $\Omega_2$  pulse transfers the atom from a superposition of  $F = 3, 4$  into  $F = 4$  by generating a field  $\alpha$  in the cavity

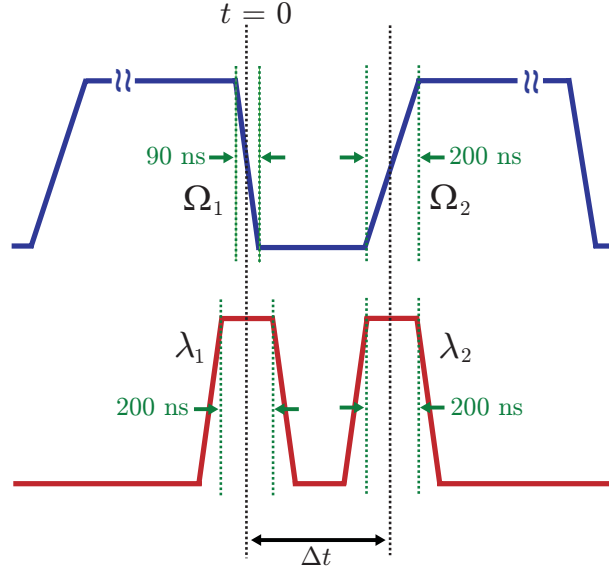


Figure 3.3: Timing diagram: the upper curve shows the  $\Omega_1$  and  $\Omega_2$  pulses; the lower curve shows the  $\lambda_1$  and  $\lambda_2$  pulses. Each of these pulses can be turned *on/off* independently. Here  $\Delta t$  is the delay between the falling edge of  $\Omega_1$  and the rising edge of  $\Omega_2$ . By enabling various combinations of these pulses, and/or varying the relative phase  $\theta$  between  $\lambda_1$  and  $\lambda_2$ , we perform different measurements on the atom. The phase  $\theta$  is set by the phase difference of RF pulses driving an acousto-optic modulator in the probe beam.

whose phase depends on the phase of the atomic superposition. In turn, the phase of the original atomic superposition is set by the phase of  $\lambda_1$ . With  $\lambda_2$  *on* and  $\Omega_2$  *off*, the  $\lambda_2$  pulse generates a field  $\beta$  inside the cavity whose phase is set by  $\lambda_2$ . If  $\Omega_2$  and  $\lambda_2$  acted independently, then when both  $\Omega_2$  and  $\lambda_2$  were *on*, the fields  $\alpha$  and  $\beta$  would combine to give a total field  $\alpha + \beta$ , whose amplitude depends on the phase difference  $\theta$  between  $\lambda_1$  and  $\lambda_2$ . Because  $\Omega_2$  and  $\lambda_2$  do not act independently, this model is only approximately correct. Nevertheless, the phase of the final field still depends on  $\theta$  for the coherent processes associated with  $\lambda_{1,2}$ ,  $\Omega_{1,2}$ .

We first consider a series of measurements which demonstrate that the  $\lambda_1$  pulse transfers more population from  $F = 4$  to  $F = 3$  in the presence of the  $\Omega_1$  pulse than in its absence. We start with the atom in  $F = 4$  and apply the  $\lambda_1$  pulse, either with the  $\Omega_1$  pulse (adiabatic absorption, which consists of both coherent and incoherent components) or without it (only incoherent absorption  $4 \rightarrow 3'$ , with spontaneous decay to  $F = 3$ ). In either case,  $\lambda_1$  transfers some population from  $F = 4$  to  $F = 3$ .

To quantify the population transfer, we apply  $\Omega_2$  and measure the probability that a single photon is detected within  $1 \mu\text{s}$  of the rising edge of  $\Omega_2$ .<sup>4</sup> We thereby infer the fraction of the atomic population that was in  $F = 3$ .<sup>5</sup> For adiabatic absorption ( $\Omega_1$  *on*), we find that the probability  $p_a$  for the atom to be transferred from  $F = 4$  to  $F = 3$  by  $\lambda_1$  is  $p_a = 0.063 \pm 0.002$ , whereas for incoherent absorption ( $\Omega_1$  *off*), the probability is  $p_i = 0.046 \pm 0.001$ . The ratio of the adiabatic to the incoherent absorption probability is  $r = p_a/p_i = 1.38 \pm 0.04$ .

As shown in Figure 3.4, we vary the arrival time  $t_1$  of the  $\lambda_1$  pulse and study the effect on the adiabatic-to-incoherent ratio  $r$ .<sup>6</sup> This ratio is maximized when  $\lambda_1$  is well aligned with the falling edge of  $\Omega_1$  at  $t = 0$ . If  $\lambda_1$  arrives too early ( $t_1 \ll 0$ ), then any population that it transfers from  $F = 4$  to  $F = 3$  is pumped back to  $F = 4$  by  $\Omega_1$ . If  $\lambda_1$  arrives too late ( $t_1 \gg 0$ ), then  $\Omega_1$  is already *off*, resulting in incoherent transfer with  $r = 1$ .

Figure 3.4 also shows the results of a computer simulation of the absorption process. The simulation predicts values for  $p_a$  and  $p_i$  and therefore the ratio  $r = p_a/p_i$ . The correspondence between our simulation and the actual measurements of  $r$  vs.  $t_1$  in Figure 3.4 is qualitatively reasonable (the only free parameter in the simulation is the atom-cavity coupling  $g$ , which we set to  $g/g_0 = 0.44$ ). The simulation can also be used to partition  $p_a$  into a coherent component  $p_a^c$  and an incoherent component  $p_a^i$ . We define the coherent component of  $r$  by  $r^c = p_a^c/p_i$ , the incoherent component of  $r$  by  $r^i = p_a^i/p_i$ , and plot  $r^c, r^i$  vs.  $t_1$  in Figure 3.4. The simulation indicates that the value of  $t_1$  for which the adiabatic absorption process is maximally coherent is roughly the value of  $t_1$  that maximizes the adiabatic transfer probability, and suggests that for this value of  $t_1$  the adiabatic absorption process has appreciable coherence, with  $r^c/r^i \simeq 1$ .

---

<sup>4</sup>For these measurements and those of Figure 3.5,  $\Delta t = 290$  ns. The probe is polarized along  $\hat{y}$ ; for the case when  $\lambda_2$  is *on*, this ensures that the emerging signal is not dominated by the component of  $\lambda_2$  that is transmitted by the cavity.

<sup>5</sup>This involves subtracting a background probability of 0.0025, which we determine by pumping the atom to  $F = 4$  and applying  $\Omega_2$ , and dividing by the single photon generation efficiency of 0.036, which we determine by pumping the atom into  $F = 3$  and applying  $\Omega_2$ .

<sup>6</sup>For these measurements,  $\Delta t = 2 \mu\text{s}$ , and the probe is polarized along  $\hat{x}$ .

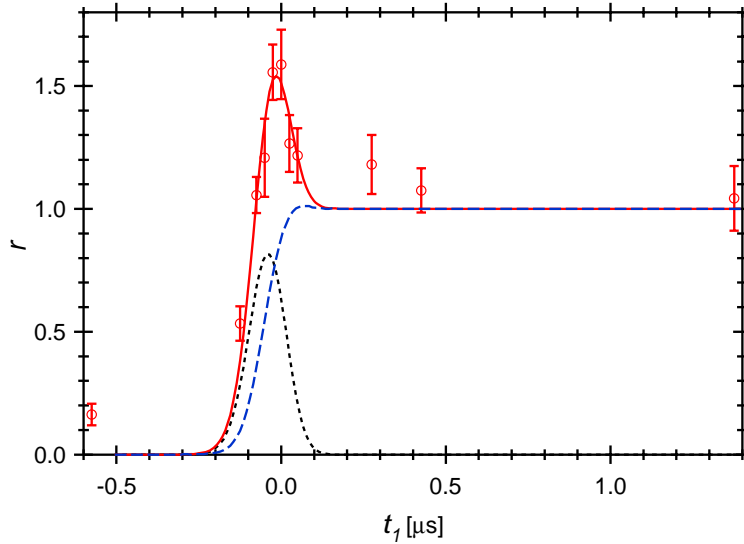


Figure 3.4: Ratio  $r$  of adiabatic transfer probability to incoherent transfer probability vs. arrival time  $t_1$  for the incident coherent pulse  $\lambda_1$ . Red data points ( $\circ$ ):  $r$  vs.  $t_1$  (experiment). Red solid curve:  $r$  vs.  $t_1$  (computer simulation). Black dotted curve: coherent component  $r^c$  vs.  $t_1$  (simulation). Blue dashed curve: incoherent component  $r^i$  vs.  $t_1$  (simulation)

In Figure 3.5, we present measurements that demonstrate that the adiabatic absorption process is indeed coherent. As before, we prepare the atom in  $F = 4$  and apply  $\lambda_1$ , either with or without  $\Omega_1$ , followed by  $\Omega_2$ . But now we add the  $\lambda_2$  pulse, which overlaps with the rising edge of  $\Omega_2$ . If the  $\lambda_1$  pulse is absorbed coherently, then the amplitude of the field generated by the combined action of  $\Omega_2$  and  $\lambda_2$  will depend on the relative phase  $\theta$  of  $\lambda_1$  and  $\lambda_2$ . By recording the cavity output from  $M_{out}$  as a function of  $\theta$  and observing this dependence, we can verify that the  $\lambda_1$  pulse was absorbed coherently. To accomplish this, we repeat the above sequence for different values of  $\theta$ , where for each relative phase, we measure the mean number of photons  $n(\theta)$  emitted from the cavity within a fixed detection window. We take data both with  $\Omega_1$  *on* and *off*, so as to obtain results  $n_a(\theta)$  and  $n_i(\theta)$  both for adiabatic and incoherent absorption. Figure 3.5 plots  $R_a(\theta) = n_a(\theta)/n_a(\theta_0)$  and  $R_i(\theta) = n_i(\theta)/n_i(\theta_0)$ , where  $\theta_0$  is a fixed phase. Note that these ratios, rather than the photon numbers themselves, are employed in order to cancel small, slow drifts in the intensity of the light beams. Significantly, we observe an appreciable phase-dependence with visibility

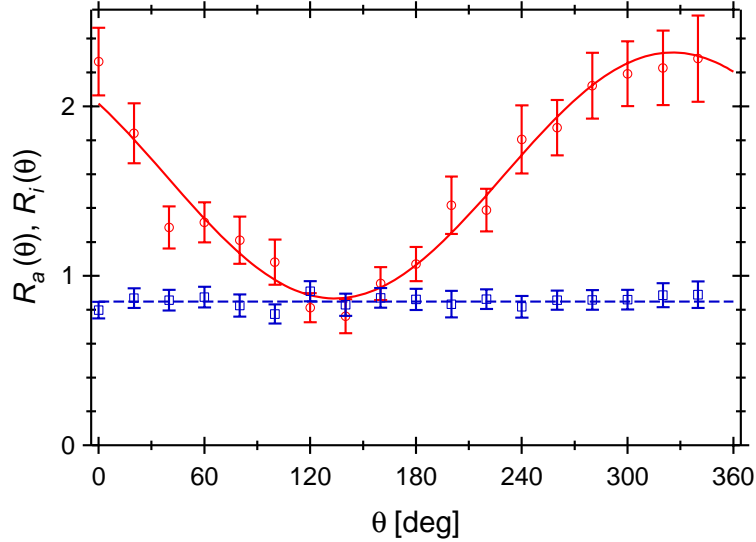


Figure 3.5: Ratios  $R_a(\theta), R_i(\theta)$  for photon generation as a function of the relative phase  $\theta$  between the  $\lambda_{1,2}$  fields. Red data points for adiabatic state transfer with  $\Omega_1$  *on*. Blue points for the incoherent process with  $\Omega_1$  *off*. The full curve is a fit to obtain the fringe visibility  $v_a \simeq 0.46 \pm 0.03$ . On average, each point represents about 130 atoms. The error bars represent statistical fluctuations from atom to atom.

$v_a = 0.46 \pm 0.03$  for the adiabatic absorption curve  $R_a(\theta)$ , while no such variation is recorded for the incoherent absorption curve  $R_i(\theta)$ .

The fringe visibility is limited by the intrinsic incoherent component of the absorption process, as well as by the mismatch in amplitudes and pulse shapes for the  $\alpha, \beta$  fields. For the results shown in Figure 3.5, a 200 ns detection window is used around the peak of the emission process. If we increase the detection window to 1  $\mu$ s, thus degrading the pulse shape overlap, the visibility drops to  $v_a = 0.18 \pm 0.01$ .

In conclusion, we have demonstrated the reversible transfer of a coherent pulse of light to and from the internal state of a single trapped atom, which represents a significant step towards the realization of quantum networks based upon interactions in cavity QED. Explicitly, we have presented a detailed investigation of the adiabatic absorption of an incident coherent state with  $\bar{n} = 1.1$  photons. A fraction  $p_a = 0.063$  of the atomic population has been transferred from  $F = 4$  to  $F = 3$ , with the efficiency of the transfer being  $\zeta \equiv p_a/\bar{n} = 0.057$ . Here  $\zeta$  provides an estimate of the efficiency that could be obtained if we adiabatically absorbed a single photon state instead of

a coherent state, and should be compared to the much lower efficiencies possible in free space.

The factors that limit the transfer efficiency include the passive mirror losses [42], the fact that our cavity mirrors  $M_{in}, M_{out}$  have equal transmission coefficients  $T_{in} = T_{out}$  (as opposed to  $T_{in} \gg T_{out}$  for a single-sided cavity), and the coupling of the atom to both polarization modes of the cavity. Even in the ideal case without scatter and absorption losses in the mirrors, for a three-level atom coupled to a two-sided cavity ( $T_{in} = T_{out}$ ) with two modes, the maximum possible adiabatic transfer probability would be  $\zeta = 0.25$ . By implementing a single-sided cavity with losses as achieved in Ref. [8], we estimate that  $\zeta$  could be improved to  $\zeta \sim 0.9$  for coupling schemes with a single polarization.

## 3.2 Pulse combinations

The measurements described above consisted of trapping an atom and preparing it in one of two hyperfine manifolds, followed by combinations of the four pulses  $\Omega_1$ ,  $\Omega_2$ ,  $\lambda_1$ , and  $\lambda_2$  shown in Figure 3.3. Specifically, we employed eight configurations in which  $\Omega_2$  was always on, the other three pulses were either on or off, and the phase between  $\lambda_1$  and  $\lambda_2$  was either fixed or varied (or not applicable, in the case of only one  $\lambda$  pulse). These possibilities are enumerated in Table 3.1. Note that during a single 360 ms trapping interval, an atom would be subject to all eight pulse combinations 2000 times, with appropriate preparation of the atomic state preceding each combination. This section focuses on the information that we are able to extract from each set of pulses.

Cases 1 and 2 in Table 3.1 correspond to times  $t_1 \gg 0$  and  $t_1 = 0$  in Figure 3.4. In case 1, the atom is prepared in  $F = 4$ ; since the cavity is tuned to  $F = 4 \rightarrow F' = 3$ , we expect the vacuum Rabi splitting to shift the incoming pulse  $\lambda_1$  out of resonance with the system. In the absence of  $\Omega_1$ ,  $\lambda_1$  will only transfer population to  $F = 3$  through incoherent, off-resonant excitation of the atom. The probability of this population transfer is measured by attempting to generate a single photon using  $\Omega_2$ , which will

#	$F_{start}$	$\Omega_1$	$\lambda_1$	$\lambda_2$	$\theta$	measured probability
1	4	off	on	off	n/a	incoherent absorption
2	4	on	on	off	n/a	coherent and incoherent absorption
3	4	on	on	on	$\theta_0$	adiabatic fringe, fixed phase
4	4	on	on	on	$\theta$	adiabatic fringe, variable phase
5	3	off	off	off	n/a	single photon generation
6	4	off	off	off	n/a	background
7	4	off	on	on	$\theta_0$	incoherent fringe, fixed phase
8	4	off	on	on	$\theta$	incoherent fringe, variable phase

Table 3.1: The series of eight pulse combinations applied to each atom in the reversible state transfer experiment.  $F_{start}$  is the hyperfine manifold in which the atom is prepared before the pulses are applied.

succeed only if the atom is in  $F = 3$ . In case 2, the inclusion of a classical pulse  $\Omega_1$  means that now we expect the coherent Raman process to transfer population from  $F = 4$  to  $F = 3$ , though of course incoherent excitation will still be possible. The relative probability to generate photons in these two cases reflects the extent to which our mapping process is coherent. While our system is in the strong coupling regime, we are limited by the fact that  $g$  is not larger, which means that some off-resonant light from  $\lambda_1$  can enter the cavity. The maximum atom-cavity coupling for our system on the  $F = 4 \rightarrow F' = 5$  transition is  $g_{max} = 33.9$  MHz, but the single-photon generation scheme constrains us to the  $F = 4 \rightarrow F' = 3$  transition ( $g_0 = 16$  MHz), and the variation of  $g$  over the range of FORT wells and atomic motion result in an inferred coupling  $g_0 = 7$  MHz, only a factor of two greater than the cavity linewidth.

Cases 3 and 4 are the basis for the data presented in Figure 3.5. We map the coherent pulse  $\lambda_1$  onto the atom by means of  $\Omega_1$ ; then, while attempting to generate a single photon with  $\Omega_2$ , we introduce the pulse  $\lambda_2$ .  $\lambda_2$  interferes either constructively or destructively with the photon generation process as a function of  $\theta$ , which in case 4 is varied over  $2\pi$ . In case 3,  $\theta$  is held fixed at an arbitrary value  $\theta_0$ , so the photon generation probability should in principle be constant. We compensate for small drifts in the probe power over the course of the experiment by expressing the phase variation as the ratio of the case 4 to case 3 data for each atom.

Case 5, in which we simply use  $\Omega_2$  to generate single photons on demand, provides us with a calibration of the photon generation efficiency. In case 6, we again attempt to generate single photons, but with the atom in the wrong hyperfine manifold, so that we expect nothing to happen. We then subtract this measured background value from the data obtained in all other cases.

Finally, cases 7 and 8 provide a baseline for comparison with cases 3 and 4. Because  $\Omega_1$  is omitted, we expect that the process that transfers population to  $F = 3$  is strictly incoherent; that is, it should have no phase dependence. We confirm this by varying the relative phase of  $\lambda_1$  and  $\lambda_2$  and observing no change in photon generation probability. These data are also plotted for comparison in Figure 3.5; as in cases 3 and 4, we divide the probability with variable phase by the probability with fixed phase for each atom to remove the effects of probe drift. This reflects a more general strategy of cycling repeatedly through the full range of experimental parameters rather than performing various measurements sequentially in the course of a data run. As a result, we are less sensitive to long-term drift and can obtain real-time information about the progress of the experiment. Another example of this strategy, increasing the phase  $\theta$  in  $20^\circ$  steps between each atom loading event, is discussed in Section 3.5.

### 3.3 Timing

Reversible state transfer was the first lab 11 experiment that required more complicated timing than the ADwin alone could provide. The ADwin can produce pulses as short as 100 ns; however, the length of any pulse shorter than a few  $\mu s$  should be confirmed on an oscilloscope, as it may be up to 1  $\mu s$  shorter or longer than specified by the control program. In the present case, we had two requirements: (a) we needed to generate a pair of adiabatic pulses  $\Omega_{1,2}$  from the side of the cavity that would turn on and off over hundreds of ns, and (b) we needed the timing of these pulses to be stable with respect to  $\lambda_{1,2}$ , the pair of coherent state pulses along the cavity axis. (We did not take special care to generate  $\lambda_{1,2}$  adiabatically, as we found that the temporal pulse shape that resulted from switching the probe AOM with TTL logic

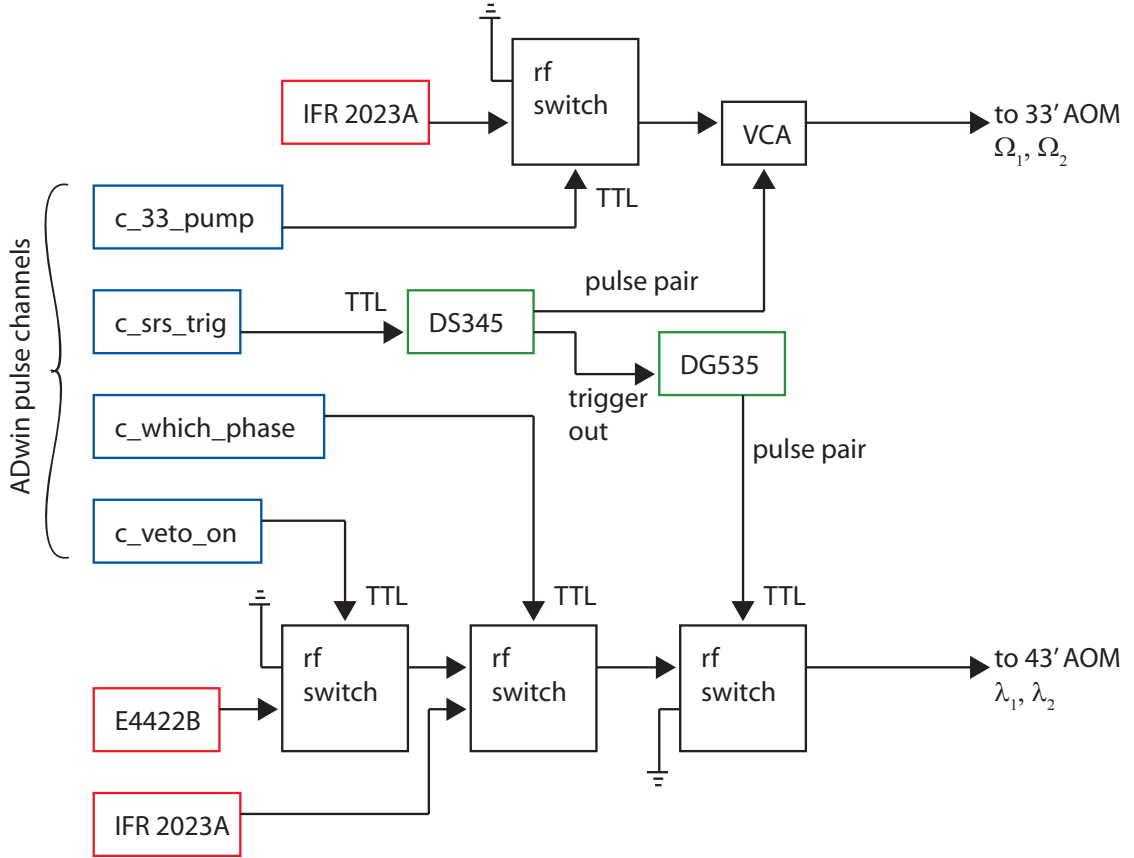


Figure 3.6: Instrumentation diagram for the generation of  $\Omega_{1,2}$  and  $\lambda_{1,2}$  pulses

was a reasonable approximation to the shape of photons generated in Ref. [16].)

As shown in Figure 3.6, timing was controlled by four digital logic output channels on the ADwin. Channel `c_srs_trig` triggered a single sweep of a Stanford Research Systems (SRS) DS345 function generator. The DS345 can be programmed to generate arbitrary waveforms; in this case, we set the output to shape the two  $\Omega$  pulses shown in Figure 3.3. The pulse pair then provided the control input for a voltage-controlled attenuator (VCA). A second channel, `c_33_pump`, controlled the RF input to the VCA and thus regulated whether one or both of the pulses would drive the  $F = 3 \rightarrow F = 3'$  AOM. Meanwhile, the  $\lambda_{1,2}$  pulse pair was generated by a pre-programmed SRS DG535 pulse generator using the logical AND of its two pulse outputs. A single sweep of the DG535 was triggered by the DS345 rather than directly by the ADwin in order to avoid  $\sim 25$  ns jitter between the pulse pairs due to the DS345 clock

rate. Two other ADwin channels controlled RF switches in the  $\lambda_{1,2}$  path: the first, `c_which_phase`, determined which of two signal generators would provide the RF source; both signal generators were set to the same frequency, but one (IFR 2023A) had a fixed phase, while the phase of the other (Agilent E4422A) was variable. A second switch, `c_veto_on`, performed the same function as `c_33_pump`, determining whether none, one, or both of the pulses would be able to pass to the  $F = 3 \rightarrow F' = 4'$  AOM.

### 3.4 Phase stability

Our first attempts to generate a fringe using both  $\Omega_{1,2}$  and  $\lambda_{1,2}$  were not successful, though the data suggested some underlying phase-dependent periodicity. We realized that the Raman process underlying photon absorption and generation relied on the relative phase of  $\Omega(t)$ , the  $F = 3 \rightarrow F' = 3$  lattice, and  $\lambda(t)$ , the source of  $F = 3 \rightarrow F' = 4$  pulses along the cavity axis. While  $\lambda(t)$  was derived from the master (probe) laser,  $\Omega(t)$  was generated by the repump laser, which at the time had a separate lock to the cesium saturated-absorption spectrum. Luckily, the electronic phase lock that we had formerly used to synchronize the FORT and Raman lasers had been decommissioned during the ground state cooling experiment in favor of a quieter injection lock (Section 2.2.1). We resurrected it in order to set up a phase lock between the master laser and the repump: auxiliary beams from both lasers were combined on a fiber beamsplitter whose output was focused onto a 25 GHz photodetector (New Focus 1417). In the same configuration used previously for the Raman lock, the optical beat note from these two lasers was mixed down at  $\Delta_{HF}$  and provided feedback signals for the repump laser's diode current and piezo voltage.

The fringe measurement also depended on a stable, programmable phase relationship  $\theta$  between  $\lambda_1$  and  $\lambda_2$ . The two signal generators for  $\lambda_1$  and  $\lambda_2$  (Figure 3.6) were set to provide the same output frequency and were phase-referenced to one another using a 10 MHz input/output. In order to confirm relative phase stability, we monitored the outputs of the two sources (set to a fixed relative phase) over the course

of two days on a fast oscilloscope and found the long-term phase drift to be between 0.02 and 0.05 radians/hour. The data shown in Figure 3.5 were acquired over the course of about three hours, so we would expect drifts of  $< 0.15 \text{ rad} \approx 2 \text{ degrees}$  during this time frame.

A second verification of the phase stability was provided by an optical interferometer formed by the shifted (first-order) and unshifted (zeroth-order) beams at the output of the  $F = 4 \rightarrow F' = 3$  AOM, driven by one of the two RF sources. We generally use an iris to block all but the first-order beam, but with the iris opened, the two beams could beat against one another when they were recombined after being double-passed through the AOM. The beat note, at twice the RF input frequency, was then observed to be phase-stable on an oscilloscope with respect to the second RF source.

### 3.5 Remote programming capabilities

One important technical development for this experiment was the ability to program electronic equipment remotely via serial commands sent from the ADwin. During the ground-state cooling experiment, we had adjusted the Raman frequency detuning by hand on an IFR (Aeroflex) 2023A signal generator. That process grew increasingly time consuming, however, as our experiments became more complicated.

We now include ASCII strings as text in the code that controls our experiment. For example, the instructions

```
0.0 'text = ":PHASe "'
0.0 inline 'serial_partial_out (9)'

0.0 inline 'lngtostr (10*(i-1), text)'
0.0 inline 'serial_partial_out (9)'

0.0 inline 'text = " DEg"'
0.0 inline 'serial_out (9)'
```

tell the Agilent E4422B signal generator at time 0.0 to set the phase of its output frequency to  $10 * (i - 1)$  degrees, where  $i$  is an integer between 1 and 18. (As the RF signal drives a double-passed AOM, an RF phase shift of  $180^\circ$  is equivalent to an optical phase shift of  $360^\circ$ .) The subroutines `serial_partial_out` and `serial_out` send the ASCII characters as TTL pulses on a specified ADwin channel (in this case, channel 9), followed by either a carriage return or a line feed to signal the end of the command. A home-built circuit based on a Texas Instruments MAX232N chip then converts the TTL pulses to signals on an RS-232 serial cable. The serial cable can be used either to drive devices directly (for example, the Aeroflex and Agilent signal generators) or to drive GPIB-controlled devices such as the DG535. In the latter case, we use an RS232-to-GPIB converter manufactured by National Instruments.

In the process of data acquisition, we run a loop which increments  $i$  on an atom-by-atom basis. In addition to writing time-stamped photon counts to two channels of the P7888 card, we write the value of  $i$  to a third channel. The data analysis programs that David Boozer has written then separate the atoms into bins indexed by the value of  $i$ .

Our first remote programming applications in the lab were automated frequency sweeps (in order to record Raman spectra) and phase shifts (to observe the coherence fringe in the current experiment). More recently, we have generated pulse trains of variable lengths and delays in order to measure, for example, Rabi flops and Ramsey fringes. We have also extended our frequency sweeps to the microwave domain, where they enable us to search for narrow resonance features (Chapter 5).

## 3.6 Mapping single photons

We return now to consider the original plan to map cavity-generated photons back onto a trapped atom. Figure 3.7 outlines a scheme that would allow us to realize this in the laboratory. A photon exiting the cavity passes (with probability 1/2) through a nonpolarizing beamsplitter cube (NPBS), a Faraday rotator, and a PBS into an optical delay line, which would provide a necessary buffer for the experiment timing.

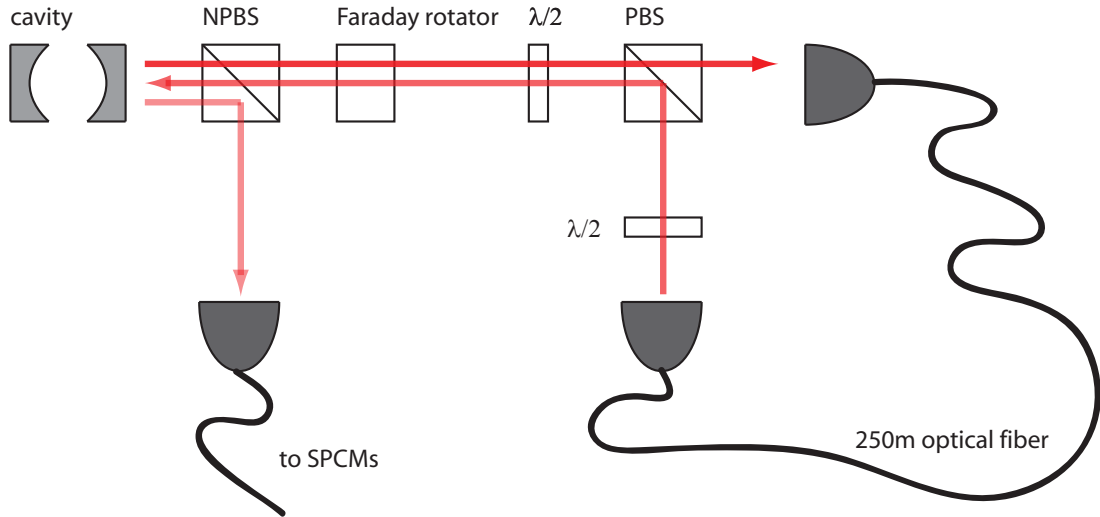


Figure 3.7: Possible output path configuration in order to generate single photons on demand, then map them back into the cavity

At the fiber output a few microseconds later, a half-waveplate rotates the photon so that it reflects off the PBS and retraces its earlier path. A second pass through the Faraday rotator corrects for the waveplate rotation, and the photon re-enters the cavity in its original polarization state.

Half of all photons at the cavity output reflect off the NPBS, where they can be detected by one or more SPCMs; this includes both photons generated within the cavity and returning photons that are not absorbed. The initial step to characterize photon reabsorption into the cavity would be to monitor returning reflected photons at this port. As the timing of the adiabatic classical field  $\Omega_1$  is adjusted so that it is synchronous with the returning photons, we would expect to see a reflection dip. One could then attempt to confirm photon reabsorption directly by generating a second photon in the cavity, which would only occur if the first photon had transferred the atom back to its initial hyperfine state.

It is important to acknowledge the inefficiency of this scheme, which is nevertheless the most promising one we have found. Table 3.2 enumerates losses at each stage of the proposed experiment after generation of an initial photon within the cavity mode, which we assume occurs on every attempt. We see that detection of a second photon

Propagation step	Efficiency
cavity escape (mirror losses)	0.6
symmetric cavity	0.5
NPBS	0.5
Faraday rotator	0.93
free space propagation (filters)	0.66
single-mode fiber coupling	0.7
propagation through 250 m single-mode fiber	0.75
polarization drift in fiber	0.98
Faraday rotator, second pass (includes polarization error)	0.89
NPBS	0.5
after reflection from cavity, NPBS	0.5
free space propagation (filters)	0.66
single-mode fiber coupling	0.7
SPCM quantum efficiency	0.5
<b>probability to detect reflected photons</b>	<b>0.0024</b>
cavity entrance (mirror losses)	0.6
symmetric cavity	0.5
cavity escape (mirror losses)	0.6
<b>probability to detect a second photon</b>	<b>0.0004</b>

Table 3.2: Path efficiencies in mapping a photon back into the cavity. We consider detection via both reflection from the cavity (in the absence of a synchronous classical mapping field) and generation of a second photon upon successful mapping.

would be roughly 100 times less efficient than single photon generation. It would thus be a challenge to optimize various parameters of the experiment (for example, timing of  $\Omega_1$ ) based on detection efficiency. In future cavity systems, of course, the possible changes mentioned in Section 3.1 — namely, the use of a single-sided cavity with reduced scattering and absorption losses — would improve the efficiency with every pass in or out of the cavity.

Other prospects include mapping cavity-generated photons onto the ensemble of cesium atoms in the lab 2 experiment, thus generating entanglement between the hyperfine states of our trapped atom and the atomic ensemble. In this case, however, we would prefer to have the atom’s hyperfine states entangled with photon polarization states rather than the Fock states ( $|0\rangle, |1\rangle$ ), as polarization states are more robust to path losses. Schemes for cavity-QED generation of polarization-entangled photons

[4, 82, 83] require the ability to prepare the atom in a specific Zeeman sublevel, something that has been a challenge for us in the past. Chapter 4 describes our recent progress in Zeeman state preparation of single atoms, while Chapter 5 discusses our subsequent characterization of Raman transitions between Zeeman levels, including steps toward polarization entanglement.

## Chapter 4

# Atom preparation: optical pumping and conditional loading

This chapter presents two significant advances in our ability to prepare trapped atoms within an optical cavity. First, we demonstrate that we can use Raman transitions to pump a trapped atom into any desired Zeeman state. Second, we introduce a feedback scheme for conditioning our experiment on the presence of at most one atom in the cavity. When combined with a new Raman-based cavity loading method which allows us to trap multiple atoms consistently, this scheme allows us to perform single-atom experiments after almost every MOT drop.

While there exist well-known methods for optically pumping atoms in free space, we have struggled to implement them in our lab. These conventional methods rely on classical fields which address both hyperfine manifolds of the atom, and we have used the lattice beams as well as linearly polarized light from the side of the cavity for this purpose. One source of our difficulties may be the Zeeman-dependent AC Stark shift which the FORT induces in the excited states of the atom [39]; this potentially leads to mixing of the excited-state Zeeman populations during the optical pumping process. In addition, recent calculations suggest that diffraction of beams focused into the cavity from the side results in significant intensity variation along the cavity axis.

After a series of frustrating optical pumping attempts in the cavity, we realized that it might be better to study our techniques first in the simpler setting of a MOT.

We rehabilitated the old lab 1 upper vacuum chamber for this purpose, and undergraduate Eric Tai is currently working with Dal in lab 9 to explore free-space optical pumping. In the meantime, we have found an alternative method of preparing atoms in a specific Zeeman state, presented in Sections 4.1 and 4.2: by driving incoherent Raman transitions across a specifically chosen frequency range, we can create a tunable dark state for population trapping. Not only does our new scheme avoid the problems associated with side beams and excited-state mixing, but also it no longer restricts us to the Zeeman levels  $m_F = 0, +F, -F$  as in conventional optical pumping.

Variation in intracavity atom number is another bugbear of the experiment which in the past has been only indirectly confronted. The number of atoms loaded into the FORT after each MOT drop is believed to obey Poissonian statistics over the course of a data run. Therefore, if we can establish a maximum acceptable level of events with two or more atoms present, we can simply turn down the loading rate (and thus, the average atom number  $\bar{N}$  in the Poissonian distribution) until this threshold is met. (In practice, this is accomplished by attenuating the power in the lattice beams which cool atoms into the FORT, so that cooling is less effective.) However, we must rely on an unfortunate trade-off between two-atom contamination and data acquisition time. For example, 90.8% of all trials in the single photon generation experiment were discarded because they had no atoms, and the experiment thus required almost a day of continuous data acquisition; nevertheless, the effects of two-atom events could still be seen in the photon statistics [16, 39]. In order to decouple these two parameters, we introduce a real-time measurement of atom number which allows us to enforce the condition  $N < 2$  before the experiment begins (Sections 4.3 and 4.4).

## 4.1 Optical pumping via incoherent Raman transitions

The following section has been adapted from Ref. [32].

A new optical pumping scheme is presented that uses incoherent Raman tran-

sitions to prepare a trapped cesium atom in a specific Zeeman state within the  $6S_{1/2}, F = 3$  hyperfine manifold. An important advantage of this scheme over existing optical pumping schemes is that the atom can be prepared in any of the  $F = 3$  Zeeman states. We describe an experimental implementation of the scheme and show that a fraction  $0.57 \pm 0.02$  of the total population can be prepared in the desired state, with the remaining population distributed fairly uniformly among the six other states. We demonstrate the scheme in the context of cavity quantum electrodynamics, but the technique is equally applicable to a wide variety of atomic systems with hyperfine ground-state structure.

### 4.1.1 Introduction

Many experiments in atomic physics rely on the ability to prepare atoms in specific internal states. For example, spin-polarized alkali atoms can be used to polarize the nuclei of noble gases [84], to act as sensitive magnetometers [85], and to provide frequency standards that exploit magnetic-field-insensitive clock transitions [86]. In the field of quantum information science, internal atomic states can be used to store and process quantum bits [1, 2, 34, 87, 88] with extended coherence times.

A standard method for preparing an atom in a specific internal state is optical pumping [89, 90, 91], which involves driving the atom with light fields that couple to all but one of its internal states; these light fields randomly scatter the atom from one internal state to another until it falls into the uncoupled “dark” state. Various optical pumping schemes have been analyzed and demonstrated for alkali atoms [92, 86, 93] and today are well-established techniques. These schemes rely on dark states that are set by the polarization of the driving field, and this imposes restrictions on the possible Zeeman states in which the atom can be prepared. Specifically, one can prepare the atom in the  $m_F = 0$  state by using light that is linearly polarized along the quantization axis, or in one of the edge states ( $m_F = \pm F$ ) by using light that is circularly  $\sigma_{\pm}$ -polarized along the quantization axis.

In contrast, the scheme presented here allows the atom to be prepared in any

of the Zeeman states within the lowest ground state hyperfine manifold of an alkali atom, which in our case is the  $6S_{1/2}, F = 3$  manifold of cesium. The key component of the scheme is a pair of optical fields that drive Raman transitions between pairs of Zeeman states  $|3, m\rangle \leftrightarrow |4, m\rangle$ . We apply a magnetic bias field to split out the individual Zeeman transitions and add broadband noise to one of the optical fields, where the spectrum of the noise is tailored such that all but one of the transitions are driven. The two Zeeman states corresponding to the undriven transition are the dark states of the system, and we exploit these dark states to perform optical pumping. We verify the optical pumping by using coherent Raman transitions to map out a Raman spectrum, which allows us to determine how the atomic population is distributed among the different Zeeman states; these measurements show that a fraction  $0.57 \pm 0.02$  of the total population is prepared in the desired state, with the remaining population distributed fairly uniformly among the six other states. The capability of driving Raman transitions between hyperfine ground states has many additional applications, such as state manipulation [94], ground-state cooling [30, 33, 35, 37], precision measurements [95, 96], and Raman spectroscopy [97]. The scheme described here shows that this versatile tool can also be used for atomic state preparation.

We have demonstrated this scheme in the context of cavity quantum electrodynamics (QED), specifically in a system in which a single atom is strongly coupled to a high-finesse optical cavity. Cavity QED offers a powerful resource for quantum information science, and the ability to prepare the atom in a well-defined initial state is a key requirement for many of the protocols that have been proposed for this system, such as the generation of polarized single photons [4, 82] and the transfer of Zeeman coherence to photons within the cavity mode [76]. Conventional optical pumping to a single Zeeman sublevel has been previously demonstrated within a cavity [83], but we find our new method to be particularly effective given the constraints of our system, in which optical access to the atom is limited and we must address the large multiplicity of cesium sublevels. However, optical pumping via incoherent Raman transitions has much broader applications beyond the cavity QED setting and can be

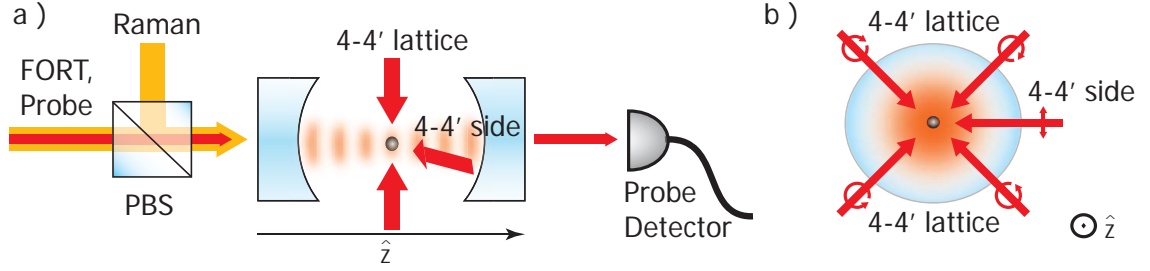


Figure 4.1: Schematic of experiment. (a) View from the side of the cavity. Shown are the linearly polarized FORT, Raman, and probe beams that drive the cavity, and the circularly polarized 4 – 4' lattice beams and linearly polarized 4 – 4' side beam that drive the atom. (b) View along the cavity axis. Shown are the 4 – 4' lattice beams and the 4 – 4' side beam.

used in a wide variety of atomic systems with hyperfine ground-state structure.

### 4.1.2 Experimental apparatus

Our system consists of a single cesium atom that is strongly coupled to a high-finesse optical cavity, as shown in Figure 4.1. The cavity supports a set of discrete modes, and its length is tuned so that one pair of modes <sup>1</sup> is nearly resonant with the atomic transition  $6S_{1/2}, F = 4 \rightarrow 6P_{3/2}, F = 5'$  at  $\lambda_{D2} = 852\text{ nm}$  (see the level diagram shown in Figure 4.2). The atomic dipole associated with this transition couples to the electric field of the resonant mode, allowing the atom and cavity to exchange excitation at a characteristic rate  $g = (2\pi)(34\text{ MHz})$  for the  $6S_{1/2}, F = 4, m_F = 4 \rightarrow 6P_{3/2}, F = 5', m_{F'} = 5$  transition, a rate that is much larger than either the cavity decay rate  $\kappa = (2\pi)(3.8\text{ MHz})$  or the atomic decay rate  $\gamma = (2\pi)(2.6\text{ MHz})$ ; thus, the system is in the strong-coupling regime [49].

We hold the atom inside the cavity via a state-insensitive far off-resonance trap (FORT) [13]. The FORT is produced by resonantly driving a cavity mode at  $\lambda_F = 936\text{ nm}$  with a linearly polarized beam, which creates a red-detuned standing wave inside the cavity. Each antinode of this standing wave forms a potential well in which an atom can be trapped; for the experiments described here, the optical power of the

<sup>1</sup> Since there are two polarization degrees of freedom, the cavity modes occur in nearly degenerate pairs.

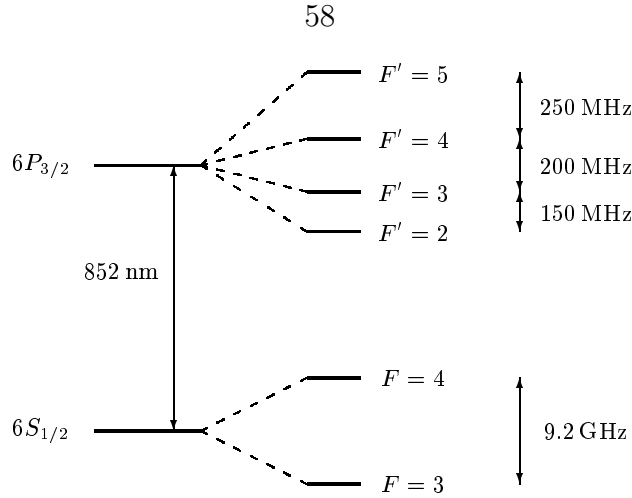


Figure 4.2: Level diagram for the  $D2$  line in cesium

FORT beam is chosen such that the depth of these wells is  $U_F = (2\pi)(45 \text{ MHz})$ .

We drive Raman transitions between the  $F = 3$  and  $F = 4$  hyperfine ground-state manifolds of the atom by adding a second beam, referred to here as the Raman beam, which drives the same cavity mode as the FORT beam but is detuned from the FORT by the atomic hyperfine splitting  $\Delta_{HF} = (2\pi)(9.2 \text{ GHz})$  (this scheme was first proposed in [19] and was used to perform Raman sideband cooling in [17]). The FORT and Raman beams are combined on a polarizing beam splitter (PBS) before entering the cavity, so the Raman beam is linearly polarized in a direction orthogonal to the polarization of the FORT beam. To stabilize the frequency difference between the FORT and Raman beams, the external-cavity diode laser that generates the Raman beam is injection-locked to the red sideband of light that has been picked off from the FORT beam and passed through an electro-optical modulator (EOM), which is driven at  $\Delta_{HF}$ . The FORT and Raman beams form the two legs of a Raman pair and drive Raman transitions between pairs of Zeeman states  $|3, m\rangle \leftrightarrow |4, m\rangle$ , where the quantization axis  $\hat{z}$  is chosen to lie along the cavity axis<sup>2</sup>. Typically we use a strong FORT beam and a weak Raman beam, so the Raman beam does not significantly alter the FORT trapping potential<sup>3</sup>.

<sup>2</sup> The FORT-Raman pair generates a Raman coupling between the hyperfine ground states that is proportional to  $\vec{J} \cdot (\hat{\epsilon}_F \times \hat{\epsilon}_R)$ , where  $\vec{J}$  is the electron angular momentum operator and  $\hat{\epsilon}_F, \hat{\epsilon}_R$  are the polarization vectors for the FORT and Raman beams, so in general  $\Delta m = \pm 1, 0$  transitions are possible [19]. For our system  $\hat{\epsilon}_F \times \hat{\epsilon}_R = \hat{z}$ , so only the  $\Delta m = 0$  transitions are driven.

<sup>3</sup> The FORT and Raman beams give level shifts  $U_F \sim \Omega_F^2/\Delta$  and  $U_R \sim \Omega_R^2/\Delta$ , and the effective

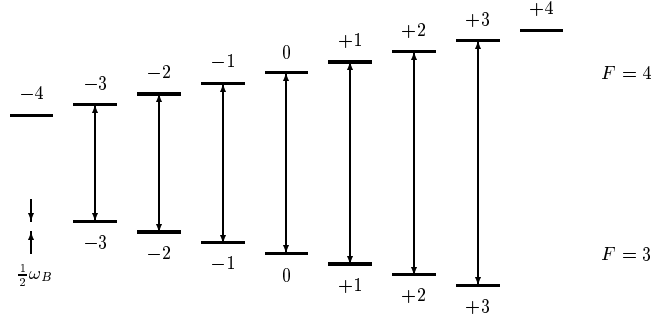


Figure 4.3: Ground state spectrum of cesium in the presence of an axial bias field. The Raman coupling drives transitions between pairs of Zeeman states  $|3, m\rangle \leftrightarrow |4, m\rangle$ , as indicated by the arrows.

In order to address individual Zeeman transitions, we apply a magnetic bias field  $B_a$  along the cavity axis. As shown in Figure 4.3, this axial field shifts the  $|3, m\rangle \leftrightarrow |4, m\rangle$  transition by

$$\delta(|3, m\rangle \leftrightarrow |4, m\rangle) = \omega_B m, \quad (4.1)$$

where

$$\omega_B \equiv (g_4 - g_3)\mu_B B_a = (2\pi)(700 \text{ kHz/G}) B_a, \quad (4.2)$$

and  $g_4 = 1/4$ ,  $g_3 = -1/4$  are the Lande  $g$ -factors for the  $F = 4$  and  $F = 3$  ground-state hyperfine manifolds. For the experiments described here, we typically set the axial bias field such that  $\omega_B \simeq (2\pi)(910 \text{ kHz})$ .

The strong atom-cavity coupling allows us to determine whether the atom is in the  $F = 3$  or  $F = 4$  hyperfine manifold by driving the cavity with a  $100 \mu\text{s}$  pulse of resonant  $4 - 5'$  probe light, as described in [30]. If the atom is in  $F = 4$ , it couples to the cavity and blocks the transmission of the probe beam, while if the atom is in  $F = 3$ , it decouples from the cavity, and the probe beam is transmitted. Using this technique, we can determine the hyperfine ground state of the atom with an accuracy

---

Rabi frequency for the Raman transitions driven by the FORT-Raman pair is  $\Omega_E \sim \Omega_F \Omega_R / \Delta$ , where  $\Omega_{F,R}$  are the Rabi frequencies of the FORT and Raman beams and  $\Delta$  is the detuning from atomic resonance. Thus, the ratio of the level shifts is  $U_R/U_F \sim (\Omega_E/U_F)^2 \sim 10^{-5}$  for the typical values  $U_F = (2\pi)(45 \text{ MHz})$ ,  $\Omega_E = (2\pi)(120 \text{ kHz})$ .

of  $\sim 98\%$  for a single  $100\ \mu\text{s}$  measurement interval.

Atoms are delivered to the cavity by releasing a magneto-optical trap located a few millimeters above the cavity, and the falling atoms are loaded into the FORT by cooling them with  $4 - 4'$  lattice light. This lattice light consists of two pairs of counter-propagating beams in the  $\sigma_+ - \sigma_-$  configuration, which are applied from the sides of the cavity. We ensure that only one atom is trapped in the FORT by applying the Raman beam and driving the cavity with a resonant  $4 - 5'$  probe; this combination gives an effect analogous to that in [18], which allows us to determine the number of atoms in the cavity based on the amount of  $4 - 5'$  light that is transmitted.

### 4.1.3 Coherent and incoherent Raman transitions

If the FORT and Raman beams are both monochromatic, then they drive coherent Raman transitions between pairs of Zeeman states  $|3, m\rangle \leftrightarrow |4, m\rangle$ , and the atomic populations oscillate between the two states in each pair. The effective Rabi frequency for the  $|3, m\rangle \leftrightarrow |4, m\rangle$  transition is

$$\Omega_E(|3, m\rangle \leftrightarrow |4, m\rangle) = \Omega_0 (1 - m^2/16)^{1/2}, \quad (4.3)$$

where  $\Omega_0$  is set by the power in the FORT and Raman beams [19]. For the experiments described here, the powers in these beams are chosen such that that  $\Omega_0 \simeq (2\pi)(120\ \text{kHz})$ . The Raman detuning for the FORT-Raman pair is given by  $\delta_R = \omega_F - \omega_R - \Delta_{HF}$ , where  $\omega_F$  and  $\omega_R$  are the optical frequencies of the FORT and Raman beams, which means that the effective detuning for the  $|3, m\rangle \leftrightarrow |4, m\rangle$  transition is

$$\delta_E(|3, m\rangle \leftrightarrow |4, m\rangle) = \delta_R - \omega_B m. \quad (4.4)$$

We can also drive incoherent Raman transitions by using a monochromatic FORT beam and a spectrally broad Raman beam, where the spectral width is typically  $\sim 10\ \text{MHz}$ . In contrast to coherent Raman transitions, in which the atom undergoes

coherent Rabi oscillations, for incoherent Raman transitions the atomic population decays at a constant rate from  $|3, m\rangle \rightarrow |4, m\rangle$  and from  $|4, m\rangle \rightarrow |3, m\rangle$ . In Section 4.1.7, we show that these decay rates are proportional to  $S(\Delta_{HF} + \omega_B m)$ , where  $S(\omega)$  is the power spectrum of a beat note formed between the FORT and Raman beams.

#### 4.1.4 Measuring the population distribution

Given an initial state of the atom in which the entire population lies in the  $F = 3$  manifold, we can use coherent Raman transitions to determine how the population is distributed among the various Zeeman states. To perform this measurement we prepare the atom in the desired initial state, apply a coherent Raman pulse of fixed duration, Rabi frequency, and Raman detuning, and then drive the cavity with a resonant  $F = 4 \rightarrow F = 5'$  probe beam to determine if the atom was transferred to  $F = 4$ . By iterating this process, we determine the probability  $p_4$  for the atom to be transferred by the Raman pulse, and by repeating the probability measurement for different Raman detunings  $\delta_R$  we can map out a Raman spectrum  $p_4(\delta_R)$ . For the Raman spectra presented here, the Raman pulses have Rabi frequency  $\Omega_0 = (2\pi)(120 \text{ kHz})$  and duration  $25 \mu\text{s}$ . This is long enough that the Rabi oscillations decohere, and the Raman spectrum just records the Lorentzian envelope for each Zeeman transition.<sup>4</sup> Thus, when the  $|3, m\rangle \leftrightarrow |4, m\rangle$  Zeeman transition is resonantly driven by the Raman pulse, roughly half the population that was initially in  $|3, m\rangle$  is transferred to  $|4, m\rangle$ .

As a demonstration of this technique, Figure 4.4 shows a Raman spectrum for an initial state with comparable populations in all of the  $F = 3$  Zeeman states. To prepare this state, we optically pump the atom to  $F = 3$  by alternating 7 pulses of resonant  $F = 4 \rightarrow F = 4'$  lattice light with 7 pulses of resonant  $F = 4 \rightarrow F = 4'$  side light, where each pulse is 300 ns long. The beams that deliver the lattice and side light are shown in Figure 4.1.

---

<sup>4</sup>Subsequent measurements (Section 5.2.2) have shown that decoherence times are longer over a certain frequency range on the red side of each transition. Pulses of  $25 \mu\text{s}$  are in fact not quite long enough for decoherence at these special detunings, but the Lorentzian assumption still holds in the context of a broad scan.

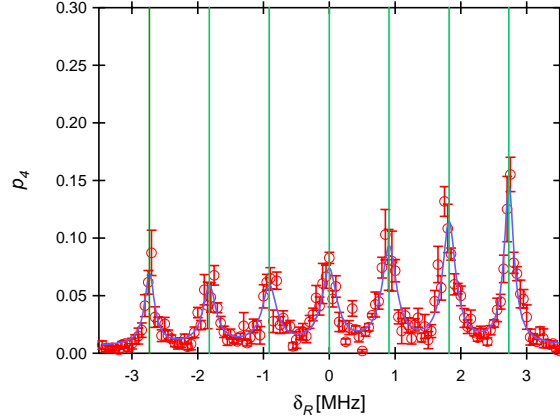


Figure 4.4: Raman spectrum for a random initial state. Shown is the transfer probability  $p_4$  vs. Raman detuning  $\delta_R$ : the points are the experimental data, the curve is a fit of  $p_4(\delta_R)$ , as given by equation (4.5), and the vertical green lines indicate the predicted frequencies  $\delta(|3, m\rangle \leftrightarrow |4, m\rangle)$  for individual Zeeman transitions.

To determine the population  $p_{3,m}$  in the Zeeman state  $|3, m\rangle$ , we fit a sum of Lorentzians, one for each Zeeman transition, to the experimental data:

$$p_4(\delta_R) = p_b + (1/2) \sum_m (1 + (\delta_R - \omega_B m)^2 / (1 - m^2/16) \Omega_0^2)^{-1} p_{3,m}, \quad (4.5)$$

where  $p_b$  is a constant background. We fit the Zeeman state populations, the Rabi frequency  $\Omega_0$ , and the frequency  $\omega_B$  that characterizes the strength of the axial bias field, and perform an independent measurement to determine the background probability  $p_b = 0.006$ . The fitted value of  $\Omega_0$  agrees to within 14% with the value we would expect based on the measured optical powers in the FORT and Raman beams, and the fitted value of  $\omega_B$  agrees to within 5% with the value we would expect based on the known axial coil current and geometry. As a consistency check, we sum the fitted populations and obtain the result  $1.10 \pm 0.03$ , in reasonable agreement with the expected value of 1.

#### 4.1.5 Optical pumping scheme

We can prepare the atom in a specific Zeeman state by using a Raman beam whose spectrum is tailored to drive incoherently all but one of the Zeeman transitions. As

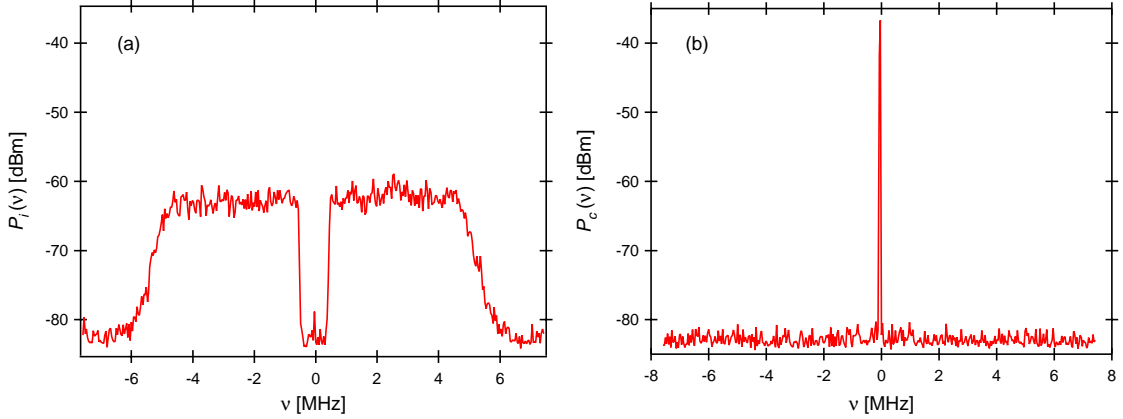


Figure 4.5: (a) Power spectrum of noise used for pumping into  $|3,0\rangle$ . (b) Power spectrum of coherent signal used for driving coherent Raman transitions with  $\Omega_0 = (2\pi)(120 \text{ kHz})$ . Both curves are obtained by combining the FORT and Raman beams on a photodetector and measuring the spectrum of the photocurrent, mixed down from  $\Delta_{HF} = 9.2 \text{ GHz}$ ; shown is the RF power in a 3 kHz bandwidth vs. detuning from  $\Delta_{HF}$ .

an example, Figure 4.5a shows the power spectrum of the noise used for pumping into  $|3,0\rangle$ . This graph was obtained by measuring the power spectrum of a beat note formed between the FORT and Raman beams by mixing them on a photodetector with a non-polarizing beam splitter. For comparison, Figure 4.5b shows the power spectrum for a monochromatic Raman beam tuned to Raman resonance, as would be used for driving coherent Raman transitions.

Comparing the noise spectrum shown in Figure 4.5a to the Raman spectrum shown in Figure 4.4, we see that the noise drives incoherent Raman transitions from  $|3,m\rangle \leftrightarrow |4,m\rangle$  for  $m \neq 0$ , but because of the notch around zero detuning, the  $|3,0\rangle \leftrightarrow |4,0\rangle$  transition is not driven. We optically pump the atom into  $|3,0\rangle$  by first driving incoherent Raman transitions for  $10 \mu\text{s}$ , then pumping the atom to  $F = 3$  using the method discussed in Section 4.1.4, and iterating this sequence 40 times. It is straightforward to modify this procedure so as to pump into the  $|3,m\rangle$  Zeeman state for any  $m$ ; we simply shift the notch in the noise so that it overlaps with the  $|3,m\rangle \leftrightarrow |4,m\rangle$  transition.

To characterize the optical pumping, we first pump the atom into a specific Zeeman state and then measure the Raman spectrum as described in the preceding section.

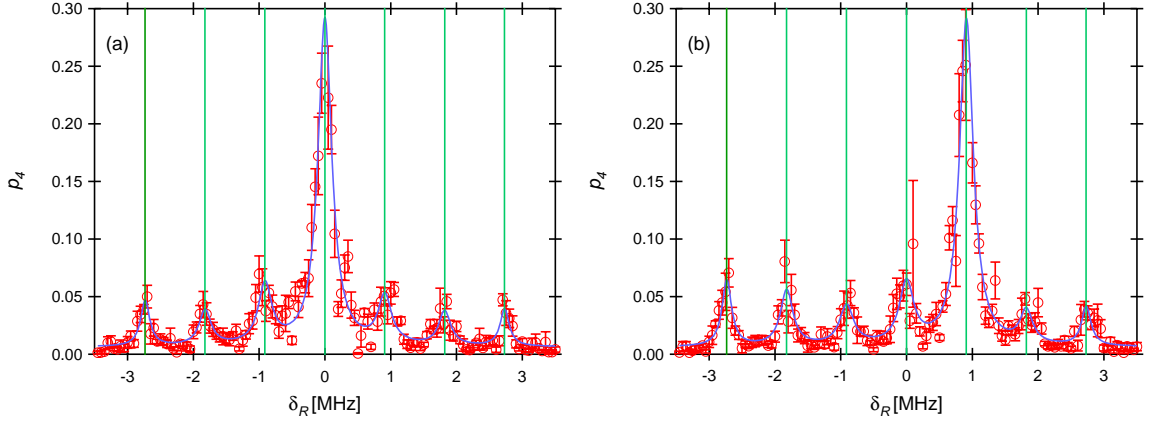


Figure 4.6: (a) Raman spectrum for optical pumping into  $|3, 0\rangle$ . (b) Raman spectrum for optical pumping into  $|3, 1\rangle$ . Raman spectrum for a random initial state. Shown is the transfer probability  $p_4$  vs. Raman detuning  $\delta_R$ : the points are the experimental data, the curve is a fit of  $p_4(\delta_R)$ , as given by equation (4.5), and the vertical green lines indicate the predicted frequencies  $\delta(|3, m\rangle \leftrightarrow |4, m\rangle)$  for individual Zeeman transitions.

Figure 4.6 shows Raman spectra measured after pumping into (a)  $|3, 0\rangle$  and (b)  $|3, 1\rangle$ . We find that the fraction of the atomic population in the desired state is  $0.57 \pm 0.02$  for pumping into  $|3, 0\rangle$  and  $0.57 \pm 0.02$  for pumping into  $|3, 1\rangle$ , where the remaining population is roughly equally distributed among the other Zeeman states (these numbers are obtained by fitting equation (4.5) to the data, as described in Section 4.1.4). Summing the fitted populations in all the Zeeman states, we obtain the value  $1.02 \pm 0.04$  for (a) and  $1.08 \pm 0.04$  for (b), in reasonable agreement with the expected value of 1.

To generate the Raman beam used in Figure 4.5a, we start with an RF noise source, which produces broadband noise that is spectrally flat from DC to  $\sim 10$  MHz. The noise is passed through a high-pass filter at 500 kHz and a low-pass filter at 5 MHz, where both filters roll off at 60 dB per octave. The filtered noise is then mixed against an 85 MHz local oscillator, and the resulting RF signal is used to drive an acousto-optical modulator (AOM) that modulates a coherent beam from the injection-locked Raman laser. The first-order diffracted beam from the AOM forms a Raman beam with the desired optical spectrum. Note that previous work has demonstrated the use of both synthesized incoherent laser fields [98, 99], such as that used here, as well as

the noise intrinsic to free-running diode lasers [100, 101] to resonantly probe atomic spectra.

Although the scheme presented here relies on incoherent Raman transitions, it is also possible to perform optical pumping with coherent Raman transitions. The basic principle is the same: we simultaneously drive all but one of the Zeeman transitions, only instead of using a spectrally broad Raman beam, we use six monochromatic Raman beams, where each beam is tuned so as to resonantly drive a different transition. We have implemented such a scheme, and found that it gives comparable results to the incoherent scheme described above, but there are two advantages to the incoherent scheme. First, it is simpler to generate a Raman beam with the necessary spectral properties for the incoherent scheme. Second, when coherent Raman transitions are used, the six frequency components for the Raman beam must be tuned to resonance with their respective transitions, and hence are sensitive to the value of the axial magnetic field. When incoherent Raman transitions are used, however, the same Raman beam can be used for a broad range of axial field values.

#### 4.1.6 Conclusion

We have proposed a new scheme for optically pumping atoms into a specific Zeeman state and have experimentally implemented the scheme with cesium atoms in a cavity QED setting. An important advantage over existing schemes is that atoms can be prepared in any of the Zeeman states in the lower hyperfine ground state manifold.

We have measured the effectiveness of the optical pumping, and have shown that a fraction  $\sim 0.57$  of the atomic population can be prepared in the desired Zeeman state. Some possible factors that could be limiting the effectiveness of the optical pumping include fluctuating magnetic fields transverse to the cavity axis, misalignment of the cavity axis with the axial bias field, and slow leaking out of the dark state due to scattering from background light. We are currently investigating these factors.

The scheme presented here operates on a fundamentally different principle from existing optical pumping schemes, in that it relies on incoherent Raman transitions

to create an atomic dark state. Raman transitions have many different applications in atomic physics, so there are often independent reasons for incorporating a system for driving Raman transitions into an atomic physics laboratory; our scheme shows that such a system can also be applied to the problem of atomic state preparation. The scheme should serve as a useful tool for experiments in atomic physics, both in a cavity QED setting and beyond.

#### 4.1.7 Transition rate for incoherent Raman transitions

As described in Section 4.1.3, we drive incoherent Raman transitions between pairs of Zeeman states  $|3, m\rangle \leftrightarrow |4, m\rangle$  by using a monochromatic FORT beam and a spectrally broad Raman beam. For incoherent Raman transitions the atomic population decays at a constant rate from  $|3, m\rangle \rightarrow |4, m\rangle$  and from  $|4, m\rangle \rightarrow |3, m\rangle$ , and in this section we calculate these decay rates.

We will consider a single Zeeman transition  $|3, m\rangle \leftrightarrow |4, m\rangle$ , so we can treat the system as an effective two-level atom with ground state  $g \equiv |3, m\rangle$  and excited state  $e \equiv |4, m\rangle$ , where the energy splitting between  $g$  and  $e$  is  $\omega_A \equiv \Delta_{HF} + \omega_B m$ . The FORT-Raman pair drives this effective two-level atom with broadband noise, which we can approximate as a comb of classical fields with optical frequencies  $\omega_k$  and Rabi frequencies  $\Omega_k$ . Let us assume that we start in the ground state  $g$ . If we only consider the coupling of the atom to field  $k$ , then the equation of motion for the excited state amplitude  $c_e$  is

$$i\dot{c}_e = \frac{\Omega_k}{2} e^{-i\delta_k t} c_g, \quad (4.6)$$

where  $\delta_k \equiv \omega_k - \omega_A$  is the detuning of the field from the atom. At small times the population is almost entirely in the ground state, so we can make the approximation  $c_g = 1$  and integrate equation (4.6) to obtain

$$c_e(t) = \frac{\Omega_k}{2\delta_k} (e^{-i\delta_k t} - 1). \quad (4.7)$$

Thus, the transition rate from  $g$  to  $e$  for a single frequency  $\omega_k$  is

$$\gamma_k = \frac{|c_e(t)|^2}{t} = \frac{\pi}{4} t \Omega_k^2 D(\delta_k t/2), \quad (4.8)$$

where

$$D(x) \equiv \frac{\sin^2 x}{\pi x^2}. \quad (4.9)$$

The total decay rate is obtained by summing the decay rates for all the fields in the comb:

$$\gamma = \sum_k \gamma_k = \frac{\pi}{4} t \sum_k \Omega_k^2 D(\delta_k t/2). \quad (4.10)$$

To evaluate this expression we need to know the distribution of Rabi frequencies  $\Omega_k$ . This information can be obtained by forming a beat note between the FORT and Raman beams on a photodetector, and measuring the power spectrum  $S(\omega)$  of the photocurrent using a spectrum analyzer. Let us first consider this measurement for a monochromatic Raman beam, and then generalize to a spectrally broad Raman beam. If both the FORT and Raman beams are monochromatic, with optical frequencies  $\omega_F$  and  $\omega_R$ , then the resulting photocurrent  $i(t)$  is given by

$$i(t) = i_F + i_R + 2\eta \cos((\omega_F - \omega_R)t) \sqrt{i_F i_R}, \quad (4.11)$$

where  $i_F$  and  $i_R$  are the cycle-averaged photocurrents for the FORT and Raman beams taken individually and  $\eta$  is the heterodyne efficiency. Thus, the power spectrum of the photocurrent has a spike at the difference frequency  $\Delta \equiv \omega_F - \omega_R$ :

$$S_c(\omega) = P_c \delta(\omega - \Delta), \quad (4.12)$$

where the integrated power  $P_c$  of the spike is proportional to  $i_F i_R$ . If the difference frequency  $\Delta$  is tuned to Raman resonance ( $\Delta = \omega_A$ ), then the FORT-Raman pair

drives coherent Raman transitions with a Rabi frequency  $\Omega_c$  that is proportional to  $\sqrt{i_F i_R}$ , so

$$\Omega_c^2 = \alpha P_c, \quad (4.13)$$

where  $\alpha$  is a constant that depends on various calibration factors.

Now consider the case of a spectrally broad Raman beam, which results in a photocurrent with power spectrum  $S_i(\omega)$ . The effective Rabi frequency  $\Omega_k$  corresponding to comb line  $k$  is given by

$$\Omega_k^2 = \alpha S_i(\omega_k) \delta\omega, \quad (4.14)$$

where  $\delta\omega$  is the frequency spacing between adjacent comb lines. Substituting this result into equation (4.10), and replacing the sum with an integral, we obtain

$$\gamma = \frac{\pi}{4} \alpha t \int S_i(\omega) D((\omega - \omega_A)t/2) d\omega. \quad (4.15)$$

If the power spectrum near  $\omega_A$  is flat over a bandwidth  $\sim 1/t$ , then we can approximate  $D$  as a delta function and perform the integral:

$$\gamma = \frac{\pi}{2} \alpha S_i(\omega_A). \quad (4.16)$$

It is convenient to use equation (4.13) to eliminate the calibration factor  $\alpha$ :

$$\gamma = \frac{\pi}{2} \frac{S_i(\omega_A)}{P_c} \Omega_c^2. \quad (4.17)$$

The spectrum analyzer trace given in Figure 4.5a displays the power spectrum in terms of the power  $P_i(\nu) \simeq 2\pi B S_i(\omega)$  in a bandwidth  $B = 3$  kHz, so we can also write this as

$$\gamma = \frac{1}{4} \frac{P_i(\omega_A/2\pi)}{P_c} \frac{\Omega_c^2}{B} = \frac{1}{4} (1 - m^2/16) \frac{\Omega_0^2}{B} \frac{P_i((\Delta_{HF} + \omega_B m)/2\pi)}{P_c}, \quad (4.18)$$

where we have substituted  $\Omega_c = (1 - m^2/16)^{1/2} \Omega_0$  and  $\omega_A = \Delta_{HF} + \omega_B m$ .

We can calculate the time evolution of the atomic populations using rate equations. It is straightforward to show that the decay rate  $e \rightarrow g$  is also given by  $\gamma$ , and from the rate equations one can show that the excited state population is

$$p_e(t) = \frac{1}{2}(1 - \exp(-2\gamma t)). \quad (4.19)$$

We can calculate the decay rates for the noise spectrum shown in Figure 4.5. For this noise spectrum the power  $P_i(\nu)$  has roughly the same value  $\bar{P}_i$  at the frequencies of all the  $m \neq 0$  Zeeman transitions, so we can write the decay rates for these transitions as

$$\gamma(|3, m\rangle \rightarrow |4, m\rangle) = \gamma(|4, m\rangle \rightarrow |3, m\rangle) = (1 - m^2/16) \Gamma, \quad (4.20)$$

where

$$\Gamma \equiv (1/4)(\Omega_0^2/B)(\bar{P}_i/P_c). \quad (4.21)$$

From the power spectrum for the noise shown in Figure 4.5a we have that  $\bar{P}_i = -63$  dBm, and from the power spectrum for the coherent signal shown in Figure 4.5b we have that  $P_c = -36$  dBm, where the corresponding Rabi frequency is  $\Omega_0 = (2\pi)(120 \text{ kHz})$ . Substituting these values into equation (4.21), we obtain  $\Gamma = 0.084 \mu\text{s}^{-1}$ .

## 4.2 Optimizing optical pumping

The discussion in the previous section centers on an example in which a magnetic field is applied along the cavity axis, so that only  $\Delta m = 0$  Raman transitions are permitted. It is important to stress, however, that Raman-based optical pumping also works for an arbitrary applied field, in which  $\Delta m = \pm 1$  transitions are also possible. The point is that given an applied field of any direction and magnitude, it will have an associated Raman spectrum which reflects transitions between different pairs of

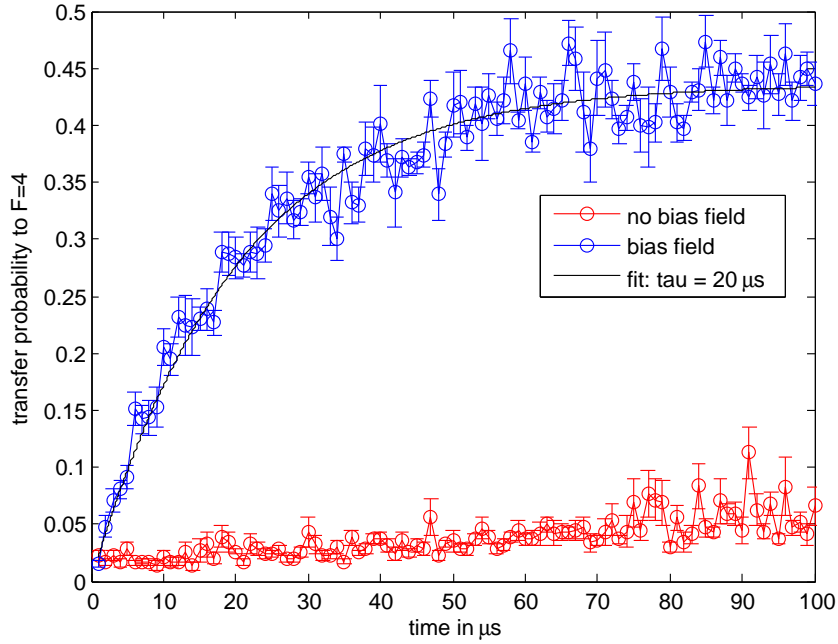


Figure 4.7: Rate of population transfer for incoherent Raman transitions: atoms are prepared in  $F = 3$  and then driven with the notched incoherent Raman spectrum of Figure 4.5(a), in the presence (blue) or absence (red) of a magnetic bias field. The probability to transfer an atom to  $F = 4$  is shown as a function of pumping time.

Zeeman levels. Based on this Raman spectrum, one can tailor a noise spectrum such as 4.5(a) which will address transitions between all but one Zeeman level.

In implementing our optical pumping scheme, we took several steps to optimize the relevant parameters. First, we characterized the preparation of atoms in  $F = 3$  via lattice light and linearly polarized side light; we found that by using short (300 ns) interleaved pulses and resonant light, we could transfer 99.9% of the population to the  $F = 3$  manifold in  $10 \mu\text{s}$ .<sup>5</sup> We next measured the rate at which the incoherent Raman spectrum transferred population from  $F = 3$  to  $F = 4$ . This is shown in Figure 4.7, where atoms are prepared in the  $F = 3$  manifold and then subjected to incoherent Raman pulses of varying duration, either in the presence or absence of a

<sup>5</sup>Switching between two fields with different polarizations is necessary to avoid creating a permanent dark state in the  $F = 4$  manifold. An alternate but slightly less efficient scheme is to drive both lasers continuously but with a small relative detuning; the detuning then sets a precession rate for the dark state. In the case of an applied magnetic field, only one  $F = 4 \rightarrow F' = 4$  laser is necessary, since now the atom's dark state changes as it travels through the field.

bias field. With the magnetic fields nulled, we expect that the the notched Raman spectrum will be unable to drive any resonant transitions between Zeeman states, and the slow leakage we observe into  $F = 4$  is probably due to off-resonant driving from the edges of the notch. In the presence of a bias field, the Raman pulses should be able to address atoms in every Zeeman level but  $|3, 0\rangle$  and to transfer population until an equilibrium is reached. We see that this population transfer takes place with time constant  $\tau = 20 \mu\text{s}$  and that it asymptotes to a state in which approximately 45% of the population is in  $F = 4$ ; presumably, another 45% resides in  $|3, m_F \neq 0\rangle$  and the final 10% remains in  $|3, 0\rangle$ . The measured value of  $\tau$  is in reasonable agreement with the calculated value  $\Gamma = 0.084 \mu\text{s}^{-1}$  in Section 4.1.7, which should be weighted by the initial distribution of atoms among Zeeman manifolds as in equation (4.20).

The time constants for these two processes — repumping to  $F = 3$  and incoherent Raman transfer to  $|4, m_F \neq 0\rangle$  — allowed us to design a series of pulses in which population is shuttled back and forth between the two hyperfine manifolds while gradually accumulating in  $|3, 0\rangle$ . In order to optimize both the pulse durations and the number of iterations, we measured the final population transferred to  $|3, 0\rangle$  as a function of these parameters; we settled on 10  $\mu\text{s}$  of incoherent Raman light followed by 4.2  $\mu\text{s}$  of  $F = 4 \rightarrow F' = 4$  repump fields (7 cycles of paired 300 ns pulses), repeated 40 times. Thus, the time required for optical pumping of each atom is roughly 600  $\mu\text{s}$ .

We also investigated the fraction of population that we could prepare in  $|3, 0\rangle$  as a function of the applied axial magnetic field. Recall that our incoherent Raman spectrum has a low-frequency cutoff at  $(2\pi)(500 \text{ kHz})$  and a high-frequency cutoff at  $(2\pi)(5 \text{ MHz})$ . In the limit of very small axial fields, all of the  $\Delta m = 0$  transitions are contained within the low-frequency notch; we expect that the Raman spectrum will be unable to transfer population to  $F = 4$ , and optical pumping will be ineffective. However, also for small applied fields, the  $|3, 0\rangle \rightarrow |4, 0\rangle$  Raman pulse that we use to measure population should in fact address all Zeeman states. Thus, as we see in Figure 4.8, the measured population transfer is very high at the smallest field values. As the  $\Delta m = 0$  transitions with  $m \neq 0$  are pushed out of resonance with the

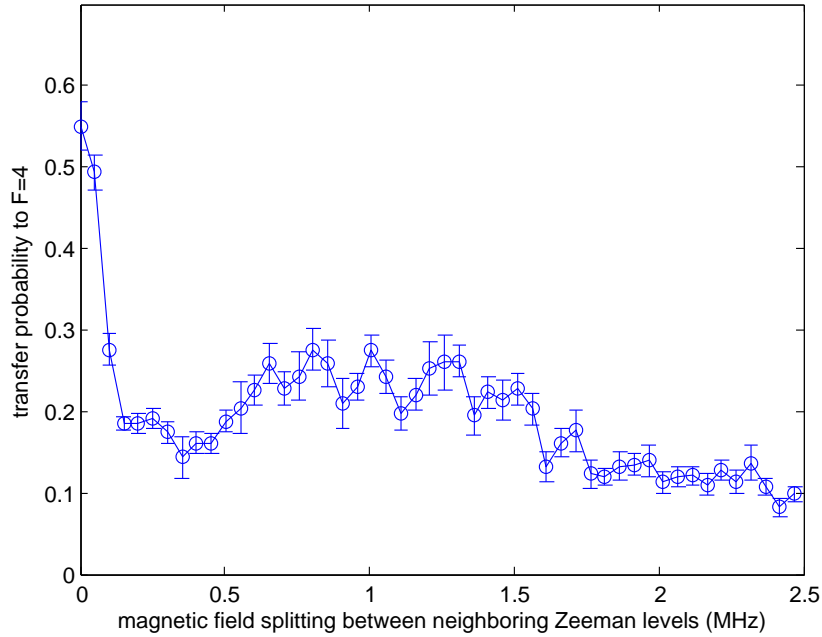


Figure 4.8: We measure the success of our Raman optical pumping protocol as a function of axial magnetic bias field. After optical pumping, we apply a Raman pulse to transfer population from  $|3, 0\rangle$  to  $|4, 0\rangle$ , followed by state detection. For small fields, the pulse addresses all Zeeman levels, while at larger values, the number of Zeeman transitions inside the Raman envelope is field-dependent.

$|3, 0\rangle \rightarrow |4, 0\rangle$  detection pulse, this value declines steeply. It then rises again for field splittings greater than  $(2\pi)(0.5 \text{ MHz})$ , as one by one, Raman transition frequencies are pushed outside the notch and can now be driven by the incoherent Raman fields. Finally, at roughly  $(2\pi)(\frac{1}{3} \times 5 \text{ MHz})$ , the  $|3, \pm 3\rangle \rightarrow |4, \pm 3\rangle$  transitions are pushed past the high-frequency cutoff and again out of range of the incoherent Raman; here the transfer probability begins again to decline. Based on this measurement, we set our axial field to generate a splitting of  $(2\pi)(910 \text{ kHz})$  between neighboring Zeeman levels. However, it is clear that optical pumping should be effective over  $\sim 1 \text{ MHz}$  of field values, and we could of course use different filters in order to access a wider range.

Despite our efforts at optimization, we are able to transfer at best 60% of atoms into a target Zeeman state. We remain unsure as to what limits our pumping effi-

ciency, although we have narrowed the list of possible suspects. We have ruled out scattered light from stray fields, as we have seen that atoms pumped into  $F = 3$  only leak into  $F = 4$  very slowly (Figure 4.7). The small peak at 85 MHz in the power spectrum shown in Figure 4.5(a), due to carrier frequency leakage through our RF mixer, is also not a cause for concern; we have confirmed that the optical pumping efficiency does not change when we shift the center frequency of the spectrum out of resonance with the  $|3, 0\rangle \rightarrow |4, 0\rangle$  transition. We also have replaced the 500 kHz low-frequency notch with one at 100 kHz with no observed change in pumping efficiency, suggesting that off-resonant excitation of  $|3, 0\rangle \rightarrow |4, 0\rangle$  due to the finite notch width is not the problem. Remaining candidates include fluctuating magnetic fields and the finite suppression ( $\sim 20$  dB) of Raman power which the notch provides.

A final unresolved question concerns the timing of our optical pumping scheme. We would expect that atoms would be pumped to the dark state  $|3, 0\rangle$  by applying the incoherent Raman pair and the  $F = 4 \rightarrow F' = 4$  repumping light simultaneously. However, in practice we have found that this is much less successful than the pulsed scheme and that any overlap between the Raman and repump pulses degrades the scheme's effectiveness.

## 4.3 Trapping and detecting multiple atoms

### 4.3.1 Cavity loading

Through mid-2007, we relied on optical lattice Sisyphus cooling to load atoms into the FORT after their release above the cavity [13]. The details of this method are as follows: 30 ms after the end of polarization-gradient cooling in the lower MOT, when we expect the atoms to be falling through the cavity mode, we turn on  $F = 3 \rightarrow F = 3'$  and  $F = 4 \rightarrow F = 4'$  lattice beams for 5 ms, where both beams are blue-detuned by 10 MHz. The best observed loading probabilities for  $\geq 1$  atoms are  $\sim 60\%$  with this technique, in which case (assuming Poissonian loading statistics)  $\sim 30\%$  of all loading attempts would consist of single atoms. We hypothesize that one of the two

lattice beams provides Sisyphus cooling [67], while the other acts as a repump (and thus in principle does not need to be in the standing-wave lattice configuration). In experiments where the cavity is tuned to the  $F = 4 \rightarrow F = 4'$  transition, we have found that we cannot load efficiently using  $F = 4 \rightarrow F = 4'$  lattice light; we believe that this is due to resonant scattering into the cavity mode. Instead, in this case we employ the  $F = 3 \rightarrow F = 3'$  lattice beam in conjunction with a resonant probe beam along the cavity axis, which presumably repumps the atoms with less scatter-induced heating.

We have recently found that by instead using the FORT-Raman pair during the 5 ms loading window in conjunction with the  $F = 4 \rightarrow F = 4'$  lattice beam, over 99% of all MOT drops result in cavity loading. (Note that as the intracavity FORT is always present, the beams we turn on for loading are the Raman beam and the  $F = 4 \rightarrow F = 4'$  lattice.) In contrast with the previous method, which required a dense, bright lower MOT, here we observe excellent loading even when the lower MOT quality is visibly poor. Furthermore, the measurements described below confirm that we are loading multiple atoms almost every time.

We hypothesize that by replacing the  $F = 3 \rightarrow F = 3'$  beam with Raman transitions, we are still able to recycle the atom to  $F = 4$  while avoiding the spontaneous emission inherent to a  $F = 3 \rightarrow F = 3'$  repump; the  $F = 4 \rightarrow F = 4'$  lattice beam then provides the necessary Sisyphus cooling. Repumping via Raman transitions thus results in more efficient atom cooling, because spontaneous emission was previously heating the atom throughout the cooling process. Loading efficiency is found to increase as a function of Raman beam intensity, presumably because it allows faster recycling, and we currently use a Rabi frequency of 2.2 MHz for atom loading. We have explored loading efficiency of the Raman scheme as a function of various parameters, as discussed in Section 4.3.4.

Despite the significant improvement in loading efficiency, we do not observe direct loading from the upper MOT (with the timing sequence adjusted appropriately, so that the cooling beams address the atoms while they are within the cavity). In the process of setting up the lab 11 experiment, Joe Buck and Jason McKeever observed

transits from atoms dropped from both the upper and lower MOTs, with narrower transits corresponding to the faster velocities of the upper MOT atoms [102], but we no longer see upper MOT transits. Presumably this effect is highly sensitive to the position of the upper MOT with respect to the gap between the cavity mirrors, as well as to the forces which the falling atoms experience as the magnetic fields are ramped off.

### 4.3.2 Raman-based determination of atom number

The “Raman repump” technique outlined above can be used not only to load atoms into the cavity but also to determine the number of atoms present in real time. In order to explain this measurement, we first consider the “by the numbers” effect originally demonstrated in Ref. [18]. In that experiment, the cavity was tuned to the  $F = 4 \rightarrow F = 4'$  transition and probed continuously with a resonant on-axis beam in tandem with a  $F = 3 \rightarrow F = 3'$  lattice beam. While the vacuum-Rabi splitting tells us that the presence of a single two-level atom in our strongly coupled cavity will completely suppress the transmission of a resonant probe beam, the two-level model is insufficient for a non-cycling transition such as  $F = 4 \rightarrow F = 4'$ . An atom may be in the  $F = 4$  manifold, in which case it participates in the cavity-QED interaction, or it may be in  $F = 3$ , in which case the probe laser sees an empty cavity. With the introduction of a lattice beam as a repump, the atom moves back and forth rapidly between these two possibilities, and over timescales  $\gtrsim 1$  ms, the cavity transmission represents a time-average of high ( $F = 3$ ) and low ( $F = 4$ ) values. When  $N > 1$  atoms are present, there is a greater probability that at least one atom will be in  $F = 4$  and that transmission will be suppressed. Thus, as atoms leave the cavity one by one, we observe a climbing “stair-step” transmission with distinct plateaus corresponding to atom number.

In addition to the initial  $F = 4 \rightarrow F = 4'$  measurements [18], we have subsequently observed this “by the numbers” effect with the cavity and probe tuned to the  $F = 4 \rightarrow F = 3'$  transition (though with worse signal-to-noise and shorter atom lifetimes

in the cavity). Jason suggested in his thesis [39] that this technique could be used to prepare one atom deterministically in the cavity, either by actively discarding cases where  $N > 1$  or by heating out the additional atoms. Unfortunately, most of our experiments to date have taken place with the cavity tuned to the  $F = 4 \rightarrow F' = 5$  resonance in order to exploit the physics of the cycling transition, whereas “by the numbers” relies on a non-cycling transition for atom detection.

Raman transitions between the cesium ground states allow us to have our cake and eat it too, or in this case, to implement atom number determination on a cycling transition. The key concept here is that while the trapped atoms would ordinarily remain in the  $F = 4$  manifold, we can use the FORT-Raman combination to cycle each atom between  $F = 4$  and  $F = 3$  at the Rabi frequency of the Raman pair. As in the original experiment, the probability to have at least one atom in  $F = 4$  increases with atom number. The result is the same “telegraph signal” of high (all atoms in  $F = 3$ ) and low (one or more atoms in  $F = 4$ ) values, which we observe as an averaged stair-step pattern. One might imagine that the atom-number plateaus would be noisy due to this averaging; in Ref. [18], their smoothness is due to the fact that the timescale of decay to  $F = 3$  and recycling to  $F = 4$  ( $\sim \gamma^{-1}$ , ten of nanoseconds), is much shorter than the lifetime of atoms in the cavity (hundreds of milliseconds), and that the data are filtered by the heterodyne detection bandwidth of 1 kHz. For Raman-based atom number determination, cycling between atomic levels also needs to be fast with respect to the number determination time window. In practice, as for atom loading, we operate with a Rabi frequency of 2.2 MHz. As we have replaced heterodyne detection with photon counting, we bin the photon counts on a time frame that is short compared with atom lifetimes in the cavity.

Figure 4.9 shows typical traces from a data set of 1,200 MOT drops in which the FORT-Raman pair and a blue-detuned  $F = 4 \rightarrow F = 4'$  lattice were used to load atoms into a cavity tuned to the  $F = 4 \rightarrow F' = 5$  transition, followed by 280 ms of the Raman pair in conjunction with a probe resonant with the cavity. Photon counts are binned in 1 ms intervals for the data presented. Here we observe the expected stair-step pattern and well-defined plateaus for single atoms, suggesting that  $t_{detect} = 1$  ms

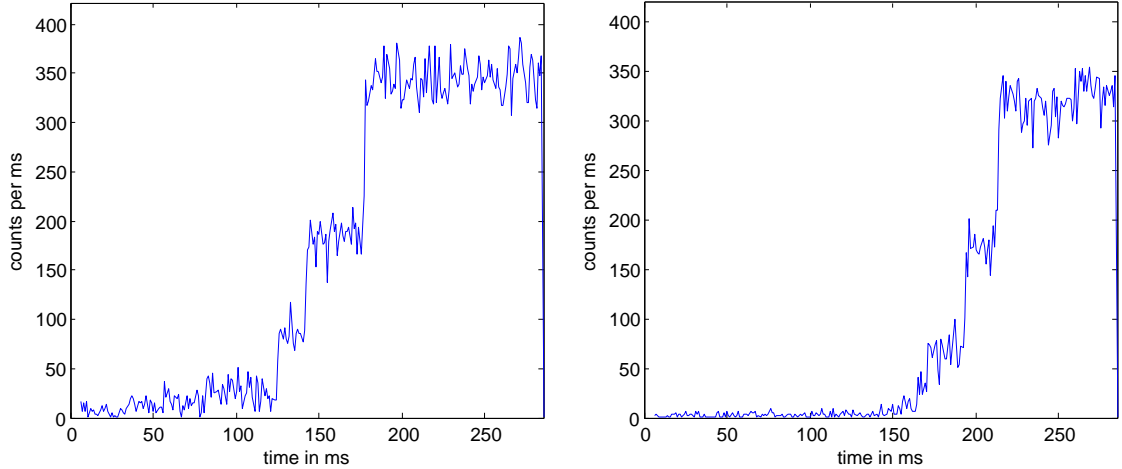


Figure 4.9: Two sample traces from a data set of 1,200 MOT drops: the FORT-Raman pair and  $F = 4 \rightarrow F = 4'$  lattice are used to load multiple atoms into a cavity on the  $F = 4 \rightarrow F = 5'$  transition, followed by 280 ms of Raman and a resonant probe beam on the cavity axis. Photon counts are binned in 1 ms intervals.

should be sufficient in order to determine  $N \leq 1$ .

Figure 4.10 shows a histogram of counts per 1 ms bin for the entire data set. Because the histogram is dominated by multi-atom (highly suppressed) events, the second plot shows a closer view of the y-axis near the origin in order to resolve zero-, one-, and two-atom peaks clearly. We observe that the one-atom peak is easy to distinguish from the zero-atom and two-atom cases, and that it is also plausible that we could separate out two-atom events. More quantitatively, we can fit the data to a sum of Gaussians corresponding to photon count distributions for each atom number, as shown in Figure 4.11; the center of each Gaussian is then the mean number of counts for a given atom number plateau. (We initially attempted to fit the data as a sum of Poissonians, but it was clear that the distribution widths were greater than  $\sqrt{N}$  fluctuations alone could explain. Other contributions to the spread may include noise on the cavity lock and variation in the probe intensity over time.)

Note that the mechanism which determines the level spacing between  $N$ -atom plateaus is different in the lattice (non-cycling) and Raman (cycling) cases. For the lattice, the intensity of an  $N$ -atom plateau is given by  $\frac{I_0}{\sum_{k=0}^N (k!)^2 y^k}$ , where the sum is from  $k = 0$  to  $N$  and  $I_0$  is the intensity of the zero-atom plateau. Here  $y$  is the ratio  $\frac{\gamma_{3 \rightarrow 4}}{\gamma_{4 \rightarrow 3}}$ ,

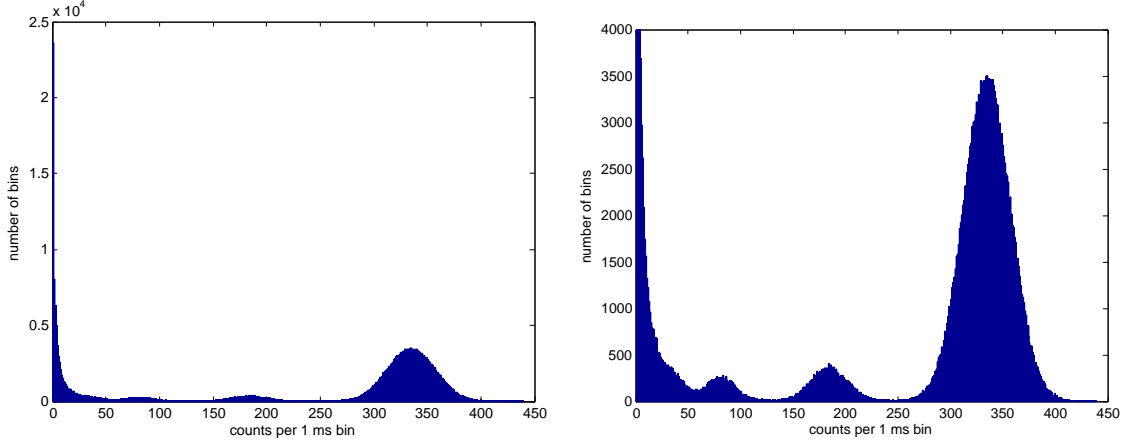


Figure 4.10: Histogram of photon counts per 1 ms time bin for the data set of Figure 4.9, with 280 ms of continuous Raman and probe beams. The data are shown twice, with a smaller range in the second plot.

where  $\gamma_{n \rightarrow m}$  is the rate at which one atom is transferred from level  $n$  to level  $m$ . In Ref. [18], these two rates could in principle be controlled independently by adjusting the intensities of the lattice and probe beams. In the current experiment, however, the probability that we will measure an atom driven by Raman transitions to be in  $F = 3$  is simply  $\frac{1}{2}$ , and the probability to find  $N$  atoms in  $F = 3$  is  $(\frac{1}{2})^N$ . Thus we expect  $I_1 = \frac{I_0}{2}$ ,  $I_2 = \frac{I_0}{4}$  and in general,

$$I_N = \frac{I_0}{2^N}. \quad (4.22)$$

The fits in Figure 4.11 are roughly consistent with this expectation, although we have observed day-to-day variation of  $\sim 20\%$  in the peak ratios. For the purposes of atom discrimination, we are only concerned with setting a strict enough lower bound so that the case  $N \geq 2$  is always excluded.

In Figure 4.12, the histogram data of Figure 4.10 are separated out by time bin. This plot displays the same basic features as Figure 3 of Ref. [18], namely (a) clustering of data in well-defined atom-number plateaus, and (b) time-dependent evolution of the plateaus from  $N \geq 3$  to  $N = 0$  as atoms leave the trap. In Ref. [18], we observe a clear departure of atoms from one plateau to the next, and by the end of the probing interval, the trap population resides entirely in the  $N = 0$  plateau.

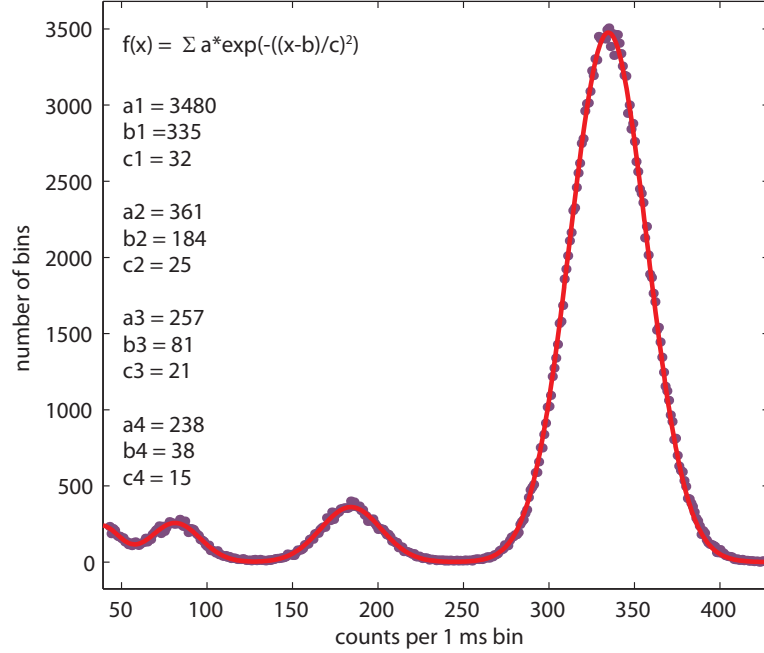


Figure 4.11: Fit of the data in Figure 4.10 to a sum of four Gaussians. The data have been truncated for small count rates in order to consider atom number  $N \leq 3$ .

Here, in contrast, while some traces show the expected progression through  $N = 1$  to  $N = 0$ , there are many cases for which  $N \geq 3$  even at the end of the probing interval. The distribution of counts around these high-atom-number events narrows as a function of time, which might suggest that poorly coupled atoms leave the trap quickly while well-coupled ones remain. Furthermore, the data at late time intervals ( $t > 150$  ms) indicate a direct progression from the multi-atom case to  $N = 0$ ; that is, atoms may sometimes leave in rapid succession due to a “catastrophic event” rather than independently.

We can further explore the time dependence of atom populations by assigning approximate atom-number boundaries to the histogram data. We have seen that the  $N = 0$  plateau (Figure 4.11) is centered at 335 counts per ms bin and that we expect this plateau value to scale as  $2^{-N}$ . We define four regions as follows:

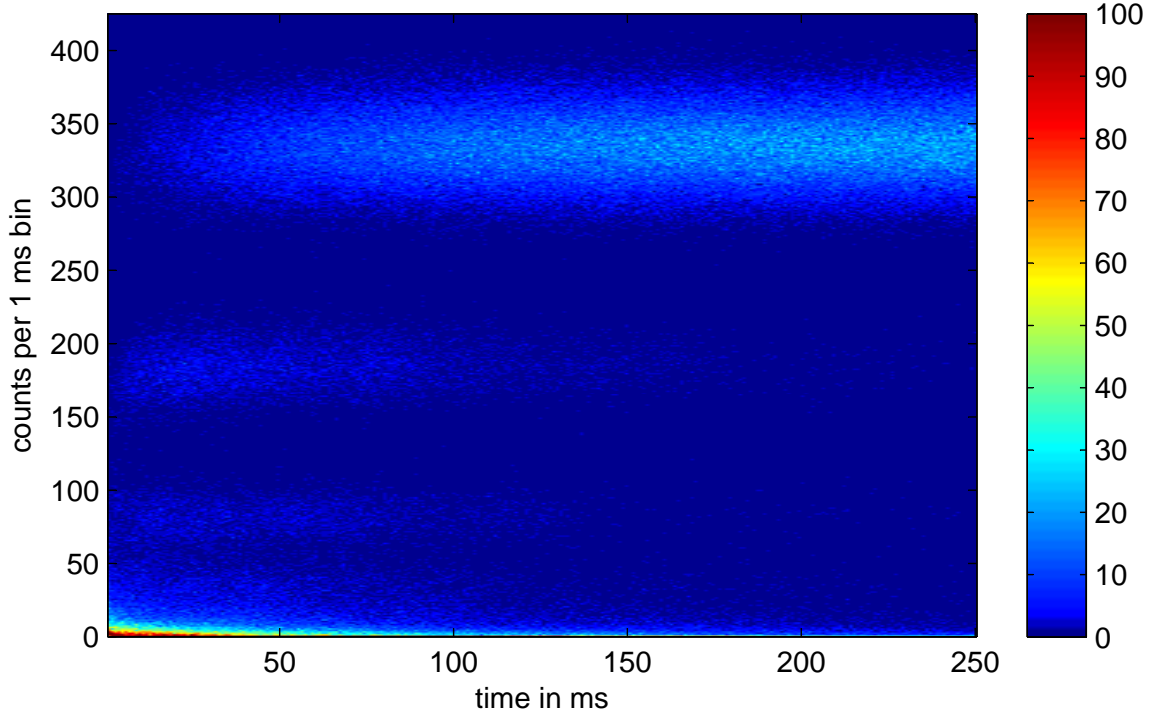


Figure 4.12: Photon count rate histograms (y axis) as a function of time bin (x axis) for the data set of Figure 4.9

Atom number	Min. counts per bin	Max. counts per bin
0	$\frac{3}{4} * 335$	
1	$\frac{3}{8} * 335$	$\frac{3}{4} * 335$
2	$\frac{3}{16} * 335$	$\frac{3}{8} * 335$
$\geq 3$		$\frac{3}{16} * 335$

By summing the number of counts within each region for every time bin, we can then plot atom populations as a function of time, as shown in Figure 4.13. Again, we find a point of comparison in the equivalent plot (Figure 4) of Ref. [18]. For that data set, the  $N \geq 3$  population exhibited a steady decay from its initial value at  $t = 0$ . The  $N = 2$  and  $N = 1$  populations first peaked, then decayed, with the  $N = 2$  peak occurring prior to that of  $N = 1$ . The  $N = 0$  population grew steadily over time, while the other three populations had almost reached zero by the end of the interval. In our current Raman data set, we begin almost every interval with  $N \geq 3$  atoms and rarely with only two. After 250 ms, the most likely case is that we have no atoms,

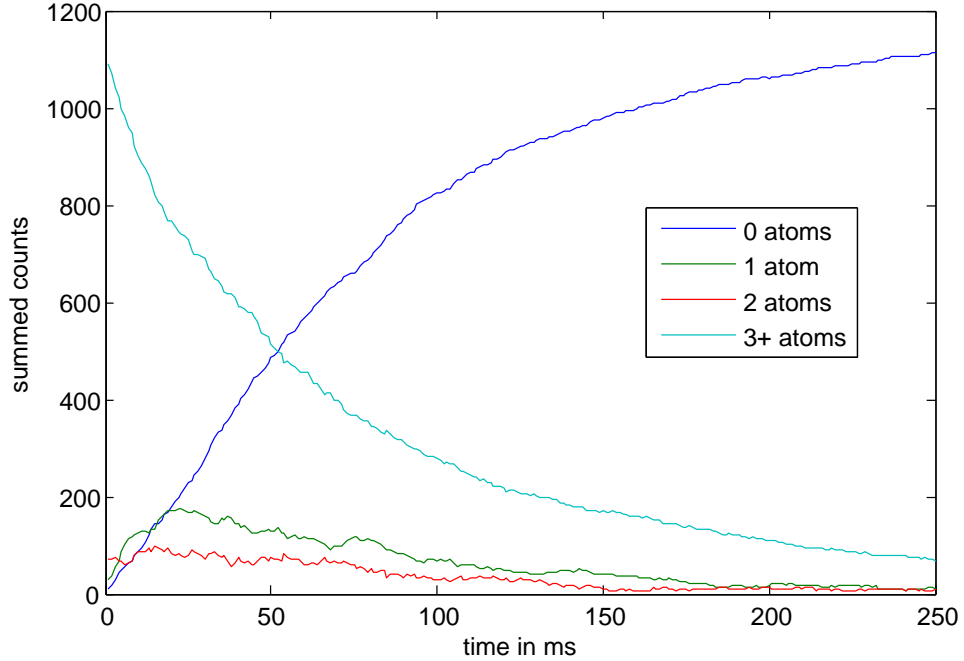


Figure 4.13: Time evolution of the  $N$ -atom populations for for the data set of Figure 4.9

but the second most likely case is that we still have  $N \geq 3$  atoms. Furthermore, despite the continual departure of atoms from the  $N \geq 3$  region, there is no growth in the  $N = 1$  and  $N = 2$  populations after early times. Only the  $N = 0$  population is increasing, and its growth can not be accounted for solely by the departure of atoms from  $N = 1$ .

### 4.3.3 Simulations

Russ has written a Matlab simulation in which  $N$  atoms (on average, with Poissonian statistics) are loaded into the trap, and at any time after loading, there is a fixed probability for an atom to leave. Transmission is given by equation (4.22), with Poissonian noise added. While the time dependence found in these simulations mirrors the observations of Ref. [18], we are not able to adjust the simulation parameters to account for the long multi-atom dwell times we observe in Figures 4.12 and 4.13. However, we do observe qualitative agreement with a second simulation, in which the likelihood for atoms to leave the cavity is described by a simple “catastrophic

event” model; that is, a model in which the initial departure of one atom increases the probability for all other atoms to leave.

A physical basis for such catastrophic events may be the variation in  $g$  over the range of possible FORT wells. Atoms in the best wells couple strongly to the cavity and completely suppress a resonant probe beam, while atoms in poorly coupled wells allow some resonant light from the probe to enter the cavity, and this intracavity field can now heat the atoms out of the trap. We can imagine a scenario in which multiple atoms are trapped in the FORT over a distribution of wells: if only one atom is well-coupled, then it functions as a gatekeeper. Once it leaves, however, probe light enters the cavity, initiating a cascade in which the remaining atoms leave rapidly.

### 4.3.4 Optimizing atom loading

Atom loading takes place within a 5 ms window during which we apply both lattice light from the side of the cavity and Raman beams along the cavity axis. Loading parameters thus include which lattice beams are used ( $F = 3 \rightarrow F' = 3$ ,  $F = 4 \rightarrow F' = 4$ , or both), and the frequency detuning and intensity of these beams. Assuming that our goal is to load as many atoms as possible, we would like to have a means to quantify the number of atoms loaded as a function of these parameters. Unfortunately, because by-the-numbers plateaus scale as  $2^{-N}$ , they provide good discrimination for the  $N = 1$  case but do not allow us to distinguish easily between, for example, 5 and 6 atoms in the cavity.

We introduce the following measurement to compare loading parameters: after loading multiple atoms, we first apply  $F = 4 \rightarrow F' = 4$  lattice light to pump all atoms into the  $F = 3$  manifold. We then drive a short Raman pulse which we expect to transfer the population of each atom to  $F = 4$  about 10–20% of the time; for example, for the data presented in Figure 4.15, we use a Rabi frequency of 140 kHz corresponding to a  $\pi$  pulse time of  $3.5 \mu\text{s}$ , and we drive a 700 ns pulse, where  $\sin^2(\frac{\pi}{2} * \frac{0.7}{3.5}) \approx 0.1$ . Finally, we apply the state detection scheme of Ref. [30] in order to read out with a probe beam whether any atom is in  $F = 4$ . The idea is that the

probability for one or more atoms to be in  $F = 4$  will scale linearly with the number of atoms in the cavity.

Each state detection measurement has a binary result: the atom is either in  $F = 3$  (zero) or  $F = 4$  (one). We perform a series of 1500 measurements per atom, where each measurement lasts about  $110 \mu\text{s}$ , including  $5 \mu\text{s}$  of pumping to  $F = 3$ , one  $700 \text{ ns}$  Raman pulse, and  $100 \mu\text{s}$  of state detection. After accumulating data over hundreds of MOT drops, we average the number of 0 and 1 counts in each of the 1500 trials to find the probability for Raman transfer. From the early data (i.e., trial number  $< 25$ ), we can infer how many atoms were initially loaded. The decay of transfer probability over time provides a gauge of how quickly the atoms leave the trap during the measurement process.

Figure 4.14 shows atom loading data for various combinations of loading beams. The most significant finding is that loading with Raman and  $F = 4 \rightarrow F' = 4$  is about a factor of 5 more effective than our previous method of loading with the two lattice beams alone. Loading with Raman and both lattice beams is worse than the loading with the lattice alone; presumably the heating effects of the lattice repump are still present, but now the Raman may slow its efficiency. Loading with Raman and  $F = 3 \rightarrow F' = 3$  works about half as well as Raman and  $F = 4 \rightarrow F' = 4$ , which may be due to the relative power in the two lattice beams. Additionally, the  $F = 4 \rightarrow F' = 4$  lattice is not very sensitive to detunings between 10 MHz and 20 MHz, but the loading probability drops significantly when the detuning is reduced to 5 MHz. When the lattice beam is resonant with the cavity, we found that loading almost never occurs, and so we were unable to acquire data at that setting. (In these measurements, both  $F = 3 \rightarrow F' = 3$  and  $F = 4 \rightarrow F' = 4$  beams are assumed to be 10 MHz blue-detuned unless otherwise specified.) For this data, the single atom transfer probability is about 20%. However, we did not calibrate the data with respect to a single-atom  $\pi$  pulse and so cannot extract information about overall loading efficiencies.

A second set of atom loading data is shown in Figure 4.15. In this case, the yellow curve (no Raman pulse) establishes a background transfer probability of  $P_{bgd} = 0.01$ ,

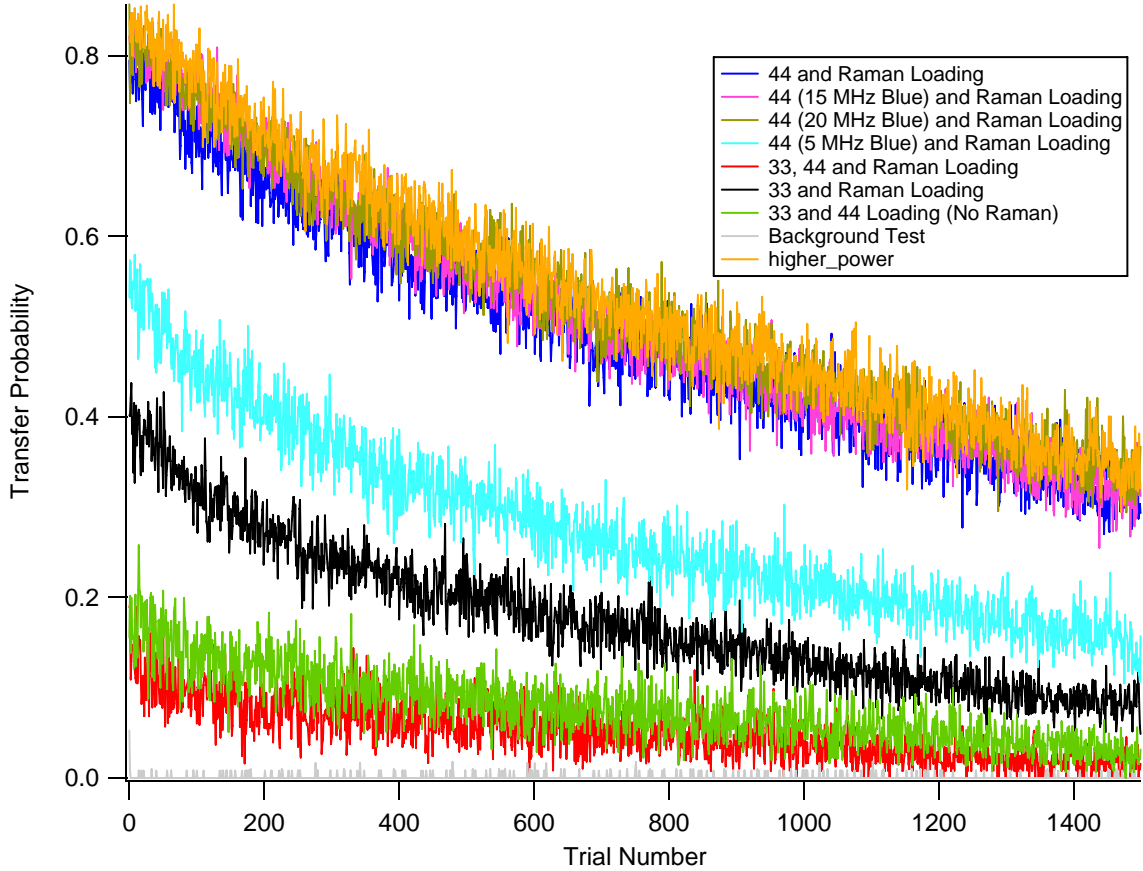


Figure 4.14: Probability for transfer of one or more atoms to  $F = 4$  following a short ( $t < t_\pi$ ) Raman pulse, as a function of trial number, where each trial lasts about  $110 \mu\text{s}$ . The measurement is repeated for various loading beam combinations in order to optimize the number of atoms loaded into the FORT.

and the pink curve (conditional loading of only one atom, discussed in Section 4.4) provides a single-atom reference of  $P - P_{bgd} = 0.06 - 0.01 = 0.05$ . We see that increasing the Raman power from  $-12 \text{ dBm}$  to  $-2 \text{ dBm}$  only improves the loading rate;  $-2 \text{ dBm}$  represents an upper limit on the amount of RF power we can safely use to drive the amplifier for the Raman AOM. Detuning changes to both beams had no appreciable affect. Under the best loading conditions, we find a transfer probability of  $P - P_{bgd} = 0.37 - 0.01 = 0.36$ , corresponding to an average of  $\frac{0.36}{0.05} \approx 7$  atoms loaded per drop. After  $165 \mu\text{s}$  of interrogation, about 4 atoms remain.

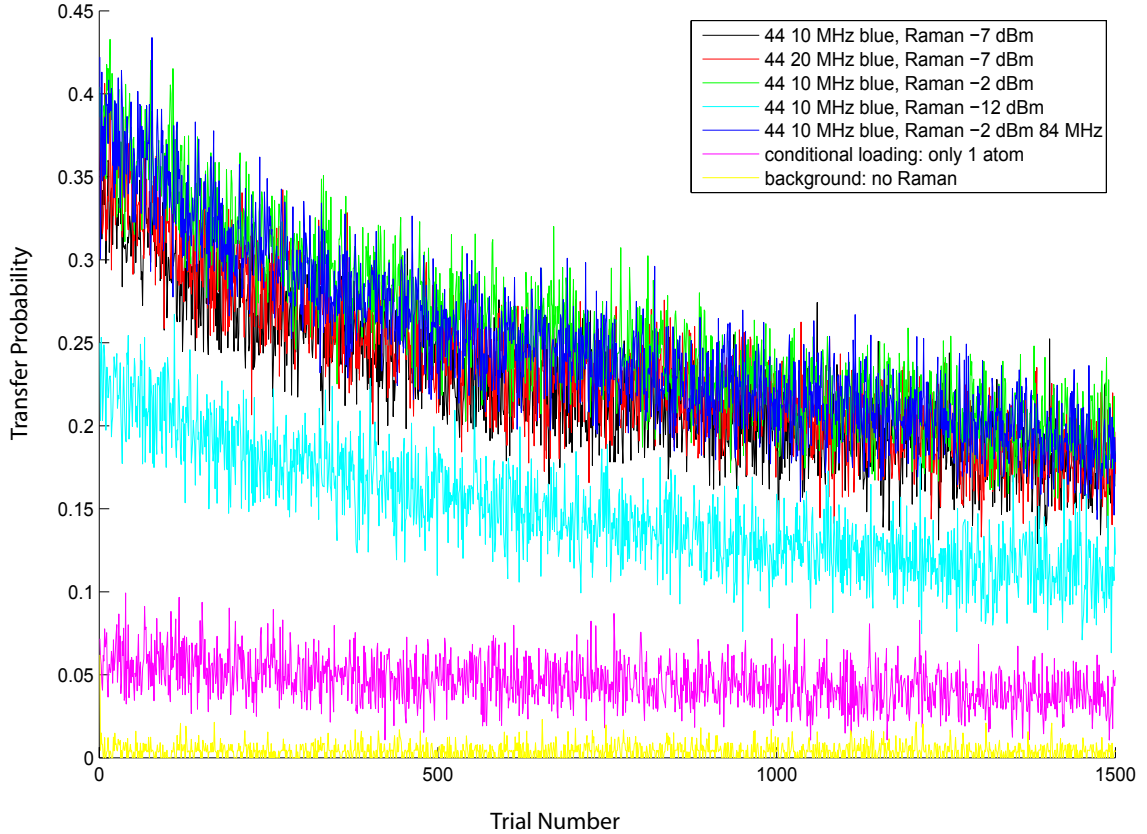


Figure 4.15: Probability for transfer of one or more atoms to  $F = 4$  following a short ( $t < t_\pi$ ) Raman pulse, as a function of trial number, where each trial lasts about  $110 \mu\text{s}$ . The measurement is repeated for various loading beam intensities and detunings in order to optimize the number of atoms loaded into the FORT. A conditional loading measurement provides a single-atom reference probability  $P = 0.05$ .

### 4.3.5 Atom detection with Raman and lattice light

The data in Figure 4.10 suggest that we can use a Raman/probe scheme to identify zero, one, and (less efficiently) two atoms. We have also explored the possibility of introducing  $F = 4 \rightarrow F' = 4$  lattice light in conjunction with the Raman and the probe, in order to shift the histogram features to resolve higher atom numbers. To understand this shift, consider a three-level atom as in Figure 4.16 with ground states  $|a\rangle$  and  $|b\rangle$  and excited state  $|e\rangle$ , where we can drive transitions between  $|a\rangle$  and  $|b\rangle$  at rate  $\alpha$  and between  $|b\rangle$  and  $|e\rangle$  at rate  $\beta$ . (In our system,  $|a\rangle \rightarrow F = 3$ ,  $|b\rangle \rightarrow F = 4$ ,  $|e\rangle \rightarrow F' = 4$ , and  $\alpha$  and  $\beta$  are determined by the Rabi frequency of the Raman pair and the intensity of the lattice light, respectively.) We also include decay from the

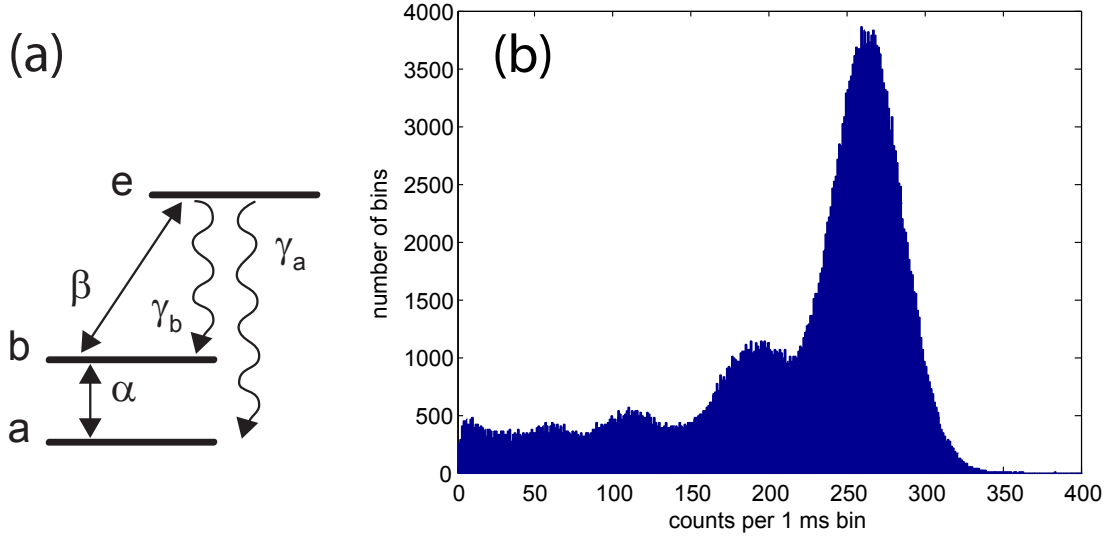


Figure 4.16: Diagram of three-level atom with transition rates  $\alpha$ ,  $\beta$  and decay rates  $\gamma_a$ ,  $\gamma_b$ . Histogram of photon counts per 1 ms time bin, with 250 ms of continuous Raman, probe, and  $F = 4 \rightarrow F' = 4$  lattice beams.

excited state to the two ground states at rates  $\gamma_a$  and  $\gamma_b$ . Then the coupled equations which describe the populations of the three levels are given by

$$\begin{pmatrix} -\alpha & \alpha & \gamma_a \\ \alpha & -\alpha - \beta & \beta + \gamma_b \\ 0 & \beta & -\beta - \gamma_a - \gamma_b \end{pmatrix} \begin{pmatrix} P_a \\ P_b \\ P_e \end{pmatrix} = 0. \quad (4.23)$$

In order to shift the histogram towards higher count rates, we want to minimize the population in  $F = 4$ , that is,  $P_b$ . Solving equation (4.23) for  $P_b$ , we find

$$P_b = \frac{1 + \frac{\gamma_a + \gamma_b}{\beta}}{3 + \frac{2(\gamma_a + \gamma_b)}{\beta} + \frac{\gamma_a}{\alpha}}. \quad (4.24)$$

If  $\beta > \gamma_a, \gamma_b$  and  $\gamma \gg \alpha$ , then  $P_b$  can become very small. Thus, we should reduce the Rabi frequency of the Raman pair and use a high-intensity lattice beam.

Unfortunately, both of these steps tend to increase the noise of the signal. An intense  $F = 4 \rightarrow F' = 4$  beam will heat the atoms, and as we saw in Section 4.3.2, we need a high Rabi frequency to smooth out the atom plateaus. Figure 4.16 shows a histogram from an attempt to use both Raman and lattice beams continuously;

while the  $N \geq 1$  peaks have clearly shifted toward higher count rates, the peak widths prevent effective discrimination. After unsuccessful attempts to find optimal intensity settings for both beams, we have concluded that this is probably not a useful technique for atom number determination.

## 4.4 Conditional feedback to the experiment timing

In the previous sections, we have demonstrated that based on the number of photon counts in a 1 ms window, we can make an accurate determination about the presence of a single atom in the cavity. Here we outline how this information can be used to run the experiment conditioned on real-time atom detection.

The ADwin-Gold system which controls the experiment timing has input and output channels, but until the current application it had only been used to generate output signals (both analog and digital). In the past, we wrote down a sequence of timing commands as a single control program, `timing.in`, using a syntax designed by Dave Boozer. Dave's compiler `hirez.exe` then translated these commands into a text file `foo.txt` written in the ADbasic language. This text was embedded in a larger ADbasic program `pulses.bas` and compiled by the ADwin system. The commands in `timing.in` collected and released the upper and lower MOTs, loaded atoms into the FORT, and then initiated the series of pulses necessary for a particular experiment. Once compiled, a series of commands will loop continuously until a new program is loaded to the ADwin.

To implement conditional loading of the experiment pulses, it was useful to partition the `timing.in` commands into three smaller programs: `timing_load_atom.in`, `timing_one_atom.in`, and `timing_experiment.in`. These programs are then separately compiled to the three text files `foo_load_atom.txt`, `foo_one_atom.txt`, and `foo_experiment.txt` and embedded in `pulses_ten.bas`, which replaces `pulses.bas`.

The command sequence in `timing_load_atom.in` begins with the formation of the upper MOT and ends with loading atoms into the FORT using the Raman and lattice beams. The next step in `pulses_ten.bas` is to initiate a do-until sequence which

calls the `timing_one_atom.in` pulses. These consist simply of 1 ms of continuous Raman and probe fields and a trigger pulse sent to an SR400 Dual-Channel Gated Photon Counter (Stanford Research Systems). After the three pulses, the for-loop then instructs the ADwin to read in the value on the first of its analog channels, which is connected to the analog output from the SR400 and scales linearly with the number of photon counts during the previous ms. Based on histograms such as Figure 4.10, we establish in advance a lower bound of counts corresponding to  $N \leq 1$  atom. The timing program repeats the pulse/read combination until the count threshold is exceeded, that is, until there is at most one atom in the cavity. (For redundancy, the do-until sequence is embedded in a for-loop which requires the count rate to exceed the lower threshold over three 1 ms intervals.) Note that the probe and Raman intervals serve two purposes: they measure the atom number, but they also provide a heating mechanism which induces extra atoms to leave the cavity; this usually occurs within about 50 ms.

Once we have eliminated multi-atom events, we introduce the experiment-specific pulse sequence. However, it is possible that all atoms left the trap during the testing interval. For the sake of efficiency, we only want to run the experiment pulse sequence if we think there is an atom present, though no-atom events will also be detected and eliminated in data processing afterwards. We set an upper threshold for counts corresponding to  $N \geq 1$  atom; only if the number of photon counts per 1 ms interval exceeds this threshold do we load the final sequence of pulses in `timing_experiment.in`. Otherwise, the experimental cycle is skipped and we begin the process again with `timing_load_atom`.

Figure 4.17 shows an histogram for atom-number determination with data acquired as in Figure 4.10, except that here we have implemented the conditional loading scheme described above. We see that peaks associated with  $N \geq 2$  atoms have been eliminated, and only zero- and one-atom peaks remain. There are also a small number of bins with very low count rates, which we have traced to 3 multi-atom events in this data set of 1200 MOT drops. We are unsure as to how these events survived the screening process but are satisfied for the time being with this low contamination

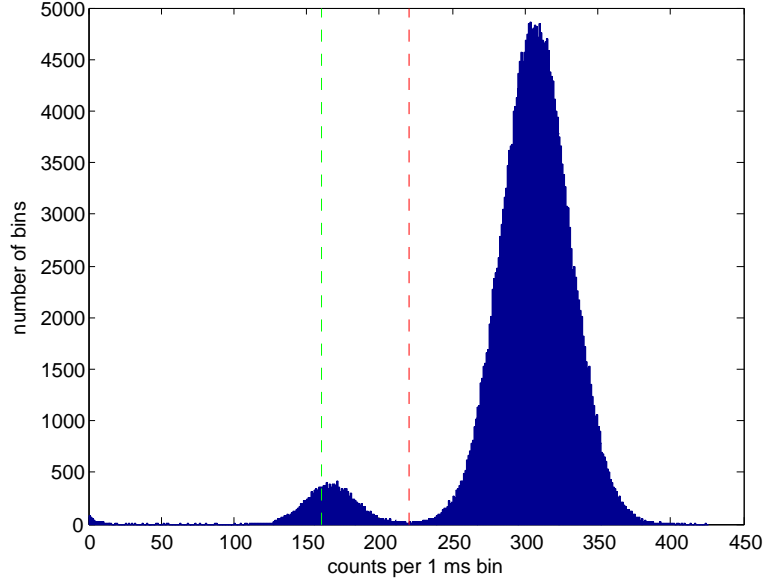


Figure 4.17: Histogram of photon counts per 1 ms time bin, with 280 ms of continuous Raman and probe beams. In contrast to the data presented in Figure 4.10, here we have implemented conditional loading of  $N \leq 1$  atom before the experiment begins, with lower and upper count thresholds indicated.

rate.

Having outlined the conditional loading scheme, I now discuss further details of the SR400 photon counter implementation. We continue to send TTL pulses from our two Perkin-Elmer SPCMs to the P7888 photon counting card for computer-based data acquisition. However, we tee off these signals before the card and send them also to the two channels of the SR400. (Before the SR400, each channel passes through a NOT logic gate which serves as a buffer, to prevent potential damage to the P7888 card.) During each 1 ms gate pulse sent from the ADwin, the SR400 sums the counts on its two inputs. At the end of the gate pulse, it sends out an analog signal between 0 and 10 V which is linear with respect to total counts between 0 and 999; that is, 1 count = 10 mV. This signal returns to the ADwin, which provides 16-bit analog-to-digital conversion of inputs between -10 and 10 V, that is, according to the formula

$$\text{value} = 32767.5 \left(1 + \frac{\text{volts}}{10}\right) = 32767.5 \left(1 + \frac{\text{counts}}{1000}\right). \quad (4.25)$$

We have currently set a lower threshold for conditional detection at 160 counts/ms (value = 38010) and an upper threshold at 220 counts/ms (value = 39976).

We have sometimes found it useful to incorporate a second ADwin analog channel input for real-time feedback to the timing. The second channel is needed when we want to generate a sequence of pulse lengths that vary from atom to atom; for example, the data in Figure 4.7 was obtained with Raman pulse lengths between 0.1 and 100  $\mu$ s. As discussed in Section 3.5, we generate these pulses by using serial commands to program a DG535 pulse generator, then triggering each pulse sequence with a TTL signal from the ADwin. However, the ADwin timing program also needs to know when the pulses are finished; for pulse lengths which vary from atom to atom, a simple way to do this is to have the DG535 put out a signal for the ADwin at the end of its pulse cycle. After the ADwin sends its initial trigger to the DG535, it then polls its second analog channel input until the value crosses a TTL threshold, at which point it continues with the experiment.

We first put conditional feedback into practice for the Raman optical pumping results presented in Section 4.1 and in [32]. We were pleased to see a number of immediate results: not only did it speed up the process of data acquisition, but also we found that our single-atom Raman scans had reduced background levels, and that the measured Zeeman populations summed to the expected value. (Both of these effects can be understood in the context of multi-atom contamination: when more than one atom is trapped in the cavity, there is a greater probability that an off-resonant Raman pulse will transfer population to  $F = 4$ , increasing background levels, and we also expect an increased probability to find one atom in any given Zeeman level.) Implementing conditional feedback into our field-nulling protocol (e.g., Figure 2.2) has also improved the contrast of these scans and allowed us to set magnetic field values more reliably. Further applications for this scheme include improved generation of single photons; we would expect a stronger suppression of two-photon events than observed in Ref. [16]. Meanwhile, single photon generation combined with optical pumping might allow us to produce photons with narrower temporal pulse shapes, as the long tail observed in Ref. [16] was attributed to atoms trapped in dark states.

## Chapter 5

# Toward atom-photon entanglement

The tools that we have developed over the past few years for control and interrogation of our atom-cavity system have brought us to the point where we can now implement complex protocols in the lab. Our current efforts focus on one such protocol, which would generate entanglement between the polarization states of a photon and the Zeeman states of a trapped atom. In Section 5.1, I describe the details of this entanglement scheme. Section 5.2 discusses the use of Rabi flops to characterize decoherence in our system; an understanding of decoherence mechanisms is necessary in order to determine whether we will be able to demonstrate entanglement. Section 5.3 presents our method for mapping superpositions of Zeeman states to hyperfine states that we have developed in the context of this entanglement project. In order to quantify the coherence of the mapping, we vary the phase between two arms of this process and generate a fringe. Section 5.4 centers on the final step in the protocol: fast pulses from the side of the cavity that excite the atom to the  $F' = 5$  manifold. Here I also discuss the current outlook for the project.

### 5.1 Atom-photon entanglement scheme

The concept of atom-photon entanglement lies at the heart of cavity-QED-based schemes for quantum networking. These schemes rely on entanglement in order to transfer information coherently between long-lived atomic superpositions (quantum nodes) and photonic states in optical fiber (quantum channels). In Chapter 3 of

this thesis, I discuss one such mapping, between cesium hyperfine manifolds  $F = 3$  and  $F = 4$  and photon Fock states  $|0\rangle$  and  $|1\rangle$ . However, a more robust scheme would entangle the atomic state with photon polarization rather than photon number. Losses in the optical path will inevitably degrade the entangled state: if the original composite system is given by

$$|\psi\rangle = |a_1\rangle \otimes |p_1\rangle + |a_2\rangle \otimes |p_2\rangle, \quad (5.1)$$

where  $a_{1,2}$  and  $p_{1,2}$  are atom and photon states, then after propagation, the density matrix  $\rho = |\psi\rangle\langle\psi|$  becomes

$$\rho' = (1 - p_E)(|a_1\rangle + |a_2\rangle)(\langle a_1| + \langle a_2|) \otimes |0\rangle\langle 0| + p_E|\psi\rangle\langle\psi|, \quad (5.2)$$

where the entanglement probability  $p_E$  is determined by path losses and  $|0\rangle$  represents the absence of a photon. In the case of the Fock state mapping, if we do not detect a photon at the cavity output, we cannot distinguish whether this corresponds to  $p_1$  (and thus to  $a_1$ ) or to  $|0\rangle$ . For polarization states, however, decoupling photon number from entanglement means that we can restrict ourselves to a heralded, effective entangled state  $|\psi\rangle\langle\psi|$  with probability  $p_E$  [103].

Recent work in Gerhard Rempe's group has shown that it is possible to control photon polarization based on the Zeeman state of an atom within a cavity [82, 83]. A magnetic field along the cavity axis is used to split out the Zeeman levels of  $^{87}\text{Rb}$ , and the cavity is tuned into resonance with the  $F = 1 \rightarrow F' = 1$  transition between the  $5S_{1/2}$  and  $5P_{3/2}$  manifolds. For an atom prepared in  $|F = 2, m_F = 0\rangle$ , an initial STIRAP process driven by a laser on the  $F = 2 \rightarrow F' = 1$  transition will either a) transfer the atom to the  $|1, -1\rangle$  ground state while generating a cavity photon with  $\sigma^+$  polarization, or b) transfer the atom to  $|1, 1\rangle$  while generating a  $\sigma^-$  photon. A second STIRAP process on the  $F = 1 \rightarrow F' = 1$  transition is conditional on the result of the first: a  $\sigma^-$  photon is generated if the atom is in  $|1, -1\rangle$ , and a  $\sigma^+$  photon if the atom is in  $|1, 1\rangle$ . Thus, alternating the two classical laser pulses creates

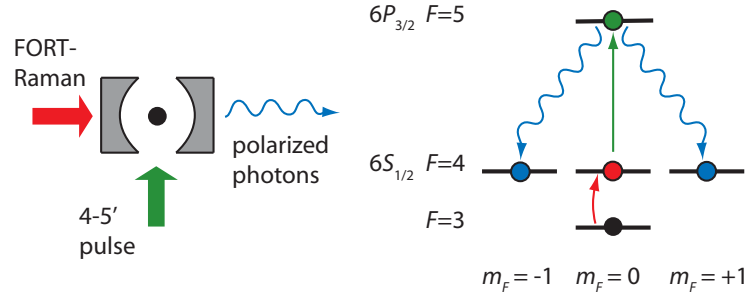


Figure 5.1: Scheme for generating entanglement between the polarization states of a photon and the Zeeman states of a trapped atom. We optically pump a cesium atom to  $|3, 0\rangle$ , then transfer it to  $|4, 0\rangle$  via a Raman  $\pi$  pulse. A fast pulse from the side of the cavity excites the atom to  $|5', 0\rangle$ . Atomic decay into the cavity mode will generate a circularly polarized photon; a  $\sigma^+$  photon corresponds to the final atomic state  $|4, -1\rangle$ , and a  $\sigma^-$  photon corresponds to  $|4, 1\rangle$ .

sequential pairs of polarization-entangled photons, which can be detected in the cavity transmission path [83]. While these experiments represent a significant step towards quantum networking, it is important to note that they were done with atoms falling through the cavity mode. For information storage in quantum nodes, we require photon generation using trapped, localized atoms that could then be re-addressed at later times. In addition, we would like to quantify atom-photon entanglement directly by reading out the atomic state rather than by generating a second photon. As our efficient method of state detection [30] only distinguishes between hyperfine manifolds, we will first have to introduce a mapping between Zeeman and hyperfine states.

We begin our protocol by preparing a single cesium atom in  $|4, 0\rangle$ . (In practice, we use the methods of Chapter 4 to prepare the atom in  $|3, 0\rangle$ , then transfer the population to  $|4, 0\rangle$  via a Raman  $\pi$  pulse.) As in the Rempe experiment, a magnetic field splits out the Zeeman states, and we define a quantization direction along the magnetic field axis. A  $\sim 10$  ns  $\pi$ -polarized optical pulse from the side of the cavity resonant with the  $F = 4 \rightarrow F' = 5$  transition excites the atom. Because the pulse is polarized along the cavity axis, the cavity mode only supports atomic decay to states  $|4, 1\rangle$  and  $|4, -1\rangle$ , with  $\sigma^-$  and  $\sigma^+$  polarization, respectively. Photon polarization is straightforward to detect with waveplates and beamsplitters at the cavity output. To

read out the atomic state, we want to map superpositions of  $|4, 1\rangle$  and  $|4, -1\rangle$  onto  $F = 3$  and  $F = 4$ , as we are able to measure superposition states of the hyperfine manifolds. We apply two simultaneous Raman  $\pi$  pulses tuned to the  $|4, 1\rangle \rightarrow |3, 0\rangle$  and  $|4, -1\rangle \rightarrow |3, 0\rangle$  transitions, where the  $\Delta m = \pm 1$  transitions rely on a component of the magnetic field transverse to the cavity axis; we expect the populations to interfere constructively or destructively depending on the relative phase of the two initial states, so that as a function of phase, the atom will either be transferred to  $F = 3$  or remain in  $F = 4$ .

Section 5.3 presents our efforts to characterize this interference process. First, however, we note that our scheme relies on carefully tuned Raman pulses at three different frequencies, two of which are sensitive to the magnetic field. In the following section, then, we investigate the decoherence mechanisms underlying our Raman technique to understand whether this is feasible.

## 5.2 Rabi flops

### 5.2.1 Theory

The Bloch equations describe the evolution of a spin system in an applied field [104]; while these equations were first introduced to describe magnetic resonance phenomena, they also apply to a two-level atom driven by an optical field, or to our current situation, in which two atomic ground states are coupled via Raman transitions. The Rabi solution of the Bloch equations for a resonant driving field shows that population initially prepared in one spin state will be driven coherently back and forth between the two states, a process known as “Rabi flopping.” The rate of population transfer is given by the Rabi frequency  $\Omega$ , which is proportional to the square root of the intensity of the driving field. Specifically, the duration of a “ $\pi$  pulse,” that is, the time required to transfer population from one state to the other, is given by

$$t_\pi = \frac{\pi}{\Omega}. \quad (5.3)$$

For a driving field detuned from resonance by  $\Delta$ , the population transfer as a function of time is given by the equation

$$P(t) = \frac{\Omega^2}{\Omega^2 + \Delta^2} \sin^2 \sqrt{\Omega^2 + \Delta^2} t / 2 \quad (5.4)$$

where  $P(t)$  corresponds to the fraction of the population transferred from the initial to the final spin state. Thus in the off-resonant case, the oscillation frequency is faster, but complete inversion between the two states is never achieved.

A more realistic model incorporates phenomenological decay processes into the Bloch equations [104]. The result is that Rabi oscillations are exponentially damped according to a set of characteristic decay times. Conversely, in order to study the decoherence mechanisms within an experiment, one simple technique is to measure Rabi flopping amplitudes and damping rates. In particular, Rabi flops have become an important benchmark for the quantum computing community, as the number of sequential gates that a quantum computer could perform is limited by the ratio of the decay time to  $t_\pi$ .

Several processes contribute to spin decoherence. In the notation used by the nuclear magnetic resonance (NMR) community, the longitudinal decay time  $T_1$  describes population relaxation to thermal equilibrium;  $T_1$  decay is due to spin-lattice coupling in NMR, but in our experiments it is negligible. Meanwhile, the transverse decay time  $T_2$  can be decomposed into two components,

$$\frac{1}{T_2} = \frac{1}{T_2'} + \frac{1}{T_2^*}. \quad (5.5)$$

Here  $T_2'$  describes homogeneous, incoherent processes, and  $T_2^*$  describes inhomogeneous effects. Note that often when we think of homogeneous and inhomogeneous processes, we imagine a macroscopic ensemble, such as a collection of spins in a crystal or an atom cloud. Homogeneous effects such as collisions would effect all spins identically, while inhomogeneous effects would assign a different value of some property to each spin, such as velocity in the case of Doppler broadening. Here we are dealing

with one atom at a time within a cavity, but the ensemble picture is valid because we collect data over a series of hundreds or thousands of atoms, and we repeat a measurement hundreds of times for each atom. In this case, inhomogeneous  $T_2^*$  mechanisms may result from changes over time: for example, variation in the intensity of the Raman beams, or gradual heating of the atoms throughout the Raman process, both of which would effectively assign a different Raman frequency to each flopping measurement. Another potential  $T_2^*$  mechanism is the finite temperature of each atom within the FORT, resulting in a periodic modulation of the Rabi frequency. (Because the intensities of both FORT and Raman beams have a Gaussian profile, the Rabi frequency seen by the atoms is spatially dependent.) For field-sensitive transitions, drifts in the magnetic field over time would result in a range of possible detunings from Raman resonance. Meanwhile,  $T_2'$  mechanisms could include phase noise on the injection lock between the FORT and Raman lasers, or scattering due to stray light.

The exponential decay that damps Rabi oscillations is given by  $T_2$ . In order to separate out the components of  $T_2$ , we must turn to other techniques, such as Ramsey interferometry. Here one prepares the sample in an initial spin state, then applies a  $\pi/2$  pulse with detuning  $\Delta$  in order to rotate the spins into the x-y plane of the Bloch sphere picture (in a frame rotating at the frequency difference between the two spins). The spins precess in the plane with frequency  $\Delta$ , so that if we apply a second  $\pi/2$  pulse after a variable time  $t$ , we will observe Ramsey oscillations at frequency  $\Delta$ . However, as the spins precess in the plane, they also drift out of phase with one another, so the oscillations that we measure will be exponentially damped at some rate. The point is that every measurement consists of two  $\pi/2$  pulses separated by a time  $t$ , which is varied while the system is “in the dark” to applied fields. Thus, decoherence mechanisms that accumulate in Rabi oscillations as a function of pulse length (for example, scattering due to the applied fields) will be constant over the Ramsey data set and will only affect the amplitude of oscillations, not their rate of decay. Also, note that inhomogeneous mechanisms that cause a variation in  $\Omega$  will not contribute, as long as the effective pulse lengths are reasonable approximations of  $\pi/2$ . Ramsey decoherence is the result of inhomogeneities in detuning from Raman

resonance, which cause different precession frequencies for each measurement.

Thus, Ramsey interferometry can give us information about a smaller subset of decoherence mechanisms on our experiment: those effects dependent on either magnetic field or temperature. Temperature-dependent decoherence may come as a surprise, given the statement above that finite atom temperature results in a spread of Rabi frequencies, to which Ramsey interferometry should be insensitive. However, atom temperature also produces a spread in detunings, given the FORT-induced differential AC-Stark shift in our experiment. Consider that the free-space hyperfine splitting  $\Delta_{HF}$  between cesium ground states  $F = 3$  and  $F = 4$  is modified by 20 kHz at the bottom of each FORT well; halfway up the FORT well, the differential shift is only 10 kHz. Thus, as an atom moves within this potential, it experiences frequency shifts on the order of 10 kHz with respect to the frequency of the Raman pair. Depending on the Raman linewidth — that is, the Rabi frequency — this may be a significant effect.

Spin echo is a second diagnostic technique that we can apply to the problem of decoherence. Known as “photon echo” in the optical case, it allows us to recover some of the coherence lost to dephasing in Ramsey interferometry. Here we follow the Ramsey scheme above, using a fixed precession time  $t$  in the x-y plane, except that now we insert a  $\pi$  pulse at time  $t/2$ . This flips each precessing spin with respect to the x axis, so that the “fast” spins now lag behind the “slow” ones. After another  $t/2$  interval, all the spins are back in phase, and the second  $\pi/2$  pulse should rotate them to the Bloch sphere pole opposite where they began. However, rephasing only occurs for coherent decay mechanisms that are constant over  $t$ , so that the second  $t/2$  interval “undoes” the first. Thus, any damping of photon echo amplitude as a function of time allows us to characterize  $T_2'$  as well as rapidly varying  $T_2^*$  mechanisms, such as fast magnetic field fluctuations.

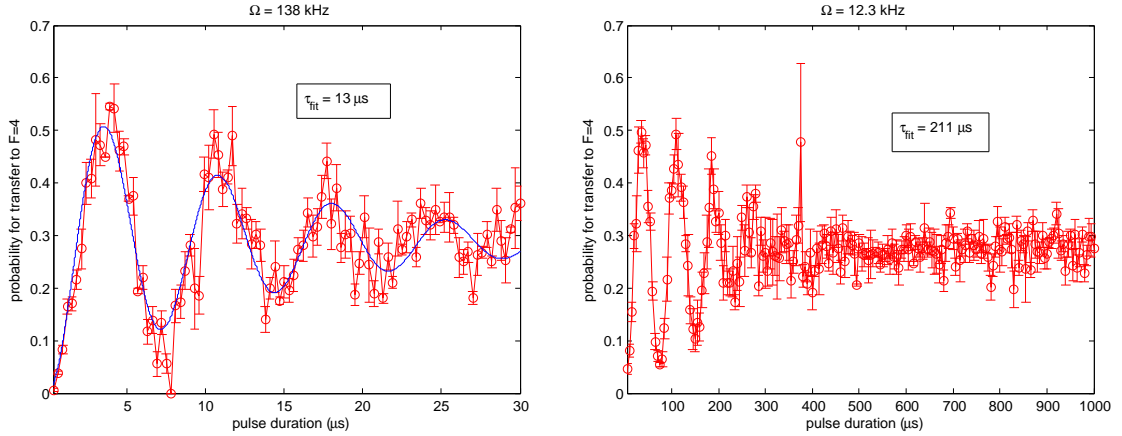


Figure 5.2: Rabi flops on the  $|3, 0\rangle \leftrightarrow |4, 0\rangle$  resonance at  $\Omega = 138$  kHz and  $\Omega = 12.3$  kHz. For each measurement, atoms are prepared with roughly 60% efficiency in  $|3, 0\rangle$ , then driven with a Raman pulse of varying duration, followed by state detection.

### 5.2.2 Rabi flopping measurements

Given the that our FORT and Raman beams are linearly polarized, mutually orthogonal, and propagate along the cavity axis, we can drive Raman transitions between pairs of Zeeman states with Rabi frequency  $\Omega_E$ :

$$\langle 4, m | \hat{\Omega}_E | 3, m \rangle = \sqrt{1 - m^2/16} \Omega_0 \cos \theta \quad (5.6)$$

$$\langle 4, m + 1 | \hat{\Omega}_E | 3, m \rangle = -\frac{1}{8} \sqrt{(4 + m)(5 + m)} \Omega_0 \sin \theta \quad (5.7)$$

where  $\Omega_0$  is the Rabi frequency for the  $m = 0$  pair and  $\theta$  is the angle between the cavity axis and the quantization axis, which we define along the applied magnetic field [19]. We see that  $\Omega_E$  is  $m$ -dependent, so that in order to observe single-frequency oscillations, we will need to apply a magnetic bias field so that we can address only one pair at a time. A quantization axis along the cavity axis ( $\theta = 0$ ) will allow  $\Delta m = 0$  transitions while suppressing  $\Delta m = \pm 1$ . For high-contrast oscillations, we must be able to prepare atoms in a given initial Zeeman state; atoms prepared in the wrong state will not be addressed by the Raman frequency, so they will not contribute to decoherence, but they will result in a reduced amplitude.

The first demonstrations of Rabi flopping in our lab used conventional optical

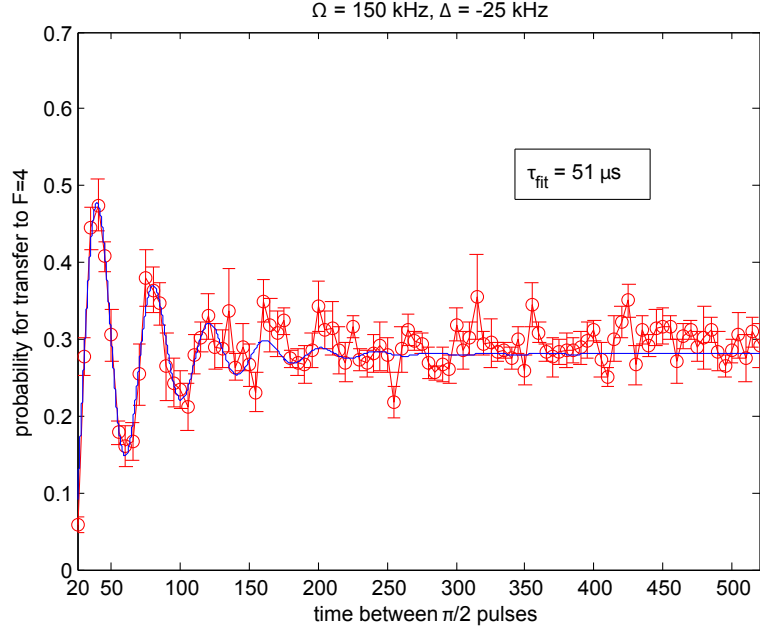


Figure 5.3: Ramsey interferometry at  $\Omega = 150$  kHz, with detuning  $\Delta = -25$  kHz from the  $|3, 0\rangle \leftrightarrow |4, 0\rangle$  transition. Atoms are prepared in  $|3, 0\rangle$ , then driven with a pair of  $\pi/2$  pulses separated by a variable time  $t$ , followed by state detection. The number of coherent oscillations is roughly the same as for Rabi flopping measurements (Figure 5.2).

pumping techniques to prepare atoms in  $|F = 3, m_F = 0\rangle$  [19], but we now rely on the method presented in Section 4.1; one advantage is that this allows us to compare the field-insensitive  $|3, 0\rangle \leftrightarrow |4, 0\rangle$  transition with the other six field-dependent transitions. After conditional loading and optical pumping, we are left with a single atom in a given  $F = 3$  sublevel. We drive Raman transitions at a fixed Rabi frequency for a variable time  $t$ , then perform state detection to determine the probability of transfer to  $F = 4$  [30]. Sample Rabi flopping traces on  $|3, 0\rangle \leftrightarrow |4, 0\rangle$ , accumulated over a series of atoms, are shown in Figure 5.2.

We emphasize two observed features of field-insensitive Rabi flops in our experiment that provide insight into the decoherence mechanisms at work. First, we find that  $T_2$  decay times are inversely proportional to Rabi frequency  $\Omega$ . Thus, independent of  $\Omega$ , an atom driven on resonance undergoes the same number of coherent flops (about three) before decoherence takes over. This effect can be seen in Figure 5.2, where the traces shown appear qualitatively similar despite the order of magnitude

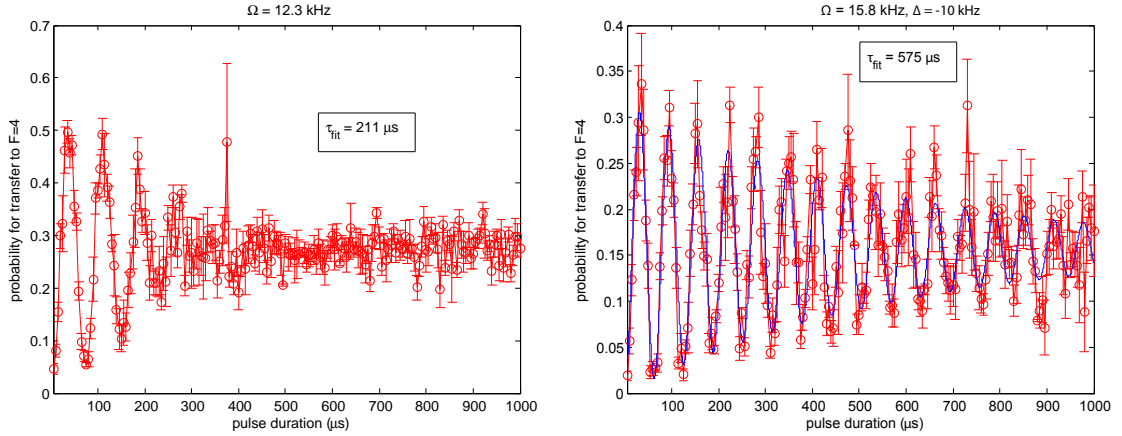


Figure 5.4: Two Rabi flopping measurements at similar Rabi frequencies, one on resonance and the other red-detuned by  $\Delta = -10$  kHz. The on-resonance data is reproduced from Figure 5.2 for comparison; note that detuning to the red increases the damping time constant by almost a factor of three.

difference in  $\Omega$ . Furthermore, Ramsey interferometry (Figure 5.3) does not extend the number of coherent oscillations, so we can rule out mechanisms to which Ramsey methods are insensitive, such as variation in Raman intensity and phase noise on the injection lock. We conclude that temperature effects are probably the cause of dephasing. Atoms with a finite temperature are not localized at the FORT minima; because of the spatial dependence of  $\Omega$ , our flopping measurement occurs over an ensemble of atoms with a range of Rabi frequencies, and the measured ratio of  $T_2$  to  $t_\pi$  tells us about this range.

A second, more perplexing finding is that by detuning the Raman pair to the red of resonance (negative  $\Delta$ ), we are able to improve coherence times. This is shown in Figure 5.4 for the case  $\Delta = -25$  kHz at a Rabi frequency of 150 kHz, parameters for which we have observed the most significant improvement. In contrast, detuning the Raman pair to the blue side of resonance (positive  $\Delta$ ) somewhat degrades the coherence, though this is not as strong an effect. We now believe that this detuning dependence is due to the FORT-induced differential AC-Stark shift described in Section 5.2.1. Depending on an atom's temperature and thus location in the FORT potential, it may be in or out of resonance with the Rabi frequency of the Raman pair; due to the AC-Stark shift, the detuning  $\Delta$  is spatially dependent. By detuning to the

red, we shift the Raman pair out of resonance with all atoms, so that only the coldest atoms will see an appreciable field; in this way, we are narrowing the distribution of Rabi frequencies in our experiment. David Boozer has written computer simulations that include this AC-Stark shift effect, and we find that they are in good agreement with our data.

Finally, one may ask if there are additional limits placed on  $T_2$  in the case of field-sensitive ( $m \neq 0$ ) transitions. Preliminary evidence suggests that this may be the case. However, with Rabi flopping measurements, it is difficult to distinguish between fast magnetic field drifts (on the timescale of decoherence for each atom) and slow drifts (on the timescale of the measurement over the ensemble). Based on sequential Raman spectrum measurements of the  $|3, 1\rangle \leftrightarrow |4, 1\rangle$  transition, we have evidence for drifts of  $\sim 10$  kHz in the course of an hour. We have demonstrated spin echo for the  $m = 0$  transition (Figure 5.5), but it would be interesting to apply this technique in the field-sensitive case: as photon echo should be insensitive to slow field drifts, a measurement of pulse amplitude as a function of precession time would provide information about fast fluctuations.

While Rabi flopping measurements have helped us to understand the limitations of our experiment, they also provide more direct insight on the prospects for atom-photon entanglement. We have seen that there is minimal decoherence over the course of a single  $\pi$  pulse, which is encouraging. However, in the case of  $\pi$  pulses on the  $|3, 0\rangle \leftrightarrow |4, \pm 1\rangle$  transitions, magnetic field drifts are a cause for concern. We should expect to use Rabi frequencies much faster than the  $\sim 10$  kHz drift range so that the transitions do not shift out of resonance in the course of the experiment. As we will see in the following sections, this imposes a severe restriction if we would like to replace optical Raman processes by driving ground state transitions directly with microwaves.

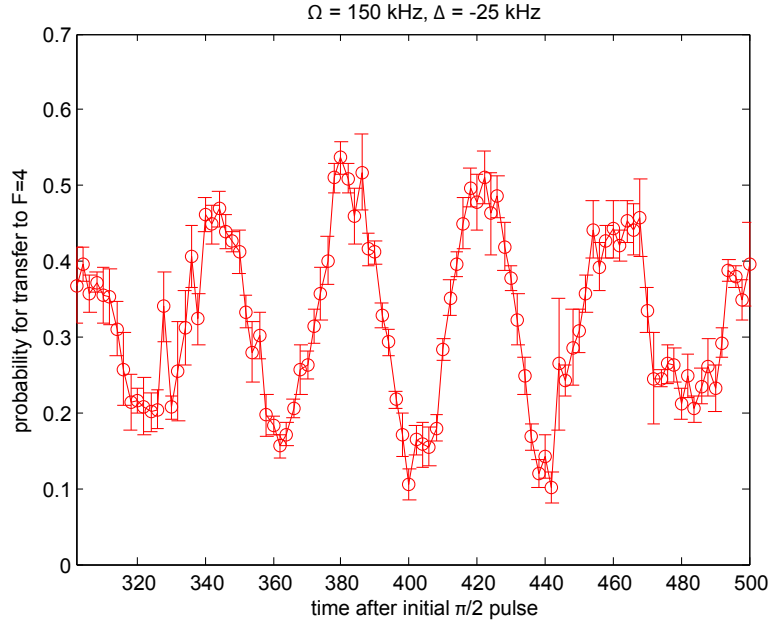


Figure 5.5: Spin echo measurement at  $\Omega = 150 \text{ kHz}$ , with detuning  $\Delta = 25 \text{ kHz}$  from the  $|3, 0\rangle \leftrightarrow |4, 0\rangle$  transition. Atoms are prepared in  $|3, 0\rangle$ , then driven with a  $\pi/2$  pulse at time  $t = 0$ , a  $\pi$  pulse at  $t = 200 \mu\text{s}$ , and a second  $\pi/2$  pulse at variable time  $t$  between 300 and 500  $\mu\text{s}$ . The pulse sequence is followed by state detection. Note the revival of the Ramsey oscillations of Figure 5.3, with no observed reduction in amplitude.

### 5.3 Zeeman to hyperfine mapping

A significant challenge in demonstrating the proposed mapping from Zeeman to hyperfine states has been to implement  $\Delta m = \pm 1$  transitions in our experiment. We have attempted this using various methods, each of which has presented its own set of drawbacks. We have been most successful in driving Raman transitions in the presence of a magnetic field transverse to the cavity axis, as well as in preliminary efforts with microwaves. I begin, however, with a discussion of our earlier attempts, which may provide some insight into the technical limitations of our experiment.

#### 5.3.1 936 nm Raman transitions from the side of the cavity

In the presence of a bias field along the cavity axis, our current FORT-Raman configuration only drives  $\Delta m = 0$  transitions. One means of accessing  $\Delta m = \pm 1$  transitions is to replace the Raman beam with a beam from the side of the cavity at the same fre-

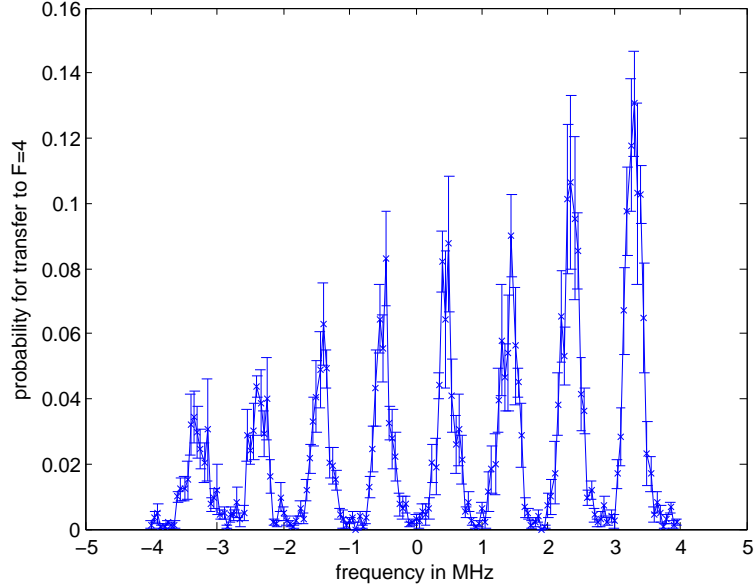


Figure 5.6: We replace the on-axis Raman beam with a 936 nm beam from the side of the cavity in order to drive  $\Delta m = \pm 1$  transitions. We apply a magnetic field along the cavity axis and prepare atoms in  $F = 3$ , then measure the probability to transfer population to  $F = 4$  after  $150 \mu\text{s}$  Raman pulses, as a function of Raman detuning. The Raman spectrum now consists of eight possible  $m$ -changing frequencies: six degenerate pairs and two edge transitions.

quency, but polarized along the cavity axis; in this case, the vector orthogonal to the FORT-Raman polarization is also orthogonal to the quantization axis, and  $\theta = \pi/2$  in equations (5.6) and (5.7). We have successfully demonstrated Raman transitions in this configuration (Figure 5.6). Note that a Raman spectrum consists of eight possible  $m$ -changing frequencies, interleaved between the seven  $\Delta m = 0$  transition frequencies. Six of the frequencies correspond to pairs of transitions:  $|3, m\rangle \rightarrow |4, m+1\rangle$  and  $|3, m+1\rangle \rightarrow |4, m\rangle$  are degenerate for  $m = \{-3, -2, \dots, 1, 2\}$ . The two edge transitions  $|3, 3\rangle \rightarrow |4, 4\rangle$  and  $|3, -3\rangle \rightarrow |4, -4\rangle$  are nondegenerate.

Unfortunately, we encountered two problems driving transitions in this configuration: first, we were limited by the power available in our Raman diode laser. With 2.2 mW of power focused from the side of the cavity, we found that it took about  $150 \mu\text{s}$  to transfer population between the hyperfine ground states. Second and more problematic was the fact that we were unable to observe Rabi flops between  $F = 3$  and  $F = 4$  after preparation in  $m_F = 0$ ; the population as a function of time simply

began in one state and ended in the other, just as for the incoherent Raman transfer of Figure 4.7. We now believe that this is likely due to diffraction of the Raman side beam by the cavity mirrors, which results in significant intensity variation over the possible FORT wells. This means that each well has a different rate for population transfer, and we would not be able to set a well-defined  $\pi$  pulse time in our experiments.

### 5.3.2 852 nm Raman transitions from the side of the cavity

At the time, we did not yet appreciate the role of diffraction in driving transitions from the side of the cavity. We believed that our failure to observe Rabi flops was due to the slow time for population transfer between ground states, during which decoherence mechanisms might play a significant role. In search of less stringent power requirements and faster Raman transitions, we switched to a pair of Raman lasers at 852 nm, detuned 3 GHz to the red of the cesium  $D2$  resonances. The new lasers were set up in an adjoining lab (the former lab 1 cavity QED experiment, now relocated to lab 9); as in our 936 nm Raman pair, a 9.2 GHz frequency sideband applied to one laser was used to injection-lock the second. We monitored this injection lock by combining light from both lasers on a fiber beamsplitter with a laser locked to the cesium resonance and monitoring the optical beat note on a spectrum analyzer. The light from the Raman pair was brought to the cavity via optical fiber and focused in through the side.

We were again unable to observe Rabi flopping on individual Zeeman transitions. In retrospect, of course, this method suffers from the same side-beam diffraction problems as the previous 936 nm Raman attempt. However, we were able to observe incoherent  $\Delta m = \pm 1$  Raman spectra using 10  $\mu\text{s}$  pulses, an order of magnitude faster than with the 936 nm Raman pair.

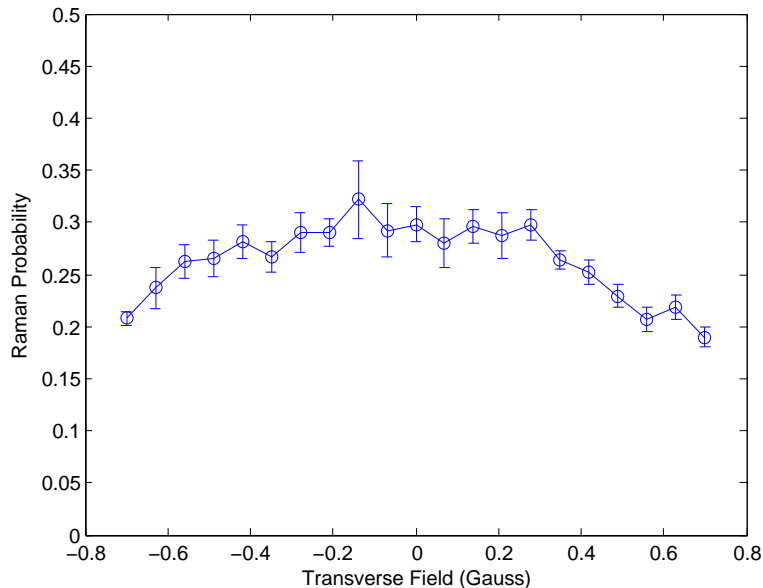


Figure 5.7: We measure the probability to optically pump into the state  $|3, 0\rangle$  as a function of a transverse magnetic field applied in addition to a constant axial field of 1.21 Gauss. The transfer probability to  $F = 4$  after optical pumping is measured using incoherent Raman transitions, with a maximum possible value of 0.5.

### 5.3.3 Raman transitions using a transverse field

A third scheme for driving  $\Delta m = \pm 1$  transitions relies on our original FORT-Raman pair, but requires us to apply a small transverse magnetic field on top of the axial field already present. We see from equation (5.7) that for small  $\theta$ , the Rabi frequency for  $\Delta m = \pm 1$  transitions is small, but as we increase  $\theta$ , we will be able to drive  $m$ -changing transitions more rapidly. On the other hand, a nonzero  $\theta$  means that the quantization axis and the cavity axis are no longer the same; specifically, the polarization modes supported by the cavity do not correspond exactly to decay from  $|5', 0\rangle$  to  $|4, \pm 1\rangle$  as in Figure 5.1, and there is now some  $|4, 0\rangle$  component. By keeping the transverse field small with respect to the axial field, we hope to minimize this effect.

Our initial concern was that with the addition of the transverse field, the effectiveness of our optical pumping to  $|3, 0\rangle$  would be reduced because of mixing between states. However, measurements of population prepared in  $|3, 0\rangle$  as a function of field strength showed that this was a small effect, significant only for strong transverse fields

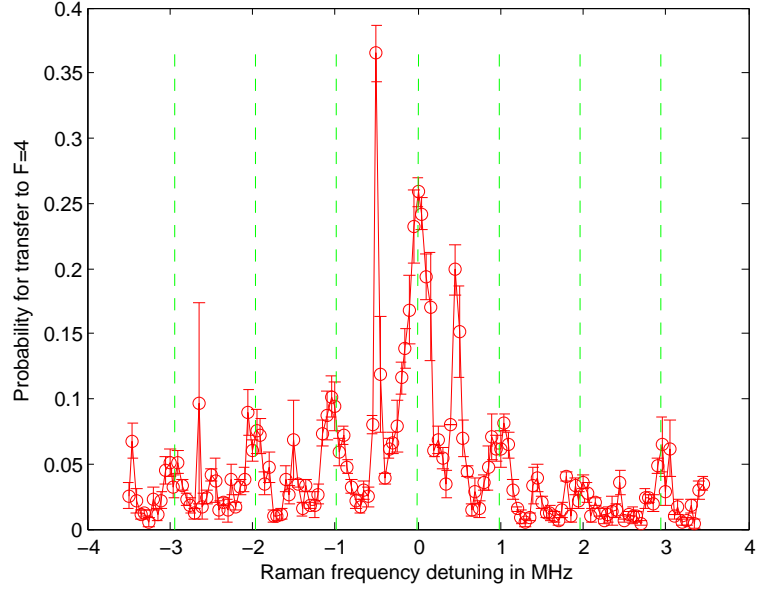


Figure 5.8: We prepare atoms in  $|3, 0\rangle$  and measure a Raman spectrum as in Figure 4.6, but in the presence of an 0.52 Gauss transverse field on top of a 1.21 Gauss axial field. Spaced between the  $\Delta m = 0$  transitions indicated by dashed vertical lines, we see  $\Delta m = \pm 1$  transitions, most prominently from  $|3, 0\rangle$  to  $|4, \pm 1\rangle$ . As the Rabi frequencies are lower for these transitions (equation (5.7)), the Raman pulse time is not long enough for decoherence to occur, so the measured transition probabilities have not yet reached their asymptotic values.

(Figure 5.7). We then measured Raman spectra in the presence of a 0.5 Gauss transverse field after optical pumping to identify transition frequencies for  $|3, 0\rangle \rightarrow |4, \pm 1\rangle$  (Figure 5.8).<sup>1</sup> We have confirmed that we can drive Rabi flops on these frequencies, both individually and jointly (Figure 5.9). In the case where both  $|3, 0\rangle \rightarrow |4, 1\rangle$  and  $|3, 0\rangle \rightarrow |4, -1\rangle$  transitions are driven simultaneously, we expect the effective Rabi frequency to increase by a factor of  $\sqrt{2}$ .

We have investigated our ability to map a superposition state of  $|4, \pm 1\rangle$  onto the hyperfine manifolds  $F = 3$  and  $F = 4$  in the following manner: we prepare an atom in  $|3, 0\rangle$ , then drive it with two simultaneous  $\pi$  pulses on the  $|3, 0\rangle \rightarrow |4, 1\rangle$  and  $|3, 0\rangle \rightarrow |4, -1\rangle$  transitions. (We thus prepare a superposition state analogous to the

<sup>1</sup>This transverse field is almost half the size of the axial field and thus larger than we would use for entanglement purposes. However, it allows us to drive Rabi flops quickly, and the superposition state mapping described below is not sensitive to the angle between the quantization and cavity axes.

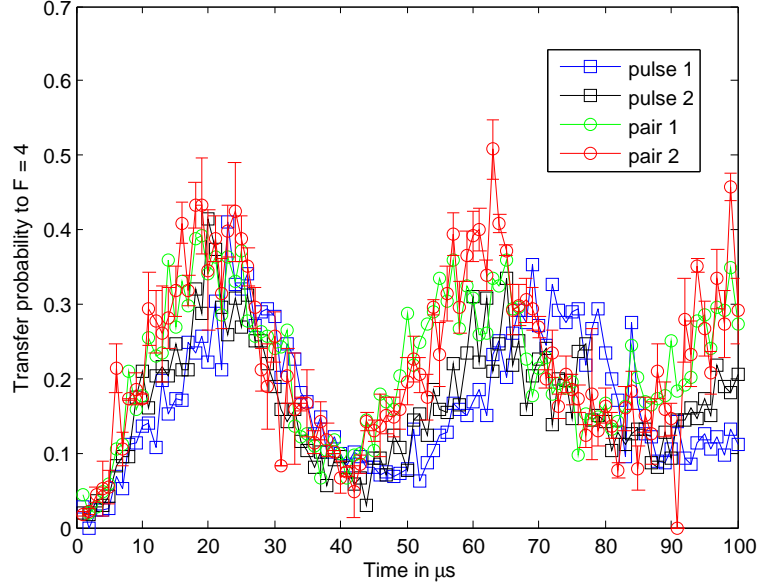


Figure 5.9: Individual and paired Rabi flops on the  $|3,0\rangle \rightarrow |4,\pm 1\rangle$  transitions. We drive atoms prepared in  $|3,0\rangle$  at the  $\Delta m = +1$  and  $-1$  transition frequencies for a variable time  $t$ , followed by state detection ( $\square$ , blue and black). We then apply both frequencies simultaneously ( $\circ$ , green and red), where for testing purposes, the two pairs use different signal generators for the  $|3,0\rangle \rightarrow |4,1\rangle$  transition. Note the increase in Rabi frequency by approximately  $\sqrt{2}$  for the paired flops.

one we intend to create via decay from  $|5',0\rangle$ .) A second pair of  $\pi$  pulses attempts to map the superposition back to  $|3,0\rangle$ . Here we vary the phase of the  $|3,0\rangle \rightarrow |4,1\rangle$  arm while holding the phase of the other arm constant; we expect the mapping processes in the two arms to interfere constructively or destructively as a function of phase. The result, shown in Figure 5.10, is a fringe with  $\sim 75\%$  visibility. For comparison, we have also plotted the data from the same measurement sequence, but with the relative phase held constant.

The fringe visibility in Figure 5.10 is limited by our ability to prepare atoms in  $|3,0\rangle$  and to drive coherent Raman  $\pi$  pulses between Zeeman pairs. We have some evidence that the off-axis magnetic field (and subsequent mixing between Zeeman states) interferes with these processes; namely, repeating the experiment above in the presence of a pure transverse field produces a fringe with significantly improved contrast. However, the presence of an axial field is necessary for the correspondence between photon polarization and Zeeman state that is the basis for our entanglement

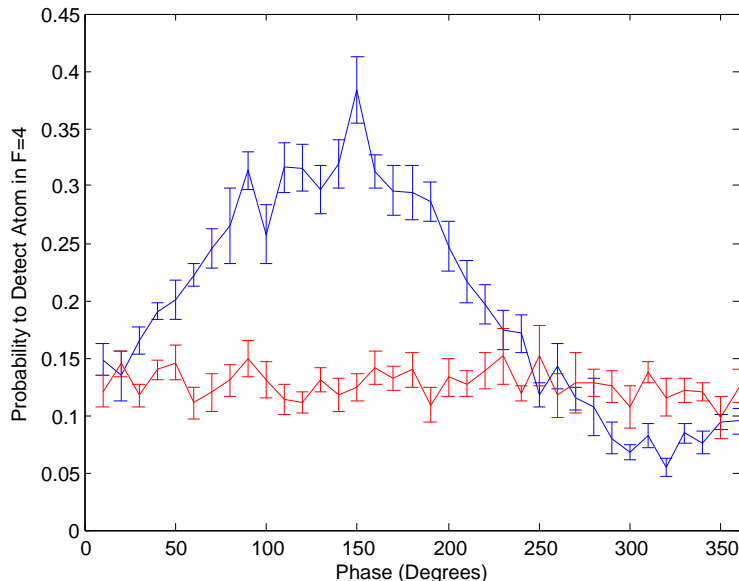


Figure 5.10: We prepare a superposition of Zeeman states  $|4, 1\rangle$  and  $|4, -1\rangle$ , then demonstrate a coherent mapping of this superposition to the hyperfine manifolds  $F = 3$  and  $F = 4$ . We apply simultaneous  $\pi$  pulses on the  $|3, 0\rangle \rightarrow |4, 1\rangle$  and  $|3, 0\rangle \rightarrow |4, -1\rangle$  transitions in order to transfer population to the  $F = 3$  manifold, followed by state detection. Shown is the probability to detect an atom in  $F = 4$  as a function of the relative phase between the two arms; for the red data, the experiment is repeated with the phase fixed at a random value. The data are plotted twice side by side to demonstrate the  $2\pi$  periodicity.

scheme.

### 5.3.4 Microwave transitions

A final possibility is to forego optical Raman processes and drive  $\Delta m = \pm 1$  transitions directly with microwaves at 9.2 GHz. By using microwaves, we avoid the problems resulting from spatial variation in Rabi frequency within each FORT well: the power from a microwave horn is constant across the  $\mu\text{m}$ -scale dimensions of the cavity, and every atom experiences the same Rabi frequency. (Atoms may still be shifted out of resonance with the microwaves as they move within the FORT, a result of the differential AC-Stark shift discussed in Section 5.2.)

While microwave horns are standard equipment in many atomic physics labs, they have not been used in our group prior to this experiment. An Agilent E8247C signal

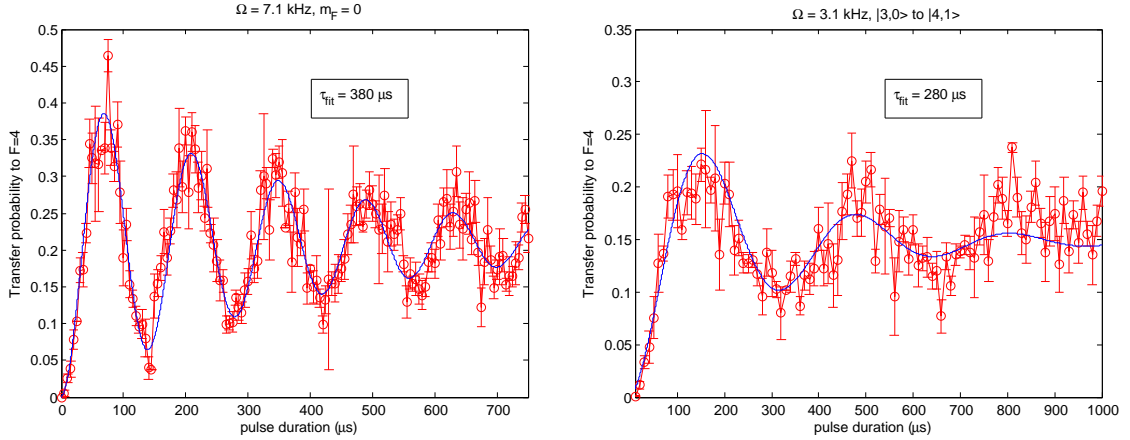


Figure 5.11: We drive microwave transitions directly between hyperfine ground states of cesium. Shown are Rabi flops on the  $|3,0\rangle \rightarrow |4,0\rangle$  and  $|3,0\rangle \rightarrow |4,1\rangle$  transitions.

generator provides us with a stable, RS-232-controlled microwave source. At the signal generator output is a microwave switch, followed by an amplifier. Between the amplifier and the microwave horn facing our cavity, we use a three-port circulator and a stub tuner in order to impedance-match the signal: we monitor the power in the reflected port of the circulator and adjust the stub tuner length to minimize this value. The stub tuner was a helpful recommendation from Sabrina Leslie in the Stamper-Kurn group at Berkeley, who also suggested the use of Huber-Suhner cables to minimize signal loss.

Using the microwave horn, we have observed Rabi flops on the  $|3,0\rangle \rightarrow |4,0\rangle$  and  $|3,0\rangle \rightarrow |4,1\rangle$  transitions (Figure 5.11). We now have a new means to drive coherent transitions between hyperfine ground states, allowing us to access both  $\Delta m = 0$  and  $\Delta m = \pm 1$  transitions while avoiding the problems of a bias field at an angle to the quantization axis (Section 5.3.3). The challenge of driving microwave transitions in our experiment stems from the available power. The Rabi frequencies in Figure 5.11 are only 7 kHz, limited at present by the 3 W amplifier in the signal path. We do have a second, 20 W amplifier, but we would like to test cavity heating effects at this power before putting it to use. However, since the Rabi frequency only scales as the square root of power, we expect less than a factor of three improvement from this amplifier.

A narrow Rabi frequency means that the experiment is highly sensitive to shifts in detuning, whether as a result of motion in the FORT potential or changing magnetic fields. Moreover, the corresponding long  $\pi$  pulse times ( $\sim 100\mu\text{s}$ ) place strict limits on acceptable decoherence rates. We have only recently begun to explore microwaves in a cavity QED setting, and there are certainly exciting applications ahead, but there are important issues that we will need to address in the process.

## 5.4 Fast pulses from the side of the cavity

We now have the means to map a Zeeman superposition onto a hyperfine superposition that we can measure. Here we return to the initial step in our entanglement protocol: using fast optical pulses from the side of the cavity to generate the Zeeman superposition along with a polarization-entangled photon. We discuss the implementation of these pulses in the lab and present correlation measurements between photon polarization and Zeeman state.

As in Figure 5.1, we would like to excite each atom from  $|4, 0\rangle$  to  $|5', 0\rangle$ . We need to drive this transition with linearly polarized light along the cavity axis, so the pulse must come from the side of the cavity. From  $|5', 0\rangle$ , the atom will decay into the cavity mode via a  $\sigma^+$  or  $\sigma^-$  photon, and the photon polarization will be entangled with the atom's final ground state. Ideally, to prepare the atom in  $F' = 5$  after each pulse, the pulse length should be short with respect to  $(2\gamma)^{-1} = 31$  ns and  $2\pi(2g)^{-1} = 14.7$  ns. In practice, we are able to make pulses as short as 10 ns. Here we use  $F = 4 \rightarrow F' = 5$  light from our master (probe) laser that is fiber-coupled into an amplitude modulator from EOSPACE Inc., a two-port Mach-Zehnder interferometer with a nominal 10 GHz bandwidth. We drive pulses with TTL signals to the modulator; additionally, we provide the modulator with a stable DC voltage  $V_\pi$ , which we adjust so as to maximize transmission when the TTL value is high. The measured suppression of the modulator is only 20 dB, so we enclose the fast modulator pulse within a slower AOM pulse applied to the light before the fiber input. Both pulses are driven from an SRS DG535 pulse generator triggered by the ADwin system. We use a Thorlabs

PDA10A 150 MHz detector to characterize the pulse shape at the cavity input.

We can make an estimate of the efficiency with which we expect these fast pulses to generate photons in the cavity mode. We first prepare atoms in  $|3, 0\rangle$  with optical pumping efficiency  $p_{pump}$ , where we have measured  $p_{pump} \approx 0.6$ . We then drive a  $\pi$  pulse from  $|3, 0\rangle \rightarrow |4, 0\rangle$ , where we estimate  $p_\pi \approx 0.8$  based on Rabi flopping data. After attempting to prepare the atom in  $|4, 0\rangle$ , we apply a single pulse from the side of the cavity on the  $|4, 0\rangle \rightarrow |5', 0\rangle$  transition. The pulse cycles population rapidly between the ground and excited states of the atom, so that the probability for the atom to be in  $|5', 0\rangle$  at the end of the pulse is  $p_{excite} = 0.5$ . Meanwhile, an atom in  $|5', 0\rangle$  will decay with probability  $p_{decay} = 0.59$  into the cavity mode and the rest of the time into free space.<sup>2</sup> We thus expect

$$p_{photon} = p_{pump} \times p_\pi \times p_{excite} \times p_{decay} \quad (5.8)$$

$$= 0.6 \times 0.8 \times 0.5 \times 0.59 \quad (5.9)$$

$$= 0.14. \quad (5.10)$$

In order to estimate the rate of photon detection at our SPCMs, we need to include the measured path efficiency  $p_{path} = 0.024$  [16];  $p_{photon} \times p_{path} = 0.0034$ . This is in reasonable agreement with the photon detection rate of 0.0046 that we have measured in the lab.

Our next step was to measure correlations between the detection of a cavity photon and the final Zeeman state of an atom. After the sequence above (state preparation,  $\pi$  pulse from  $|3, 0\rangle \rightarrow |4, 0\rangle$ , fast pulse from the side), we introduced a state-detection measurement, preceded by either zero, one, or two Zeeman-specific  $\pi$  pulses. In the absence of any  $\pi$  pulses, state detection conditioned on the detection of a cavity

---

<sup>2</sup>A simple way to understand this is to remember that the atomic excited state is a superposition of the two atom-cavity eigenstates. The system will thus oscillate at rate  $2g$  between having one excitation in the atom and one excitation in the cavity. When the excitation is in the atom, decay is possible at rate  $\gamma$  into free space (as the cavity mode subtends only a small fraction of the  $4\pi$  solid angle); when the excitation is in the cavity, decay takes place at rate  $\kappa$  into the cavity output mode. Assuming that  $g \gg \kappa, \gamma$ , the atom spends about half the time in each state, and the probabilities for decay via the atom and cavity channels are  $\frac{\gamma}{\kappa+\gamma}$  and  $\frac{\kappa}{\kappa+\gamma}$ , respectively.

output photon should confirm that the atom is in  $F = 4$ , since the only decay channel from  $F' = 5$  is to  $F = 4$ . Of course, we expect atoms not only to be in  $F = 4$ , but more specifically, to be in one of the two Zeeman levels  $|4, 1\rangle$  and  $|4, -1\rangle$ . We can evaluate the population in a given Zeeman level by selectively depopulating that level with a  $\pi$  pulse before the state detection process. For example, if we insert a  $\pi$  pulse from  $|4, 0\rangle \rightarrow |3, 0\rangle$  before state detection, we still expect to find all atoms in  $F = 4$  afterwards (conditioned on a photon), since we do not expect decay into the cavity mode from  $F' = 5$  to  $|4, 0\rangle$ . In contrast, we expect that a  $\pi$  pulse from  $|4, 1\rangle \rightarrow |3, 1\rangle$  or  $|4, -1\rangle \rightarrow |3, -1\rangle$  would reduce the probability to detect population in  $F = 4$  by half.

Note that the uncorrelated data in this experiment is also a source of interesting information. In the absence of  $\pi$  pulses, the unconditional probability to detect a photon in  $F = 4$  reflects our ability to prepare an atom in  $|4, 0\rangle$ . (Here we assume that every atom not optically pumped to  $|3, 0\rangle$  is prepared in another Zeeman state of the  $F = 3$  manifold, and that our  $\pi$  pulse only addresses the  $|3, 0\rangle$  state.) Moreover, the unconditional  $\pi$  pulse data tells us about the atomic decay into both the cavity mode and free space. Recall that while we expect the atom to decay via the cavity mode 59% of the time (into  $|4, 1\rangle$  and  $|4, -1\rangle$ , with equal probability), it also decays 41% of the time into free space, where the branching ratios of the cesium transitions determine the final Zeeman states. Specifically, in the case of free space decay, we expect the atom to decay to  $|4, 0\rangle$  with probability  $p_{fs0} = 0.55$  and to  $|4, 1\rangle$  and  $|4, -1\rangle$  with probabilities  $p_{fs1} = p_{fs-1} = 0.22$ . In the uncorrelated case, we also need to remember that the atom is left unexcited in  $|4, 0\rangle$  after half of all pulses. When we include this fact and weight the Zeeman state probabilities of the two decay channels, we find the expected probabilities

$$p_1 = p_{-1} = 0.5(0.41 \times 0.22 + 0.59 \times 0.5) = 0.19; \quad (5.11)$$

$$p_0 = 0.5 + 0.5(0.41 \times 0.55) = 0.61. \quad (5.12)$$

A more thorough calculation also takes into account the imperfect nature of our state

$\pi$ pulse(s)	$P_4$ , unconditional	$P_4$ , conditional
none	0.62	0.92
$ 4, 0\rangle \rightarrow  3, 0\rangle$	0.33	0.84
$ 4, 1\rangle \rightarrow  3, 1\rangle$	0.57	0.70
$ 4, -1\rangle \rightarrow  3, -1\rangle$	0.56	0.62
$ 4, 1\rangle \rightarrow  3, 1\rangle$ and $ 4, -1\rangle \rightarrow  3, -1\rangle$	0.53	0.35

Table 5.1: Measured correlations between a detected cavity photon and the Zeeman state of a trapped atom. We attempt to prepare each atom in  $|4, 0\rangle$  and excite it to  $|5', 0\rangle$  with a short pulse from the side of the cavity. We then measure the probability  $P_4$  that the atom is in  $F = 4$  following zero, one, or two Zeeman-specific  $\pi$  pulses; this is expressed both as an unconditional probability and conditioned on the detection of a photon in the cavity output path.

preparation and  $\pi$  pulses; in this case, we have

$$p'_1 = p'_{-1} = p_{pump} \times p_\pi \times 0.5(0.41 \times 0.22 + 0.59 \times 0.5) - 0.1 \times p_\pi = 0.01, \quad (5.13)$$

$$p'_0 = 0.8 \times (0.5 + 0.5(0.41 \times 0.55)) - 0.1 \times p_\pi = 0.21, \quad (5.14)$$

where the additional term reflects the fact that atomic population left in  $F = 3$  after the initial  $\pi$  pulse (roughly 10% for each of the three Zeeman manifolds) can be brought into the  $F = 4$  manifold by the second, diagnostic pulse.

The results of our measurements are summarized in Table 5.1. After state preparation and excitation to  $|5', 0\rangle$ , the unconditional probability to find an atom in the  $F = 4$  manifold is 0.62, somewhat better than our optical pumping and  $\pi$  pulse estimates, and the conditional probability is 0.92. The fact that this value is not 1 can be interpreted as the result of background photon counts that occur during the 38% of all trials when the atom is not successfully prepared in  $F = 4$ .

Following a  $\pi$  pulse from  $|4, 0\rangle \rightarrow |3, 0\rangle$ , the unconditional probability to detect an atom drops to 0.33 and the conditional probability to 0.84. From  $p'_0$  and the probability to find an atom in  $F = 4$ , we would anticipate the unconditional probability to be  $0.62 - 0.21 = 0.41$ . The conditional probability can again be understood in terms of background photon counts: as the unconditional probability to find an atom in  $F = 3$  is two times greater than without the  $\pi$  pulse, the chance that background

counts (interpreted as cavity photons) will coincide with an atom in  $F = 3$  is also two times greater, and the conditional  $F = 3$  probability doubles from 0.08 to 0.16.

The unconditional probabilities following  $\pi$  pulses from  $|4, 1\rangle \rightarrow |3, 1\rangle$  and  $|4, -1\rangle \rightarrow |3, -1\rangle$  are 0.57 and 0.56, respectively. In comparison, we would expect values of  $0.62 - p'_1 = 0.61$  in both cases. (Again, the discrepancy suggests that for this data run, our optical pumping efficiency was better than usual.) The conditional probabilities measured are 0.62 and 0.70. We would expect to measure roughly

$$p_{c1} = p_{c-1} = 0.90 \times (1 - 0.5 \times 0.8 + 0.1 \times 0.8) = 0.61, \quad (5.15)$$

where the second term expresses the depopulation of the Zeeman level (to which the atom has decayed with probability 0.5) by an imperfect  $\pi$  pulse, the third term is the probability that population in  $|3, 1\rangle$  or  $|3, -1\rangle$  will be excited to  $F = 4$  by this  $\pi$  pulse, and the overall scaling reflects background photon counts as above. Thus, we find good agreement between the data and our model; we do not yet have a good explanation for the asymmetry in the two conditional probabilities, but it may be connected with the cavity birefringence.

Finally, we apply a pair of  $\pi$  pulses on both  $|4, \pm 1\rangle \rightarrow |3, \pm 1\rangle$  in sequence before state detection; in this case, we find unconditional and conditional probabilities of 0.53 and 0.35. Here we expect an unconditional value of  $0.62 - 2 \times p'_1 = 0.60$  and a conditional value of

$$p_{c\pm 1} = 0.90 \times (1 - 2(0.5 \times 0.8 + 0.1 \times 0.8)) = 0.32, \quad (5.16)$$

again consistent with the data.

We have thus observed correlations between photons generated via fast pulses from the side of the cavity and atoms prepared in  $|4, \pm 1\rangle$ . In the near future, we hope to combine these correlation measurements with the hyperfine mapping of Section 5.3. After applying a fast pulse from the side of the cavity at  $t = 0$ , we would attempt to transfer the Zeeman populations in  $|4, \pm 1\rangle$  to  $F = 3$ , followed by state

detection. Conditioned on the detection of a photon at the cavity output, we expect that the hyperfine population measurement would result in a fringe as a function of  $t$ , due to precession of the Zeeman superposition state. We could then consider the long-anticipated rebuild of our cavity output path: while we are now only able to detect one photon output polarization, the ability to detect orthogonal polarizations in parallel would permit a Bell measurement of atom and photon states.

## Chapter 6

# A new generation of cavities

For several years, the workhorse of cavity QED experiments in our research group has been the optical cavity in lab 11. This cavity was built in 1999 and since then has remained in an unbroken ultra-high vacuum (UHV) environment, an exceptional stroke of good luck and a testament to the remarkable experimental skill of David Vernooy and Jun Ye. More recent cavity-building efforts in our group have had multiple goals: to construct cavities with different characteristics than those of the lab 11 resonator, e.g. shorter or asymmetric; to improve upon the design and assembly procedure for the cavity and vacuum chamber system; and to keep knowledge about the process of cavity building — something of a black art — alive in our group.

In this chapter, I discuss our group's two most recent cavity projects. While the lab 1 feedback project never produced any publishable experimental results, we learned a great deal in our effort to get it running; this information has not been detailed elsewhere and should be of use in the design of new experiments. Meanwhile, the future of the asymmetric cavity project is still an open question. In the second part of the chapter, I summarize progress to date in this most recent endeavor and attempt to highlight outstanding questions and challenges.

### 6.1 Active feedback to atomic motion

Chapter 6 of Theresa Lynn's thesis provides thorough documentation about the design of the feedback experiment [22], so I will only touch on this briefly before discussing

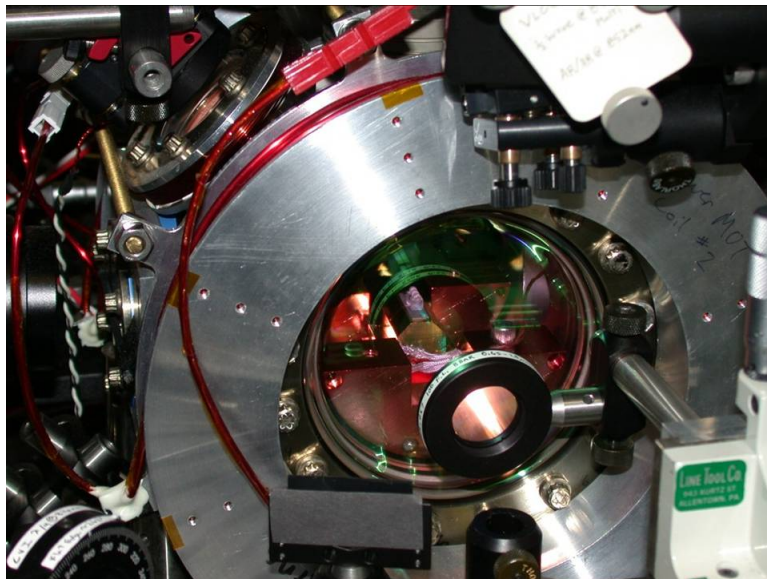


Figure 6.1: The lab 1 cavity inside the lower vacuum chamber

its implementation. In 2000, Theresa and Kevin Birnbaum began to assemble a two-chamber UHV system similar to the one already in place in lab 11. The Ti:sapphire laser previously used both for probing and locking the cavity was replaced with diode lasers at 852 nm (probe) and 815 nm (lock), both stabilized to the cesium  $D2$  line via an external reference cavity. The physics cavity inside the new vacuum chamber was the first one ever built to a specifically chosen length (in this case,  $9.2 \mu\text{m}$ ), and special care was taken to select the cavity mount materials in order to minimize birefringence. Another important reference for experiment design is Appendix B of Kevin Birnbaum's thesis, a collection of information about vacuum systems compiled during the construction of the new chamber [4]. A separate, unpublished set of notes by Kevin describes the cavity-building procedure used in December 2001. (Yat Shan Au's undergraduate thesis includes the most recent updates to this procedure [105].)

### 6.1.1 Characterizing the active-feedback cavity

In June 2002, when I joined Kevin, Theresa, and Dominik Schrader in lab 1, the new cavity had already been placed inside the lower vacuum chamber, which had just been pumped down to  $10^{-10}$  torr. We worked through the summer on optimizing the

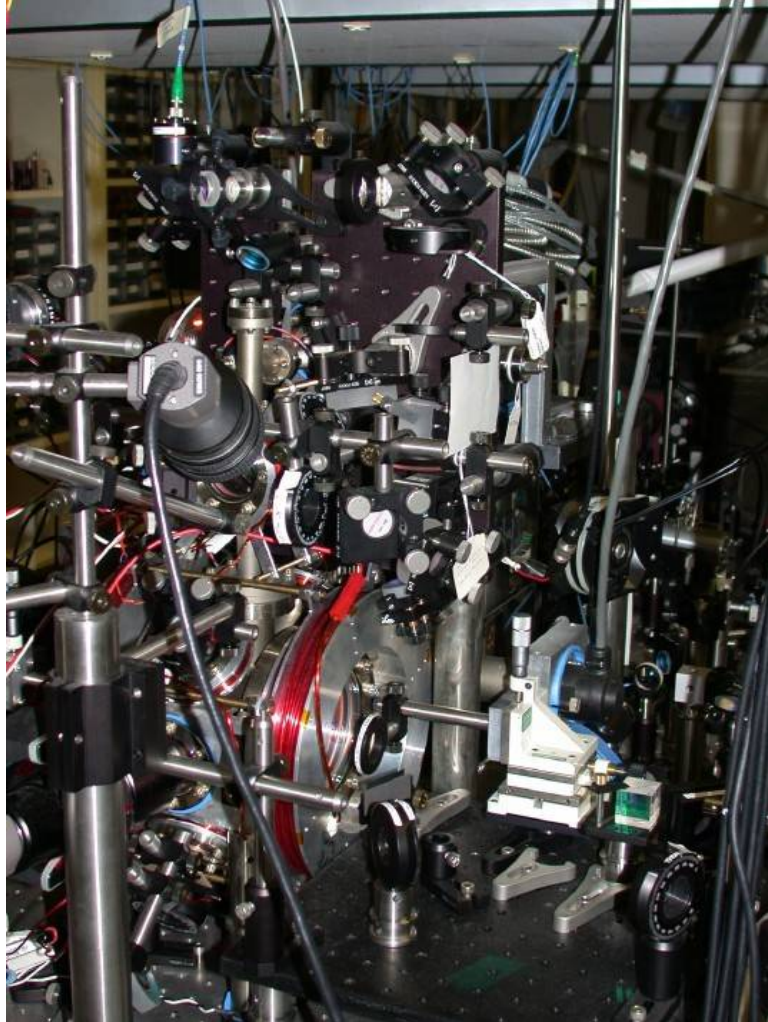


Figure 6.2: The lower and upper vacuum chamber of the lab 1 experiment, surrounded by associated optics

MOTs in the upper and lower chambers and on positioning the lower MOT above the mirrors so that atoms would fall through the cavity. As we began to implement active stabilization of the cavity length, we discovered that the cavity mount had been inadvertently plated with nickel, a ferromagnet, when it had been sent out for gold plating. Each time we switched on or off the magnetic fields used for trapping atoms, the cavity length jumped by roughly  $4 \text{ \AA}$ . In order to compensate for these jumps, we built a feed-forward input to our cavity length servo which anticipated the magnetic field switching. With the new servo in place, locking the cavity in transmission to the probe laser field, we observed our first atom transits in October 2002.

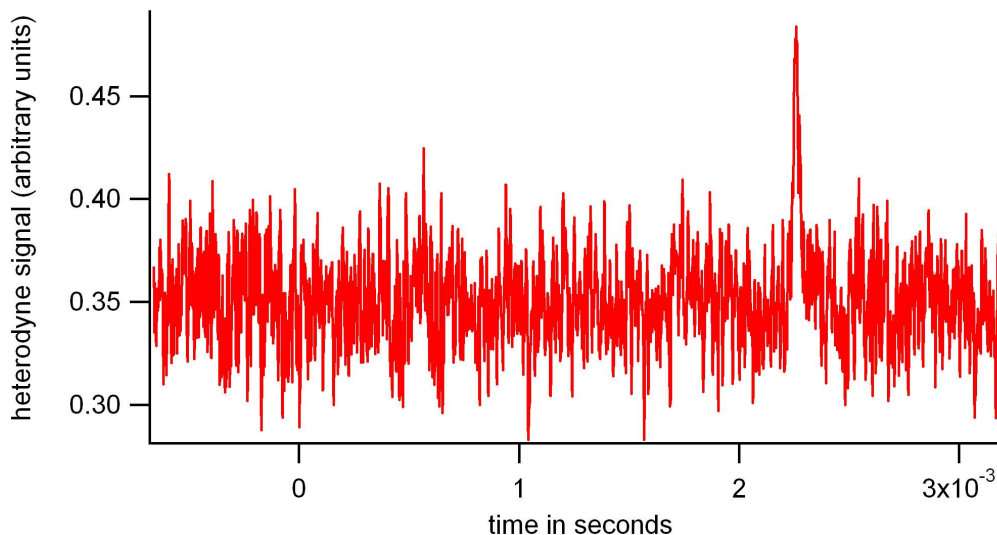


Figure 6.3: A sample “upgoer” atom transit observed in lab 1 via heterodyne detection. Here the probe laser is tuned red of the atom and cavity resonance such that  $\omega_p = g = -130$  MHz. The transit is observed about 23 ms after release of the atom cloud and has width  $\sim 50$   $\mu$ s.

Much of the following year was spent assembling the frequency metrology setup, analogous to the one used in lab 11. This rather complicated stabilization chain required us to lock our probe laser to a reference cavity, then lock the reference cavity to the cesium  $D2$  line, lock our locking laser to the reference cavity, and finally lock our physics cavity to a frequency sideband of the locking laser. It was June of 2003 before we could accomplish all of these steps simultaneously and several more months before we could do this reliably.

Once we had observed transits, both “downgoers” and “upgoers,” while locking to the 815 nm sideband, our next projects were to improve their frequency and to characterize them. Kevin and I were not particularly successful in this first task, despite our repeated efforts to optimize the size, position, and temperature of the MOT, and even to tilt the optical table. Subsequently, Kevin wrote a simulation to estimate the number of atom transits per MOT drop as a function of cavity angle, included as section 7.9 of Ref. [4]. He found that the angular dependence of transit probability was fairly weak: a tilt of  $4^\circ$  from horizontal was necessary to reduce the number of observed transits by half. (It is interesting to note that in another cavity

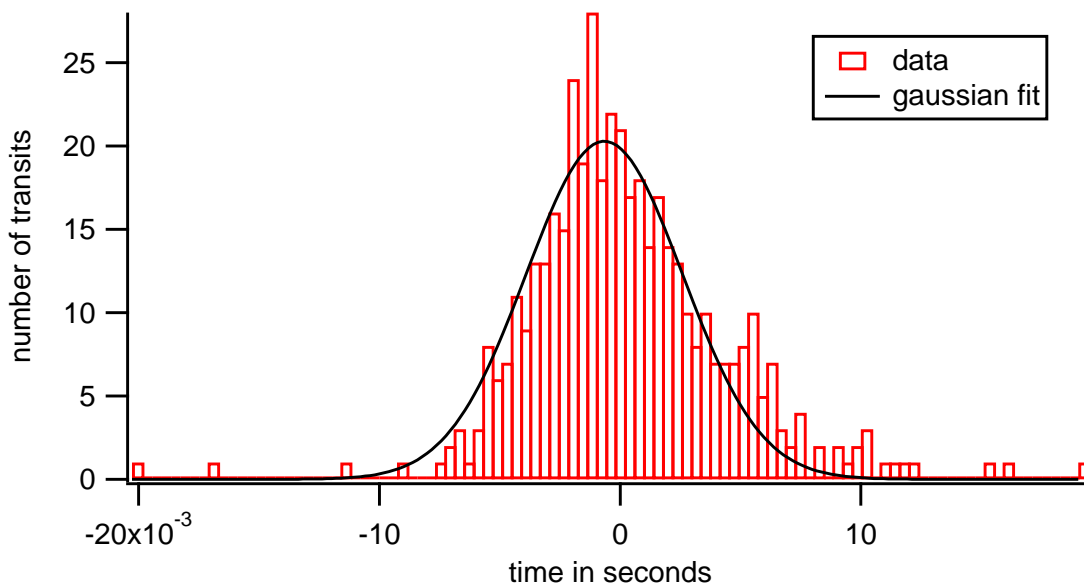


Figure 6.4: Histogram of 442 recorded transit arrival times. The trigger at time  $t = 0$  occurs 25 ms after the atoms are released from polarization-gradient cooling.

QED experiment, tilting the optical table has in fact been used to optimize the atom count rate through the cavity [106].)

One step in characterizing the transits was to assemble a histogram of transit arrival times, based on 442 transit files recorded over 7 hours in November 2003. This data is shown in Figure 6.4, where the transit arrival times are referenced to an external trigger from the LabView control program, 25 ms after the end of polarization-gradient cooling. A Gaussian fit to the data gives a mean arrival time of  $-0.8$  ms and a distribution half-width at half-maximum (HWHM) of 4.6 ms. Note, however, that the Gaussian fit is not entirely satisfactory: it overestimates the number of atoms arriving early and underestimates those arriving late.

To investigate the observed distribution — both its asymmetry and its implications for the temperature of the atom cloud — we returned to Kevin’s transit simulation program. The program takes input variables which include the standard deviations of initial x and y positions ( $\sigma_x, \sigma_y$ ) and velocities ( $v_x, v_y$ ) of atoms in the MOT as well as the height of the MOT above the cavity ( $\langle y \rangle$ ). It then samples atoms from this distribution and records the arrival time of each atom within the cavity. (This is

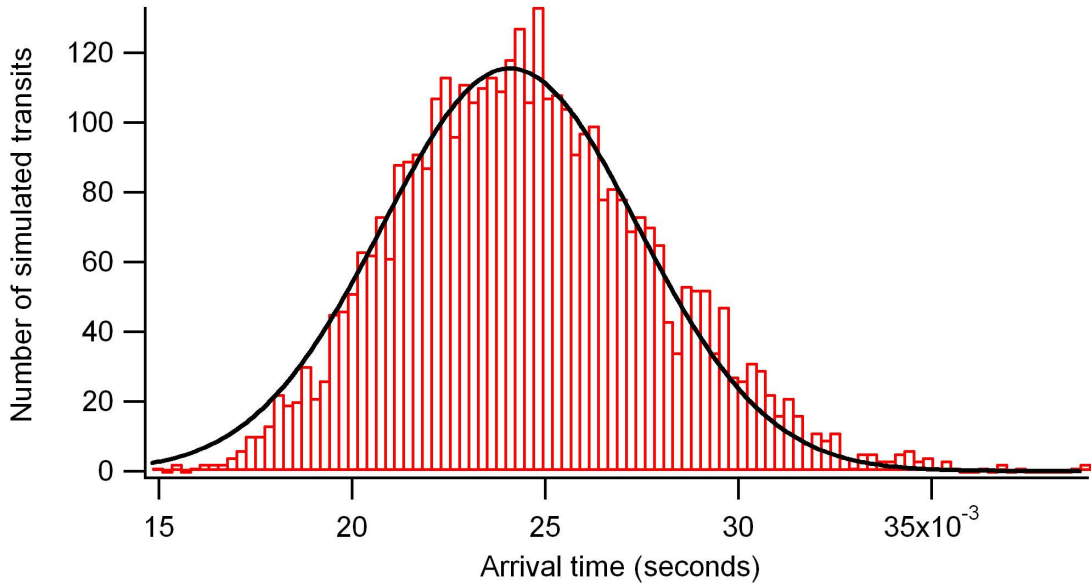


Figure 6.5: Simulated distribution of transit arrival times. Atoms are released at  $t = 0$  from a cloud above the cavity. The height and size of the cloud are determined from images of the MOT, while the initial velocities of the atoms are adjusted for good agreement with the data.

simply a calculation of moving particles under gravity, constrained by the mirror geometry, and does not take into account any light forces on the atoms.) We determined  $\sigma_x$ ,  $\sigma_y$ , and  $\langle y \rangle$  independently from calibrated frame-grabber images of our MOT. We then adjusted input parameters  $v_x$  and  $v_y$ , assuming them to be equal, in order to obtain good agreement with the measured distribution width. Figure 6.5 shows a simulated histogram with  $\sigma_x = \sigma_y = 0.174$  mm,  $\langle y \rangle = 2.9$  mm above the center of the cavity, and  $v_x = v_y = 3.13$  cm/s, for a distribution HWHM of 4.7 ms. From these velocities, we were able to infer a lower MOT temperature of  $16 \mu\text{K}$ , consistent with effective polarization gradient cooling. Moreover, it is interesting that the simulation reproduces our experimental asymmetry, with more atoms piled up at the slow tail.

We also wanted to understand the observed time for an atom to transit the cavity, which was faster than we had initially expected. For example, in November 2003, we measured transits with full-width at half-maximum (FWHM) between 20 and 36  $\mu\text{s}$ , corresponding to a velocity of 0.6 – 1 m/s across the cavity mode. However, an atom falling from rest 3 mm above the cavity (the measured location of the MOT)

would only have  $v = 0.25$  m/s. The answer was that this classical picture neglects the trapping force provided by the atom-cavity coupling  $g$ , which in fact accelerates the atoms as they approach the center of the mode. A calculation using the cavity parameters  $\omega_{atom} = 0, \omega_{cavity} = 0, \omega_{probe} = -130$  MHz,  $g_0 = 130$  MHz,  $\kappa = 17$  MHz, and empty cavity photon number  $\langle a \rangle = 1$  found that an atom falling 3 mm would cross an antinode of the cavity mode with  $t_{FWHM} = 29$   $\mu$ s. As it turns out, there is only a very weak relationship between the initial height of an atom and its transit time, which is almost entirely determined by  $g$ . For example, an atom falling from 2 cm would have a transit time  $t_{FWHM} = 22$   $\mu$ s; for an atom with no initial fall velocity,  $t_{FWHM} = 31$   $\mu$ s. An apparent discrepancy with the 74  $\mu$ s average transit time reported in Ref. [20] was resolved when Theresa explained that their criterion had been the amount of time that atoms were within one mode waist of the cavity center, rather than the FWHM.

A third transit measurement looked at the difference between peak and empty cavity transmission for “upgoers” as a function of probe intensity (Figure 6.6). The results were roughly consistent with a Matlab calculation using the quantum optics toolbox and thus confirmed that our heterodyne calibration (which we used to scale cavity transmission to photon number) was about right.

Finally, we were concerned about the polarization of the intracavity light in connection with observations that a repump beam from  $F = 3$  to  $F' = 4$  improved the frequency of transits. (We intended to drive the cavity with circularly polarized light on the closed  $F = 4 \rightarrow F' = 5$  transition. The fact that atoms were present in the  $F = 3$  manifold seemed to suggest the presence of linearly polarized light, though we later concluded that the repump beam probably just helped us see atoms that were in  $F = 3$  as they entered the cavity.) After reworking the cavity input path so that the last optical elements were a polarizing beamsplitter cube (PBS) optimized for 850 nm and a zero-order quarter waveplate at 850 nm, we determined that only 0.003% of the input light had the wrong circular polarization. In December 2003, we measured  $\kappa_1 = 14.4 \pm 0.6$  MHz along one birefringent axis of the cavity and  $\kappa_2 = 17.0 \pm 0.8$  MHz along the other, where the difference in the center frequency between the two

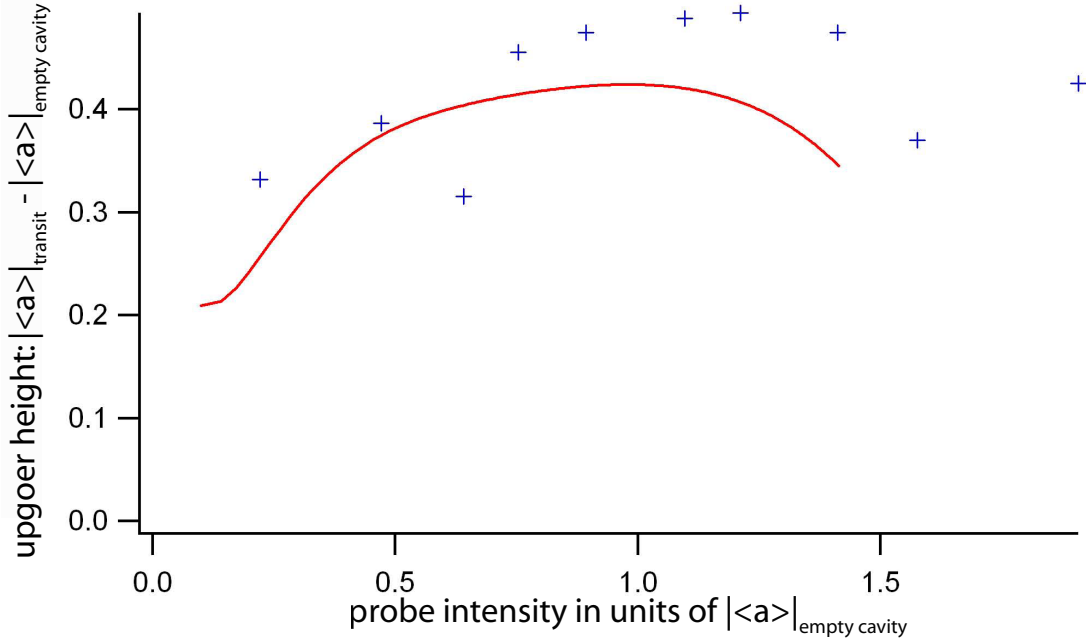


Figure 6.6: Upgoer height as a function of probe intensity, expressed in units of  $|\langle a \rangle|$  (proportional to the square root of the heterodyne detection signal) for comparison with a Matlab quantum optics toolbox calculation (red). As the empty cavity value of  $|\langle a \rangle|$  also increases with probe intensity, this is subtracted from each data point.

resonances (i.e., the birefringent splitting) was  $\Delta\nu = 4$  MHz. Thus  $\frac{\Delta\nu}{\kappa} \approx 0.25$ , in contrast with  $\frac{\Delta\nu}{\kappa} \approx 1$  for the lab 11 cavity [29]. As  $\frac{\Delta\nu}{\kappa}$  is proportional to the birefringent phase shift per round trip, we can conclude that the efforts made by Theresa and Kevin in constructing the new cavity had succeeded in reducing birefringence effects by a factor of four.

In the spring of 2004, we assembled a diode laser at 936.8 nm, two cavity free spectral ranges red of the cesium resonance, with the intention of trapping atoms within an intracavity FORT. Because of the narrow gap between the cavity mirrors, we would not be able to focus lattice beams through the cavity from the side in order to cool and load atoms into the trap. However, with an EOM providing frequency sidebands for locking the laser to the physics cavity and an AOM for switching the trap, we planned to trigger the FORT on in the presence of an atom, as had been done in the early days of lab 11 [40]. The FORT linewidth and other cavity parameters are listed in Table 6.1.

lab 1 cavity parameter	value
effective length $l$	9.2 $\mu\text{m}$
mode waist $w_0$	13.3 $\mu\text{m}$
$\kappa_1, \kappa_2$	$2\pi \times (14.4 \text{ MHz}, 17 \text{ MHz})$
finesse	570,000 (along axis 1)
$g_0$	$2\pi \times 130 \text{ MHz}$
$\kappa_{815\text{nm}}$	31.2 MHz
$\kappa_{936\text{nm}}$	4.9 GHz

Table 6.1: Parameters for the lab 1 active-feedback cavity. All parameters are for 852 nm unless otherwise stated.

## 6.1.2 Difficulties in implementation

We encountered a number of difficulties which slowed our progress on the active-feedback experiment and would have made data acquisition a challenge. Here I highlight what seem in retrospect to have been the most significant of these problems and suggest how they might be avoided in future experiments.

### 6.1.2.1 A nickel-plated cavity mount

The nickel-plated cavity mount described in Section 6.1.1 has received a great deal of blame. The copper mount was gold-plated through the machine shop in order to prevent oxidation during cavity assembly, after which it could no longer be baked. Unknown to us, nickel is generally used as an underplate in this process to avoid gold diffusion into the copper, and we should have specifically requested its omission. While it was frustrating to learn that magnetic material had found its way into the vacuum chamber, in practice we were able fairly quickly to devise a feed-forward locking circuit that compensated for the cavity stabilization difficulties caused by induced fields. Although the cavity length jumped each time the current in the MOT coils switched, a signal sent to the locking circuit provided a synchronous offset voltage to the cavity piezo.

However, this adaptation made the locking circuit inherently less stable. In addition, the induced magnetization in the nickel would make it challenging to implement controlled transverse and axial bias fields in future experiments. This sort of con-

trol over the magnetic field seen by atoms trapped in the cavity has emerged as an important tool in lab 11.

### 6.1.2.2 Complexity of the stabilization network

The network of lasers and servos required for the experiment to run was fairly complex. The MOT trapping and repump lasers had to be locked separately to cesium lines. The cavity probe laser and 815 nm locking laser were each locked to a 30 cm, 50 kHz reference cavity, and the reference cavity was then locked to cesium. A traveling wave modulator was used to put frequency sidebands (tunable up to 1 GHz) on the locking laser, and the physics cavity length was then stabilized by locking to one of these sidebands. Later, the 936 nm FORT laser was also locked to the physics cavity. All of these locks used the Pound-Drever-Hall technique, and all five lasers were home-built external-cavity diode lasers.

This complexity was to some extent inevitable, but it meant that we spent a great deal of time just trying to keep everything locked simultaneously, and the instability of the cavity lock due to the feed-forward circuit described above only made things worse. We learned to avoid unwanted amplitude modulation (which causes DC offset drift in an error signal) by using EOMs to put frequency sidebands on the laser light instead of modulating the laser current; in addition, it was helpful to put a PBS cube before each EOM for a clean input polarization. At first, we locked the physics cavity in reflection but then switched to locking in transmission, which allowed us to avoid noise on the reflected signal.

In this situation, we could have learned from lab 11, where Andreea Boca implemented a robust injection-locked laser setup for the MOT trapping laser [29]. By replacing the grating-stabilized  $F = 4 \rightarrow F = 5$  laser with a slave laser seeded by injection light from the cavity probe, we could have eliminated one cesium lock from our system. We could also then have bypassed our SDL tapered amplifier, which came with its own alignment headaches, since an injection-locked laser can provide a few hundred mW of power. (Using a grating to form an external cavity reduces the laser output power by roughly half, since the rest of the power is fed back into the

diode.) More recently in lab 11, we replaced the cesium lock for the  $F = 3$  repump laser with a phase lock to the probe laser, as described in Chapter 3. This was done for the purposes of having phase-stable  $F = 3$  and  $F = 4$  lasers for the coherent state transfer experiment; however, we have found as a side benefit that the lock has been much more robust.

### 6.1.2.3 A dearth of transits

This final problem is perhaps the most fundamental: we simply never saw very many atoms in our cavity. During successful data runs, it was more likely to see no transits than one transit in a four-second experimental cycle, and it was uncommon to see more than one transit per cycle. When lasers drifted out of alignment, or the MOTs were not well positioned, it was difficult to see any transits at all.

Perhaps this should have been more cause for concern beforehand, given the short length of the cavity: Theresa notes in her thesis that on average 40 transits per cycle were observed in lab 11, and that the flux of atoms through the lab 1 cavity was expected to be 60 times smaller than in lab 11. This had not been an issue in the previous atom-cavity microscope experiment, also based upon a  $\sim 10 \mu\text{m}$  cavity, because that experiment had used only one MOT, formed directly from cesium background vapor above the cavity. The cost of switching to a double-MOT design is a reduced atom number in the final MOT, by roughly a factor of 100.

The current focus in our group has been on cavities with enough space to admit lattice beams from the side as in lab 11, that is, at least  $30 \mu\text{m}$  in length. However, if there is future interest in a very short cavity with large  $g$ , I would recommend developing a new strategy for obtaining a large lower MOT. For example, one might incorporate a “pusher beam” into the upper MOT in order to create an “atom faucet” [107] that would load the lower MOT with a high-flux, low-divergence atomic beam.

### 6.1.3 Technical improvements

There are also some positive lessons to be drawn from the lab 1 experiment. The design of the two-chamber vacuum system offers much more physical and optical access than is available in lab 11. The technique of coupling both the trapping and repump beams for the MOT into polarization-maintaining optical fiber, then bringing them out of fiber in a compact setup close to the chamber, proved very successful. I would like to emphasize the usefulness of having a systematic procedure in place for MOT alignment, that is, the ability to center all three transmitted MOT beams by eye on their output windows and the use of irises for retro-reflection alignment.

Two optimization procedures for the MOT are worth mentioning. The first concerns the positioning of both the upper and lower MOTs, in the first case above the differential pumping tube, and in the second case above the cavity. The main MOT coils provide a gradient trapping field for the MOT, while three pairs of bias coils ensure that the magnetic field is nulled at the MOT location. If this condition is not met, then when the main coils are turned off for polarization-gradient cooling, the atoms will be pulled away from the center of the trapping beams by the residual fields and will not fall correctly into the second chamber or through the cavity mode. In order to optimize the currents through the bias coils, we used a Labview control program which, after forming a MOT, gradually stepped down the current through the main coils over the course of a few seconds. This allowed us enough time to observe the trajectory of the atom cloud on a camera as the MOT dissipated. We could then adjust the bias coil currents until the cloud expansion appeared uniform and symmetric.

The second procedure measured the temperature of the cesium cloud after cooling. In January 2004, as part of an effort to improve the frequency of transits, we decided to quantify the polarization-gradient cooling, which consisted of 35 ms of illumination from the trapping beams, at a lower intensity and increased detuning from their MOT settings and with the MOT coils off. We used the following method: after waiting a variable time delay  $t$  after the fields were turned off, we applied a detuned pulse of light

a few ms in length in order to illuminate the atom cloud. For each time  $t$ , we took a pair of pictures of the illuminated cloud with our camera frame-grabber. One picture of each pair was taken with the MOT coils always turned off (i.e., in the absence of atoms) and then subtracted from the other in order to remove background light from the chamber. After obtaining image pairs at a series of delay times, we analyzed the data in IgorPro: following the image subtraction, we took a line profile through the center of the remaining cloud, which we fit to a Gaussian. Plotting the Gaussian widths as a function of  $t$ , we fit the data to determine both the initial radius of the cloud and the expansion time constant  $\tau$ , from which we could extract a temperature. In practice, once we had improved the cooling by adjusting the intensity and detuning settings of the beams, it was no longer possible to measure a temperature accurately because the cloud fell under gravity out of the range of the camera before it had much chance to expand. In this case, we could make further improvements to the upper MOT settings by instead observing the number of atoms collected in the resulting lower MOT.

One interesting consequence of our difficulties in observing transits was that Kevin began to wonder if there was some underlying physics at work that we hadn't considered. He realized that in the case of such a small cavity, the atom-cavity coupling of  $2\pi \times 130$  MHz was on the order of the cesium hyperfine excited state splittings. This brought into question the assumption that we could model our system as a two-level atom interacting with a single cavity mode (the Jaynes-Cummings model [3]); even though our circularly polarized probe beam addressed a two-level cycling transition between  $F = 4$  and  $F = 5$ , the cavity could now couple to other hyperfine levels. Working with Scott Parkins, who was visiting from the University of Auckland, Kevin calculated the transmission as a function of probe and cavity detunings for a cavity coupled to multiple excited state levels, as well as to the entire  $D2$  transition [28, 5]. While our optical cavity was just on the border where these couplings become relevant, it may be possible to observe some of the phenomena predicted by his calculations in the microtoroid experiments currently underway in our group.

## 6.2 An asymmetric cavity system

In the fall of 2004, we abandoned work on the active feedback experiment and began instead to construct a new cavity. This next-generation cavity would address several shortcomings of the current lab 11 system. While we hoped that it could someday run in parallel with the lab 11 experiment, the system also had a practical function as a backup cavity for lab 11, which at that point had been running continuously for six years (now nine).

In particular, the new cavity would be “single-sided,” that is, built with one “open” mirror more transmissive than the other (“closed”) one, so that light escaping from the cavity would exit primarily through this open mirror. At a minimum, this design would allow us to collect roughly twice the intracavity photons as in lab 11, where photons exit from both cavity mirrors but are only collected at one port. We could also hope to realize protocols for quantum computation, such as a quantum nondemolition (QND) measurement of photon number [44]. (This protocol relies on a single-sided cavity because it requires a photon either to reflect off the cavity — acquiring a phase shift in the process — or to enter the cavity and then exit through the same mirror it entered.) The most ambitious vision was that with a second functioning optical cavity in our group, we might entangle the states of two atoms trapped simultaneously in both cavities [78].

Previous cavity-building efforts had attempted to minimize birefringent splitting in the cavity modes by avoiding any nonuniform stress to the mirrors. Techniques for achieving this included minimizing the use of epoxy which bonds the mirrors to their v-blocks, keeping the epoxy as far as possible from the mirror surfaces, selecting an epoxy with optimal thermal expansion properties, machining the v-blocks out of BK7 in order to match the thermal expansion coefficient of the mirror substrates, and not baking the vacuum chamber once the cavity was inside [21, 22]. As we have seen, in the active-feedback cavity, the result was a reduced but still measurable birefringence. We hoped in this case to explore stressing the cavity mirrors on purpose in order to induce a birefringent splitting. Ideally, we could then tune this stress, perhaps with a

piezoelectric transducer, either to (a) null it entirely, or (b) make it large enough (i.e.,  $\Delta\nu \gg g$ ) so that our intracavity atom would only interact with one cavity mode.

Finally, we were not sure what was limiting the recently demonstrated 2–3 s trap lifetimes in the lab 11 cavity, but a prime candidate was background collisions [102]. In the new vacuum chamber, we would aim for a background pressure of  $10^{-12}$  torr, two orders of magnitude lower than in previous experiments, in the hope that this would permit longer intracavity storage times. However, this new target pressure suggested that we would have to bake the vacuum chamber more aggressively than in the past. It would be necessary to reconsider how well the chamber components could withstand baking.

Kevin had meanwhile joined Andreea, David Boozer, and Russ Miller on the vacuum Rabi splitting experiment in lab 11. I took on the project of collaborating with mirror manufacturers to develop low-loss mirrors for our cavity, the subject of Chapter 7. Meanwhile, I worked with undergraduates Yat Shan Au and Travis Bannerman on vacuum chamber and cavity redesign; the project later grew to include Toby Burrows, Andrey Rodionov, and Dal Wilson.

### 6.2.1 Cavity redesign

At the heart of our cavity-QED experiments is a high-finesse Fabry-Perot resonator consisting of two mirrors fabricated on BK7 substrates. As described in more detail in Refs. [21, 22], in the most recent generation of cavities, the mirrors are attached with epoxy to BK7 v-blocks which have been glued on top of shear-mode piezoelectric transducers. Another layer of electrically conductive epoxy bonds the piezos to the cavity mount, a copper block.

This cavity design presented two problems in light of our plan to bake the vacuum chamber: the low Curie temperature ( $190^\circ\text{C}$ ) of the piezo material, EBL3, and the temperature ranges of Torr-Seal and Master Bond EP30LTE-ND, the epoxies used for bonding the v-blocks to the piezos and the mirrors to the v-blocks. After extensive research, Yat was able to suggest replacement materials. Pz23 and Pz27 from Ferrop-

erm Piezoceramics (Kvistgaard, Denmark) have relatively high Curie temperatures of 350 °C and a recommended maximum working temperature of 250–300 °C. For a UHV epoxy, Caburn MDC (West Sussex, U.K.) sells a product called H27DUHV which it claims is vacuum-compatible to  $10^{-11}$  torr and can be baked to 270 °C. Dal returned to the question of epoxy last year in the process of building several test cavities, where in addition to UHV compatibility and the coefficient of thermal expansion, he considered the importance of a good consistency and reasonable curing time for cavity-building. He has settled on Epotek H21D as a cheaper alternative to the Caburn product; in addition, its volatile organic outgassing specifications are well-documented. (After a cavity baking experiment in which the finesse dropped by a factor of two, we are now concerned about outgassing not only because of its effects on background pressure but also because it may deposit material on the mirror faces.) It is interesting to note that he has also successfully used thermo-compression to achieve a glue-free bond between two flat surfaces, for example, by clamping together a silver-evaporated piezo and a copper cavity mount for an hour at 150 °C.

Would the new high-temperature piezos allow us to tune the cavity length over a full free spectral range (426 nm of travel)? This is a difficult question to answer, as the shear mode piezos in both the previous lab 1 cavity and the current lab 11 cavity exhibit two to three times as much travel as one would expect [40, 22]. Here the relevant quantity is the shear displacement  $d_{15}$  of one piezo surface relative to the other, which is 335 pm/V for Pz23 and 500 pm/V for Pz27. In comparison, the nominal value of  $d_{15}$  for EBL3 is 730 pm/V, but measurements in lab 1 indicate  $d_{15} = 1.7$  nm/V; one free spectral range corresponds to an applied potential of about 250 V. Initial interferometer measurements in the lab were consistent with specified  $d_{15}$  values; a test cavity which Dal later built with Pz27 in October 2006 was found to travel 425 nm over 400 V, or  $d_{15} \approx 1$  nm/V. It remains to be seen whether the Ferroperm products will display a similar behavior in a cavity under vacuum. As for the response of the piezos to temperature stress, Yat tested Pz23 after baking for 48 hours at 198 °C and observed no change in maximum travel. Now that we have an oven capable of higher temperatures, it would be interesting to revisit this question.

Given the uncertainty about the range of the piezos, for several months we discussed a more significant redesign of the cavity mount. The impressive passive drift of  $< 10$  fm/s reported by Michael Chapman's group at Georgia Tech [47, 108] prompted us to consider a single expansion-mode piezo design, which they believed was the source of their stability [109]. Here as well we were confronted by the short travel range of the piezo for our small cavity as well as questions about stress induced by gluing the mirrors directly to the piezo. Yat then designed a mount in which an expansion-mode piezo drove a spring system formed by electrical discharge machining of an aluminum piece; the cavity mirrors were glued directly to the metal on either side of the spring. The design had several appealing features, including a large range of travel, mechanical stability because the mirrors shared a common mount, and the possibility of avoiding glue altogether. However, in initial tests, piezo expansion was found to tilt the mirror alignment along with changing the length of the cavity, probably due to nonuniform spring compression [105]. Finally, we have considered the option of giving up long-range piezo tuning altogether and instead relying on slow temperature tuning, either with a laser or a heating element inside the vacuum chamber. But as we have not yet demonstrated a satisfactory replacement, we have decided for the time being to rely on the previous cavity mount design, with the simpler substitution of high-temperature-compatible components.

### 6.2.2 Controlling birefringence

The challenge of controlling the cavity birefringence is of course connected to cavity redesign, since any mechanism to actively induce stress in the mirrors would have to be incorporated into the cavity mount, along with the usual considerations of UHV compatibility and optical access for the MOT and cavity beams. Toby spent the summer of 2005 engaged in two projects: using finite element analysis to model how stress on the mirror substrates leads to strain and a change in the mirror's index of refraction, and trying to induce and quantify birefringence with test cavities in the lab using jigs that I had designed. Unfortunately, due to the short length of his stay,

neither project was conclusive.

Yat and Dal then took on this project in the following year and spent some time characterizing the birefringence of test cavities. By first securing a mirror with a wire in order to pre-load it, then applying a voltage to a piezo wedged between the mirror and the wire, they successfully observed an induced birefringence. More sophisticated mounts for inducing stress were then employed, one in which a mirror was pre-loaded with set screws against two piezos which applied pressure from orthogonal directions, and a second (a possible candidate for use in UHV) in which the usual cavity mount design was adapted by placing an expansion-mode piezo inside one of the v-blocks. In all cases, the observed change in the birefringent splitting between the two orthogonal cavity modes was on the order of  $\frac{\Delta\nu}{FWM} = \frac{\Delta\nu}{2\kappa} = 1$ . This is in rough agreement with what we would expect from a finite element analysis model that Yat developed [105].

While these results are encouraging, at this time we still have no reliable means of controlling the birefringent splitting of our cavities. Moreover, the magnitude of the induced birefringence suggests that while we might (with a clever design) be able to eliminate the intrinsic birefringence of a cavity, we would have to increase the stress on the mirror coatings by at least two orders of magnitude in order to observe splittings large compared to  $g$ . One interesting prospect is the use of cylindrical piezoelectric transducers which could be custom-ordered with the same diameter as the mirror substrates. Under an applied voltage, the piezos would then squeeze the substrates, and a slit in the piezos could perhaps break the cylindrical symmetry, providing a preferred birefringent axis.

### 6.2.3 Cavity length

The lab 11 cavity, 42.2  $\mu\text{m}$  long, supports 99 half-wavelengths at  $\lambda_{Cs} = 852$  nm and 90 half-wavelengths at  $\lambda_{FORT} = 936$  nm. A cavity which is resonant at both wavelengths must therefore have a length which is an integer multiple of  $\frac{11\lambda_{Cs}}{2} = \frac{10\lambda_{FORT}}{2}$ . In order to maximize  $g$ , we would like to build the smallest such cavity that will still allow us to focus lattice beams through the cavity side gap, as in lab 11.

Imagine a Gaussian beam focused through a gap which is tens of microns wide and 1 mm long. Let the  $x$ -axis lie along the path of the beam with its origin at the center of the gap. If  $z$  is the beam waist at the focus (at  $x = 0$ ), then the beam waist as a function of  $x$ ,  $z$ , and the wavelength  $\lambda$  is given by

$$w(x, z, \lambda) = z \sqrt{1 + \left(\frac{x\lambda}{\pi z^2}\right)^2}. \quad (6.1)$$

We want to minimize  $w$  at  $x_{gap} = 0.5$  mm, the edge of the gap. We thus solve

$$\frac{dw(x_{gap}, z, \lambda_{Cs})}{dz} = 0 \quad (6.2)$$

to find  $z_{min} = 11.6$   $\mu\text{m}$ . The minimum gap between the mirrors is then given by

$$2w(x_{gap}, z_{min}, \lambda_{Cs}) = 32.9 \mu\text{m}. \quad (6.3)$$

The smallest co-resonant cavity that can accommodate this gap supports 88 half-wavelengths at  $\lambda_{Cs}$ , 80 half-wavelengths at  $\lambda_{FORT}$ , and is 37.5  $\mu\text{m}$  long. This is then the target length for our cavity.

The preceding discussion has not addressed the problem of diffraction. Siegman notes that an aperture criterion of  $4.6w$  is necessary to reduce spatial intensity variation to 1% [9]. In practice, we need to compromise between the demands of strong coupling and the desire for a uniform intensity along the cavity axis. What we have seen in lab 11 is that a 42.2  $\mu\text{m}$  gap allows us to perform effective lattice-based cooling, but that diffraction may be at the root of our difficulties in using side beams for optical pumping.

## 6.2.4 Rethinking passive stabilization

In past cavity systems, passive vibration isolation from the chamber and optical table has been provided by a series of heavy copper pieces separated by rubber bumpers of Viton and RTV. [21] We had two concerns regarding this design. First, it seemed

likely that outgassing from the Viton and RTV would limit the background pressure we could attain in our new system. Second, Viton can only be baked to 200 °C, and we hoped to bake out the system at higher temperatures.

On the recommendation of Ching-Tzu Chen, a graduate student in the Yeh group, we used an accelerometer to analyze the sensitivity of the cavity system. By measuring acceleration as a function of driving frequency at the location of the cavity mount, we established a baseline for the current system which we could then use to evaluate the efficacy of new designs. An alternate method to analyze the passive stability of the cavity is to lock it to a laser and then monitor the error signal from the lock; we also explored this option, using both the 852 nm probe and 936 nm FORT lasers.

The simplest redesign consisted of replacing both the Viton and RTV with Kalrez, a material which Travis discovered in his research. Viton and Kalrez are both manufactured by Dupont Dow; Viton is a fluoroelastomer, while Kalrez is a perfluoroelastomer, about ten times more expensive, has superior outgassing properties, and can be baked to 316 °C. (RTV stands for “room temperature vulcanization” and may refer to a number of silicone products.) In addition, the bumpers cut from Kalrez O-rings were loaded radially rather than axially, a technique known as streamline loading which produces a more uniform compression and improved damping. The measured sensitivity of the new system was found to be as good as the old one, with some improvements at low frequencies [110].

A more ambitious redesign came out of our discussions with LIGO staff scientist Riccardo DeSalvo. He suggested that we suspend our cavity mount from the walls of the vacuum chamber by employing the mini Geometric Anti-Spring (mini-GAS) system currently in use at the TAMA gravitational wave antenna in Japan [111]. In collaboration with Travis and Riccardo, Italian engineers who had produced the TAMA suspension designed a four-spring system made of beryllium copper that was compatible with our vacuum chamber. Its all-metal construction ensured that it would not be the limiting factor in determining bake-out temperature, and the anti-spring design avoids the long-term creep that ordinary spring systems experience. Although the design would provide effective passive suppression of high-frequency

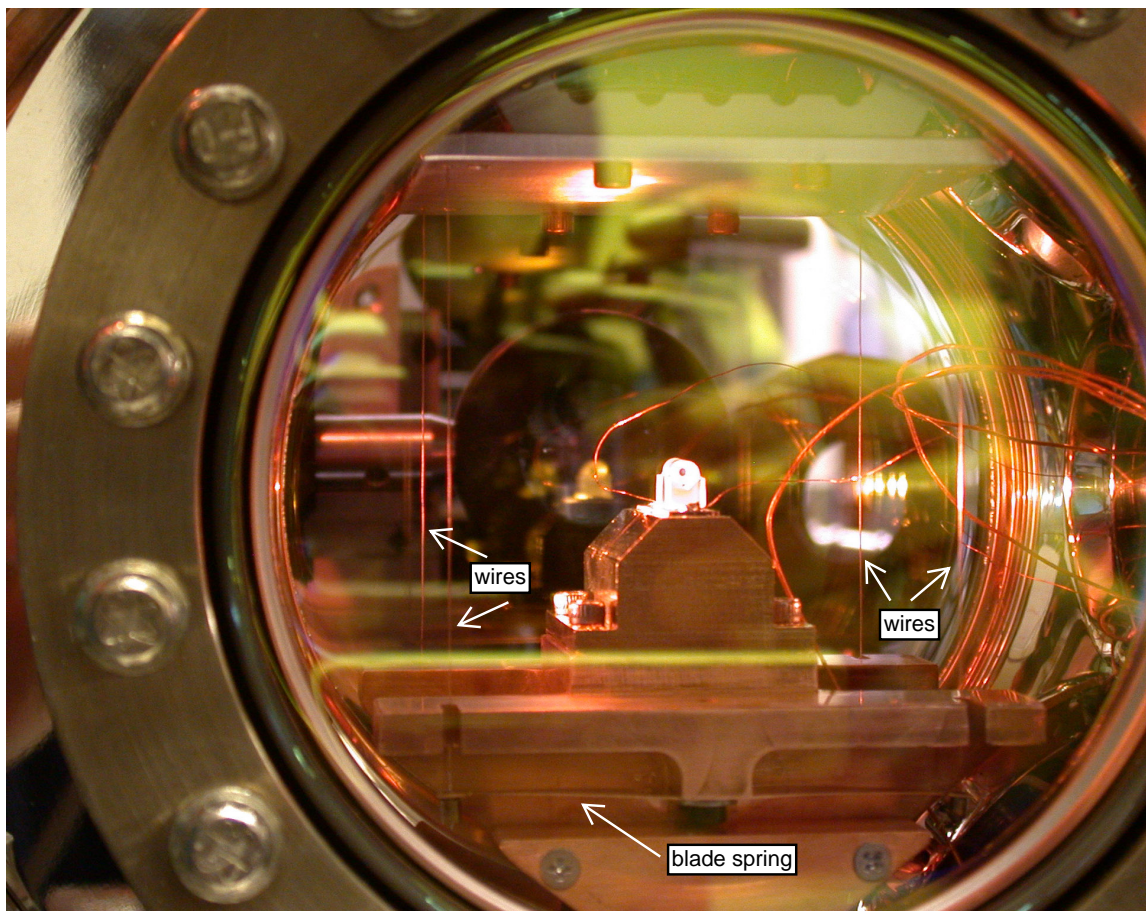


Figure 6.7: The mini-GAS suspension mount supports a cavity inside the lab 1 test vacuum chamber in June 2006. Note the four thin BeCu wires which are secured to blade springs beneath the mount.

noise, it would have a  $\sim 2$  Hz pendulum mode and a  $\sim 8$  Hz leaf spring resonance which would both require an active servo for compensation; we hoped to achieve this initially by using magnetic fields from the MOT coils to induce eddy-current damping in the mount.<sup>1</sup> The system arrived from Italy shortly before Travis's graduation. It was assembled within a test chamber (Figure 6.7) and characterized with both the accelerometer (Figure 6.8) and cavity lock techniques, which confirmed that the low frequency resonances were substantial; an attempt to observe damping from the MOT coils was unsuccessful. One possibility which might circumvent this difficulty

<sup>1</sup>The slow damping time of pendulum modes and daily creep are two reasons why the Chapman group, for example, has moved away from their earlier cavity suspension, despite its demonstrated excellent passive stability [109].

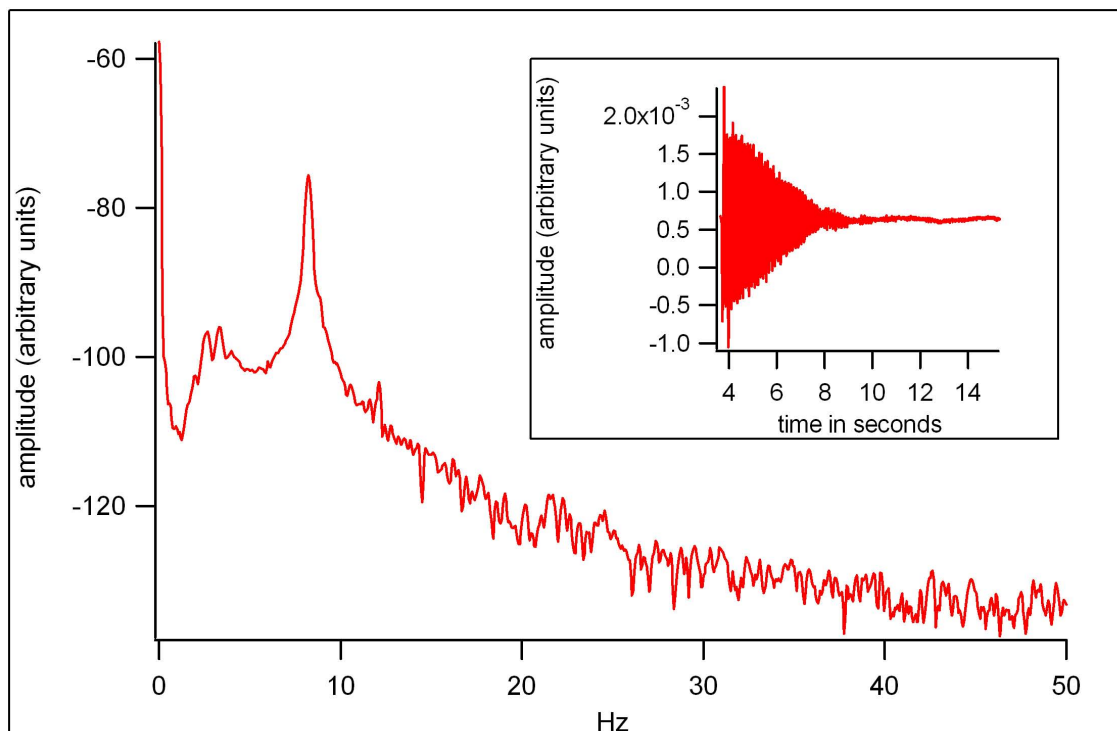


Figure 6.8: Accelerometer measurements of the mini-GAS suspension. The suspension mount is displaced and its ringdown as a function of time is recorded (inset). A Fourier transform of this data reveals expected resonances at around 2 Hz and 8 Hz, corresponding to the pendulum mode and the leaf spring resonance. Vibrations at higher frequencies are quickly damped by the spring system.

would be to use the suspension to support future microtoroid experiments. As light is coupled in and out of the microtoroids via optical fiber rather than in free space, the motion of the cavity with respect to the vacuum chamber is no longer a cause for concern, and perhaps low-frequency active damping could be avoided entirely.

### 6.2.5 Vacuum chamber

We decided to purchase new vacuum chamber components rather than attempt to reuse the old cavity chamber. This allowed us not to worry about damaged knife edges from old components that might compromise vacuum, and it provided us with a backup chamber in which we could test vibration isolation.

I attempted to stay as close to the previous chamber design as possible, for simplicity and ease in reusing input and output optics. The lower chamber had been

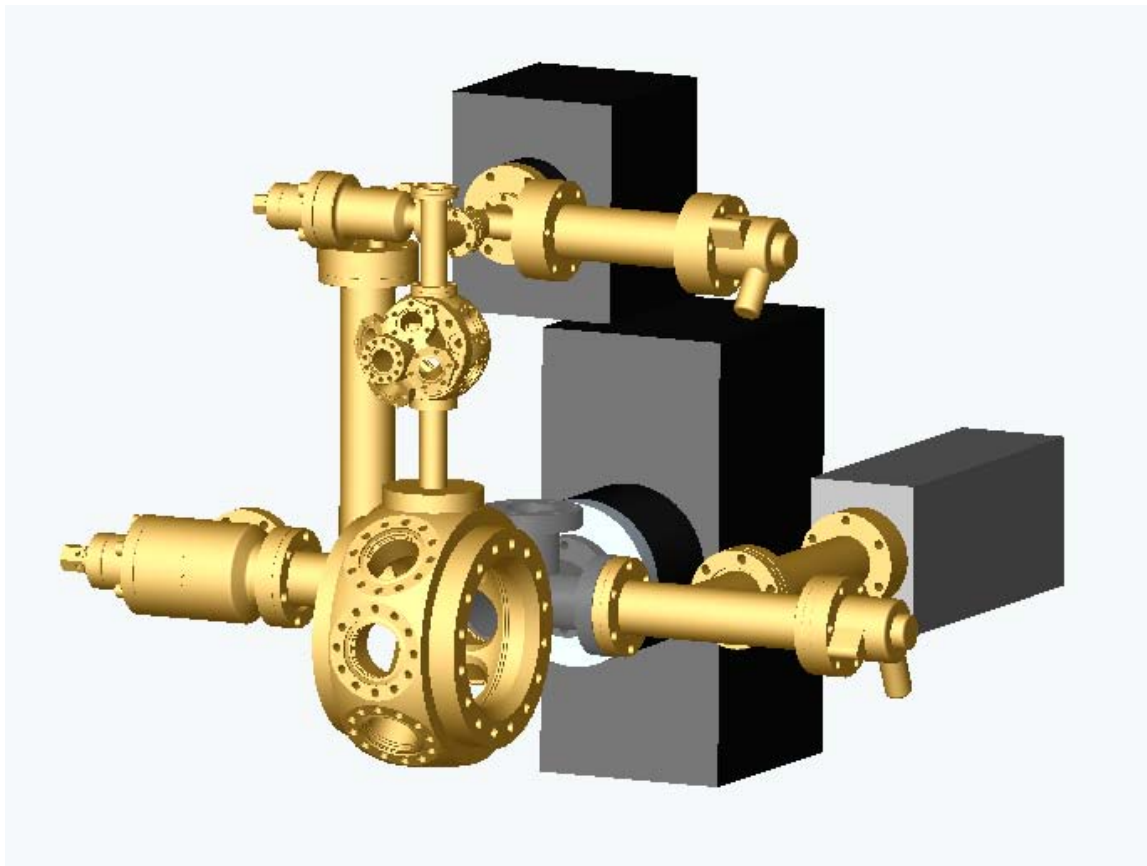


Figure 6.9: Vacuum chamber design for a new asymmetric cavity. Much of the earlier lab 1 design remains intact, with an upper and lower chamber connected by a differential pumping tube and brought to UHV with two Varian ion pumps. New components include a residual gas analyzer (RGA), a titanium sublimation pump, and a multiplexer port on the upper chamber in order to incorporate getters.

custom-built by NorCal and was replaced with a Kimball Physics 6" spherical octagon of similar dimensions. The upper chamber was again a 2.75" Kimball Physics spherical hexagon. The 55 l/s and 20 l/s Varian VacIon Plus Starcell ion pumps that had been used for the lower and upper chambers were also replicated. The new differential pumping tube was identical to the older one, as it was a backup version that had been machined at the same time. Both chambers now had nude Bayert-Alpert ionization gauges from Varian, model UHV-24 for the upper chamber and UHV-24p (lower pressure limits  $2 \times 10^{-11}$  torr and  $5 \times 10^{-12}$  torr, respectively) for the lower chamber. All-metal gate valves from VAT could be used to pump down the upper and lower chambers simultaneously.

From his experience building vacuum chambers at Michigan, Russ Miller suggested that we include a residual gas analyzer (RGA200, SRS) in order to diagnose any leaks we encountered and a titanium sublimation pump (Lesker) to reduce the final system pressure by an order of magnitude. As we were concerned about the possibility of titanium sputtering near our mirrors, there is no line of sight between this pump and the cavity.

The previous chamber had used a cesium ampoule to load the upper chamber MOT from a reservoir of background gas. We decided instead to implement the newer technique of “getters,” alkali metal dispensers which emit a vapor when they are resistively heated [112, 113]. Using getters is simpler, more compact and avoids problems associated with successfully breaking the glass ampoule under vacuum. It also permits a lower background pressure in the chamber, especially if the getters are operated in a pulsed configuration. However, the metal in each dispenser eventually becomes depleted; how long this takes depends on the current at which the dispenser is operated, as well as whether it has been subjected to short bursts of high current. We have seen getters in use in the atomic ensembles experiment (lab 2) last only several months. In comparison, the amount of cesium provided by the lab 1 ampoule has been sufficient for the past ten years. Cindy Regal reports that at JILA, getters are used for glass chambers, but in stainless steel chambers (where alkali atoms are absorbed by the walls), ampoules are still used. Our getter design replaced a 2.75” window on the upper chamber with a five-port 2.75” multiplexer (Kimball Physics); the center port was for a MOT beam, while the others could be used for getters. With two getters per port, we could in principle stock our chamber with eight getters and hope for several years of operation before they were all depleted. One encouraging factor is our chamber geometry, which allows us to place the getters  $\sim 2$  cm from the upper MOT. Thus, we are able to form a bright MOT with lower currents than have been necessary in lab 2 and, more recently, in the microtoroid experiment: Dal and summer student Jie Wu measured  $N_{atoms} \sim 10^8$  with 3.25 A through the getters, well below the threshold current of  $\sim 4$  A where the response becomes nonlinear [114]; labs 2 and 11a operate at or above this threshold. (It is, however, necessary to

Vacuum Components	°C
Stainless steel chambers, upper and lower	450
Stainless nipples and flanges	450
Stainless tees, crosses, multiplexers	450
Differential pumping tube	450
Getter feedthroughs	450
PZT feedthrough	450
Valves for roughing pumps	450 open 350 closed
Viewports, without AR coating	400
Ion pumps without magnets	350
Titanium sublimation pump cartridge	350
Residual gas analyzer (RGA)	300

Table 6.2: Maximum baking temperatures for vacuum chamber components

operate the getters briefly above threshold during bake-out as part of an “outgassing” process to remove impurities from the surface. This process should be repeated after each instance in which the getters are exposed to air [115].)

In Table 6.2, I list the maximum baking temperatures for our vacuum chamber components, also reproduced in Yat’s thesis. In the past, we have obtained UHV viewports from Larsen with anti-reflection (AR) coatings applied by Guernsey. The uncoated viewports have a baking temperature of 400 °C limited by the glass-to-metal transition, but according to Guernsey engineers, the coatings could not be baked above 250 °C. As this would potentially limit our bake-out temperature, we arranged for a coating run by Advanced Thin Films (Longmont, Colorado) on bare Larsen viewports. These coatings reflect less than 0.5% of light between 800 and 950 nm and no longer limit the viewport baking temperature.

In order to determine our target bake-out temperature, Yat was able to find measured thermal desorption spectra for 316LN stainless steel. [116] These indicated a desorption peak for water molecules at around 300 °C. Thus, even if our cavity mount assembly required lower temperatures, we would at least plan to pre-bake the chamber itself above 300 °C for several days. We purchased a large custom oven from Milmetco which could reach temperatures of 600 °F (316 °C). We threaded a 48 inch braided bellows through a hole in the side of the oven so that we could bake the

chamber under vacuum. Inside the oven, one end of the bellows attached to a tee from which two smaller bellows connected to the upper and lower all-metal valves of the chamber. Outside the oven, the other end of the bellows allowed us to pump either with a turbo pumping station (Pfeiffer TSU071) or, at lower pressures, with an ion pump (VacIon Plus 40 Starcell). The chamber, of course, has its own ion pumps attached, but as their magnets have to be removed temporarily for baking, we are not able to use them inside the oven.

### 6.2.6 Current project status

We assembled the two-chamber vacuum system, absent the cavity or the cavity mount apparatus, in the fall and winter of 2005. We successfully demonstrated a pressure of  $\leq 5 \times 10^{-12}$  torr in the empty chamber (the resolution limit of the nude ion gauge) one month after firing the titanium sublimation pump, with blanks substituted for the viewports during this initial test. Dal has also explored the option of placing an unbaked cavity (with the cavity mount components baked separately before assembly) inside of a pre-baked chamber and vibration isolation system, venting it to nitrogen during the  $\sim 15$  minute transfer process, and he has confirmed that the chamber with cavity returns to its initial pressure after several months. (In this instance, the pressure was  $\sim 10^{-10}$  torr in order to expedite the process. As the use of the titanium sublimation pump should improve the pressure by an order of magnitude, this result suggests that we may not need in-situ baking of the cavity mirrors.)

At the moment, the chamber is simply waiting for a cavity. As I have discussed in this chapter, some questions about how to improve the cavity design, such as incorporating control over birefringence, have not yet been resolved. The primary cause for delay, however, has been our quest for better cavity mirrors. In the following chapter, I describe our goals in improving mirror losses, the process of mirror characterization, and the results of this effort to date.

## Chapter 7

# In search of the perfect mirror

### 7.1 New mirrors for a new cavity

In October 2004, the decision was made to replace the lab 1 cavity built by Kevin Birnbaum and Theresa Lynn with a new, single-sided cavity. Central to the cavity project was the need to re-establish connections with the manufacturers of our high-finesse mirrors. Collaborations between our group and Ramin Lalezari of PMS Electro-Optics in Boulder, Colorado (later Research Electro-Optics) had produced record-low mirror losses in 1991 [8]. These “supermirrors” had total losses (transmission plus scatter and absorption) of just 1.6 parts per million, corresponding to a cavity finesse of  $1.9 \times 10^6$ . A few years later, Quentin Turchette and postdoc Michael Chapman worked with Research Electro-Optics (REO) to develop the tapered 3 mm / 1 mm mirrors which are now used in several labs worldwide. Christina Hood then traveled to REO in order to develop improved mirror cleaning and handling techniques [21].

The state-of-the-art mirrors which our lab relies on for strong-coupling cavity QED were thus a product of extensive back-and-forth dialogue with industry, but by 2004, this dialogue had lapsed for several years. Meanwhile, Ramin had left REO to start his own company, Advanced Thin Films (ATF), in Longmont, Colorado. We hoped that by placing orders with both REO and ATF for new mirror coating runs, we could encourage the two companies to push the scatter and absorption of their mirrors to new lows.

In March 2005, I drove to Colorado with a breadboard of mirror-testing equipment, since neither company had the ability to characterize such low-loss mirrors at 850 nm. I spent several weeks there that spring and summer and have made two subsequent trips to measure more recent ATF coating runs. In this chapter, I summarize that experience, focusing both on techniques to characterize mirrors efficiently and on what we've learned about the present limits of mirror coating technology. Furthermore, I discuss the implications of current mirror technology for proposed cavity QED experiments in our lab.

## 7.2 The nuts and bolts of mirror testing

We can define a mirror at a given wavelength by its reflection,  $R$ , its transmission,  $T$ , and its scatter and absorption losses,  $S + A = l$ , where

$$R + T + l = 1. \quad (7.1)$$

In theory, one could determine the values of  $R$ ,  $T$ , and  $l$  by placing the mirror in a laser path, measuring the fractions of the beam transmitted and reflected, and attributing the rest to losses. In practice, when we need to discern transmissions and losses on the order of  $10^{-6}$  or  $10^{-7}$ , detector nonlinearity and scattered light into the detectors present serious problems for this method. A more reliable approach is to construct an optical cavity from two identical mirrors and then to characterize the cavity.

Christina Hood and Jun Ye outline their procedure for characterization of cavity mirrors in Refs. [21] and [42]; specifically, this procedure is based on their 1999 investigation of mirrors from REO coating run no. T95, the source for the current lab 11 cavity and past lab 1 cavities. First, a measurement of cavity finesse  $\mathcal{F}$  determines total losses  $\mathcal{L} = T + l$ , since  $\mathcal{F} = \frac{FSR}{FWHM} = \frac{FSR}{2(\kappa/2\pi)} = \frac{2\pi}{\mathcal{L}}$  in the low-loss cavity limit [9]. Here FSR is the cavity's free spectral range, the spacing between longitudinal modes, which can be determined from cavity length or (for a very short cavity) with

a wavemeter;  $\kappa$  is the HWHM linewidth of the cavity’s TEM<sub>00</sub> mode. If the mirrors’ losses are low enough and the cavity is long enough,  $\kappa$  can be measured directly via cavity ringdown in order to determine finesse. Alternatively, frequency sidebands applied to a probe laser can provide a meterstick for  $\kappa$  as the cavity length is scanned with a piezo. (More sophisticated methods of measuring  $\kappa$  for short cavities are available when the cavity length can be actively locked; Section 4.3 of Ref. [29] provides details.) Next, in order to partition total losses into  $T$  and  $l$ , cavity transmission and reflection on resonance are measured simultaneously and compared with the input power to the cavity.

This technique presupposes the cavity mirrors to be identical, a reasonable assumption if they are from the same coating run and appear defect-free under microscope inspection. It is also possible to characterize the two mirrors independently by repeating the transmission/reflection partitioning described above with light incident from the opposite side of the cavity [117].

### 7.2.1 A portable testing apparatus

When we discussed a new coating run with REO in the winter of 2004–5, they had recently completed a mirror coating/coning process for Dieter Meschede’s group at the University of Bonn. REO had initially been unable to meet the specifications of  $\mathcal{F} \sim 500,000$  until a student arrived from Bonn with equipment to quantify mirror losses at the company. The advantage of having feedback within a few hours about the results of a coating run is that the same ion beam sputtering (IBS) machine can be used again right away for a second coating, without any changes to the machine’s settings except a few tweaks indicated by the measurement, thus insuring repeatability. It was decided that I would travel to Boulder to measure the results of an initial test run and all subsequent attempts until the mirrors were found to be consistent with our target values of  $T$  and  $l$ . I would also be able to re-measure the mirrors after they were coned by REO opticians in order to document any new losses. (From the Bonn run, about 50% of the mirrors that entered the coning process were “catastrophically

damaged” and another 20% had their finesse reduced by the process [118]).

In order to replicate Christina’s and Jun’s measurements in Colorado, I assembled a breadboard of optics equipment which could be transported by car. An external-cavity diode laser (ECDL) at 852 nm would be used to characterize the mirrors. The laser passed through a prism pair, an isolator, and an acousto-optic modulator (AOM) to switch off the beam for cavity ringdown. Coupling through optical fiber provided spatial cleaning and allowed for easy replacement of the 852 laser with another fiber-coupled laser. A HeNe laser, for example, was often used to align the cavity mirrors, since the mirrors have much higher transmission at visible wavelengths. At the fiber output, the beam was telescoped and then mode-matched to the TEM<sub>00</sub> cavity waist with a lens on a translation stage. Before entering the cavity, the beam passed through a polarizing beam splitter (PBS) cube and a quarter waveplate. Reflected light from the cavity, after a second pass through the quarter waveplate, was then reflected by the PBS and focused onto a New Focus 1801 125 MHz detector; transmitted cavity light was collimated and then focused onto an identical detector. Before the breadboard left for Boulder, undergraduate Yat Shan Au replicated it in the lab 1 “clean hood” so that we would have our own testing and cavity construction setup available [105].

In order to mount the cavity mirrors for measurement purposes, I used two miniature v-groove setups (for 7.75 mm and for 3 mm diameter mirrors), both with nylon-tipped set-screw clamps from above, as shown in Figure 7.1. Each v-groove was originally machined from a single aluminum piece; the groove was then cut in half, with one half mounted in a fixed position while the other was attached to a miniature piezo-driven translation stage from Physik Instrumente (Karlsruhe, Germany). This allowed the cavity length to be adjusted over several millimeters (with the translation stage micrometer) and to be scanned over much smaller distances with a voltage input to the piezo from either a function generator or a battery box.

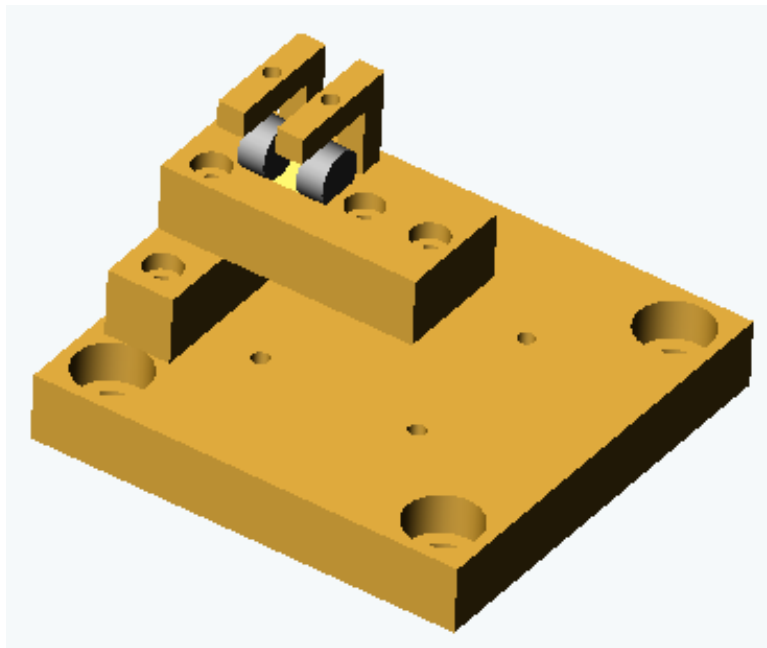


Figure 7.1: Mirror mount assembly for test cavities. Two 7.75 mm mirrors sit in a v-groove (which was later cut in half) and are clamped from above with nylon-tipped set screws. The right half of the v-groove was mounted on a piezo-driven translation stage from Physik Instrumente (not pictured), attached with screws to the base plate. This v-groove block could be quickly exchanged for a smaller one, machined for 3 mm mirrors.

### 7.2.2 Cavity construction and alignment

When two mirrors were ready to be tested, they were placed into the grooves of the mirror holder blocks using Teflon-tipped tweezers. The rear face of each mirror substrate was gently placed in contact with a shallow notch the end of the groove to ensure reproducible cavity length, and the mirrors were then secured by set screws. Initial alignment was done with all coupling lenses removed and with a HeNe input to the fiber coupler; the mirrors in the beam path before the cavity were then adjusted so that (a) the beam intersected both mirrors near their centers, (b) the reflections from the back of the first mirror and the front of the second mirror overlapped the incoming beam, and (c) the reflected and transmitted beams were incident on their respective detectors. The coupling lenses were then replaced and positioned so as to preserve the beam path. At this point, scanning the applied voltage on the cavity

piezo should produce HeNe fringes, visible either on a white card (for slow scan rates,  $\sim$  a few Hz) or at the detectors. Simply by switching the fiber-coupled input back to the ECDL laser source, transmission peaks and reflection dips at 852 nm should be visible on the detectors and can then be improved by mirror alignment. Triggering the AOM to switch off once a transmission threshold is crossed provides the sought-after ringdown signal.

There is a rather steep learning curve associated with cavity construction and measurement, as I discovered before traveling to Boulder (and as Dal Wilson has discovered since). Here Christina Hood's alignment procedure outlined in 5.2.2 of Ref. [21] proved invaluable. I would like to add a few points of my own in the hope that they may be helpful to future cavity-builders.

#### **7.2.2.1 Reflected spots**

It is worth noting that the rear face of a mirror substrate (either unconed or coned) is not perpendicular to its cylindrical surface. The rear face has been cut at an angle (wedge) in order to prevent problems associated with secondary reflection. (Additionally, the rear face is anti-reflection coated.) This is certainly true for the most recent coating runs, though I am unsure about earlier runs. As a result, when positioning cavity mirrors by aligning their reflected spots, one should expect that the spots reflected from the two faces of a single substrate will not be in alignment, and that their relative position is just a function of the rotation angle of the mirror. Only the spots reflected from the mirror faces themselves need to be aligned.

#### **7.2.2.2 Mirror cleaning**

From the REO technician who was most successful at cleaning the coned mirrors, I learned that she used lint-free cotton swabs (Huby-340, distributed by Sanborn Co.) which have a fairly dense tip. After dark-field microscope inspection, she applied a small amount of spectrophotometric-grade solvent to a swab tip. She then made a gentle, quick contact with the mirror surface, rotating her wrist outwards as she brought the swab towards her in order to avoid dragging particles across the surface.

Mirrors are now stored and transported in Gel-Pak containers, mirror face up; the rear surface is attached to the sticky Gel-Pak surface and can be cleaned with solvent upon removal if necessary.

For cleaning the 7.75 mm mirrors, technicians at both REO and ATF used a wafer spin cleaner (PM80, Headway Research). The mirror is set in a chuck, held in place with suction, and then spun via a foot pedal. A solvent is first applied directly to the mirror from a squirt bottle in order to wet it. (Again, the solvent should be spectrophotometric grade. When an empty bottle is filled, it should be first cleaned with compressed nitrogen to remove water vapor and should be filled on the same day as the cleaning.) A glue-free cotton swab is then also wet with solvent. While the squirt bottle is used to keep the mirror continuously wet, the swab is touched to the center of the optic. About ten seconds of gentle pressure is applied as the swab is gradually moved to the mirror edge. The piece is then spun for another 10 to 20 seconds without swab or solvent until it is dry. The appropriate sequence of solvents to use when removing varnish is a) water, b) acetone, and c) isopropyl alcohol. When just removing dust from a mirror, isopropyl alcohol alone is sufficient. Methanol is not well-suited for spin cleaning because it dries too fast. We have subsequently used a LIGO spin cleaner in the East Bridge sub-basement to clean 7.75 mm mirrors and have found this to be a faster, more consistent process than cleaning by hand.

### 7.2.2.3 Measurement laser

Most previous cavity measurements in our lab by Christina, Theresa, and others were carried out using a Ti:sapphire laser. The large power from the Ti:sapphire was not helpful for these measurements and in fact had to be heavily filtered (see Section 7.2.2.4), but the tunable range of the laser made it possible to map out mirror coating curves [42] and to measure the free spectral range of a small cavity [4]. Only after a series of cavity measurements using ECDLs did I appreciate a secondary benefit of the Ti:sapphire: its narrow linewidth. The supermirror cavities we construct for physics experiments have short lengths ( $\sim 40 \mu\text{m}$ ) and thus relatively broad linewidths ( $\kappa \sim 2\pi \times 4 \text{ MHz}$ ). But for testing purposes, it is convenient to build longer cavities

whose ringdown time  $\tau = \frac{1}{2\kappa}$  is much longer than the detector response time or the time to turn off the cavity input field ( $\sim 25$  ns for a good AOM). For example, a ringdown time of  $1 \mu\text{s}$  might correspond to a 5 mm, 80 kHz cavity, still broader than our Ti:sapphire linewidth, but narrower than our ECDLs, which have linewidths of roughly 500 kHz. So even a lossless test cavity on resonance with an input ECDL would only be able to accept and transmit a small percentage of its input power. For mirrors where  $T \ll l$ , the transmission efficiency is of course much worse, and a signal may be hard to discern from noise. One solution to this difficulty is presented in Section 7.2.3.

#### 7.2.2.4 Cavity input power

Since the cavity input power is multiplied by a factor of  $\mathcal{F}$  to generate the intracavity power, and since the waist of the intracavity field is quite small, the power per unit area incident on the cavity mirrors can be quite astonishing, even for small input powers. In lab 11, “lab lore” in the past has been that the cavity input power at 852 nm should never be greater than a few  $\mu\text{W}$  to avoid damage to the cavity coatings. However, when searching for a transmission signal while aligning test cavity mirrors, one would like to use as much input light as possible. When I discussed the question of a damage threshold with Sam Richman, the metrology lab manager at REO, he estimated that “continuous wave damage of these IBS coatings is governed by a thermal process that is directly related to the absorption... We don’t make any measurements of this continuous wave damage threshold, but it is probably in the neighborhood of  $10^8 \text{ W/cm}^2$ ” [119].

Assuming a radius of  $\sim 20 \mu\text{m}$  for the beam spot size on the mirrors, a finesse of  $10^6$ , and perfect mode-matching of a narrow-linewidth laser, this would suggest that a damage threshold might correspond to  $\sim 1 \text{ mW}$  of input power. Since our mode-matching is in practice far from perfect, it seems safe in the future to limit cavity input powers to  $\leq 100 \mu\text{m}$ .

### 7.2.2.5 Loss partitioning

In the measurements of the cavity described in Ref. [42] (the same one still under vacuum in the lab 11 experiment), the cavity length was locked on resonance and resonant powers in transmission and reflection  $P_t$  and  $P_r$  were recorded. With the additional knowledge of the cavity input power  $P_i$ , one can solve equations (2.1) and (2.4) of [42] to find

$$T = \frac{2r(\pi/\mathcal{F})}{1+r}, \quad (7.2)$$

where  $r = \frac{P_t}{P_i - P_r}$ . Scattering and absorption losses are then given by

$$l = \frac{\pi}{\mathcal{F}} - T. \quad (7.3)$$

Instead of locking the cavity, one can also compare the relative heights of the transmission peak ( $P_t$ ) and the reflection dip ( $P_i - P_r$ ) on identical detectors while scanning the cavity. Theresa Lynn and I used this technique in early 2003 to characterize some initial coating runs that Ramin had done at his new company. For the technique to be accurate, it is important that the scan time across the peaks be much greater than the cavity ringdown time, so cavity lengths should be relatively short. (A symptom of this problem is a visible asymmetry in the appearance of the cavity scans when the ringdown time is nonnegligible.) If a voltage scan of the cavity piezo is too noisy, one solution is to turn off the applied voltage and let the cavity drift passively across the resonance, capturing images of the transmission peak and reflection dip with a digital scope.

Note that when mode-matching to the cavity is bad,  $P_r \gg P_t$ ,  $P_i \approx P_r$ , and  $r$  depends very sensitively on an accurate measurement of  $P_r$ . This difficulty is compounded for a low-transmission coating in which  $P_r$  would be greater than  $P_t$  even with perfect mode-matching. At REO in Boulder, because of diode laser inefficiencies (7.2.2.4), I was only able to do a very rough partitioning of low-transmission mirror losses.

### 7.2.2.6 Design of cavity mounts

I had hoped that the machining of the mirror grooves (Figure 7.1) would be accurate enough to define a cavity without adjustment, and that this geometry would be reproducible when one mirror was exchanged for another. Neither of these assumptions held in practice, due in part to centration error on the mirrors from the machining process; that is, after a mirror substrate has been coned down, the angle at which light reflects off the mirror will change as the mirror is rotated around its cylindrical axis. In order to form a cavity, I had to resort to sliding pieces of tape under the second mirror block in order to compensate for the tilt angle, tapping the mirror to rotate it within the v-block, and loosening the screws attaching it to the piezo stage for left/right adjustment.

For the future, I would recommend a design in which the second mirror holder is replaced with a small Lees mirror mount attached to the piezo stage, modified with adapters so that it can accept either mirror diameter.

### 7.2.3 A simpler solution: self-locking cavity ringdown

After characterizing unconed and coned mirrors at REO in April 2005, I drove the breadboard apparatus 15 miles north to the ATF facilities in Longmont. In August 2005, I returned to ATF to provide quick feedback as they attempted a series of coating runs. During this visit, Ramin suggested a simpler measurement method for cavity ringdown based on optical feedback to the laser from the test cavity.

In ordinary circumstances, optical feedback is the bane of the experimentalist. We use current, temperature, and grating position to carefully select the frequency of our semiconductor laser diodes, and unwanted reflections back into the diode can seriously disrupt that frequency. However, if we instead set up our test cavity to feed back into the laser diode on purpose, the result will be that a) the diode frequency attempts to lock to a cavity mode, with a subsequent line-narrowing [120], and b) because of the resonant frequency and narrowed linewidth, there is a substantial power buildup within the test cavity [121].

Note that for most lab applications, we require a very specific laser frequency (referenced to cesium) that can only be achieved by tuning an external grating. In this case, however, we only need to know about the mirrors' behavior to within a few nm, since that is the scale on which the coating curve varies. We can start with a diode which lases at approximately at 852 nm and then allow the test cavity to do the rest of the work. In doing so, we have discarded the need for isolators, piezos to scan the length of the test cavity in order to match it to the laser wavelength, and the construction of a temperature-stabilized external cavity around the diode.

This approach is particularly appealing for testing low-transmission mirrors, where  $T \sim 0.1\text{--}0.5 \text{ ppm} \ll l \sim 2 \text{ ppm}$ . The small ratio of  $T/l$  means that on-resonance cavity transmission may be reduced by a factor of 100. When coupled with already low efficiencies because of the narrow cavity linewidth with respect to the diode laser's linewidth, the result is a ringdown signal that can be difficult to measure. Here the fact that optical feedback allows the laser to adapt to the cavity becomes a tremendous advantage; Dahmani reports feedback-induced linewidth narrowing by a factor of 1000 [120].

### 7.2.3.1 A breadboard setup for cavity-locked lasers

At ATF, Ramin had already set up a prototype system consisting of a HeNe laser, a lens, two test mirrors, and a fast detector built by Mark Notcutt of JILA. The detector had a Schmitt trigger that would send a signal to turn off the laser whenever the cavity output exceeded an adjustable threshold, thus triggering a cavity ringdown. When the HeNe was locked to the cavity, the cavity buildup field (or rather, its scatter from air particles) was visible to the naked eye. At the end of my August stay, we adapted the 852 nm ECDL as the basis for a similar setup, with satisfying results: despite the external grating which mitigated the cavity feedback effect, we observed much more substantial cavity buildup than I had previously achieved. As a result, I could fit cavity ringdowns with higher confidence and with greatly reduced preparation time.

Upon returning to Caltech, I constructed and tested a similar arrangement, which Dal and I later set up at ATF in January 2007. As depicted in Figure 7.2, a bare

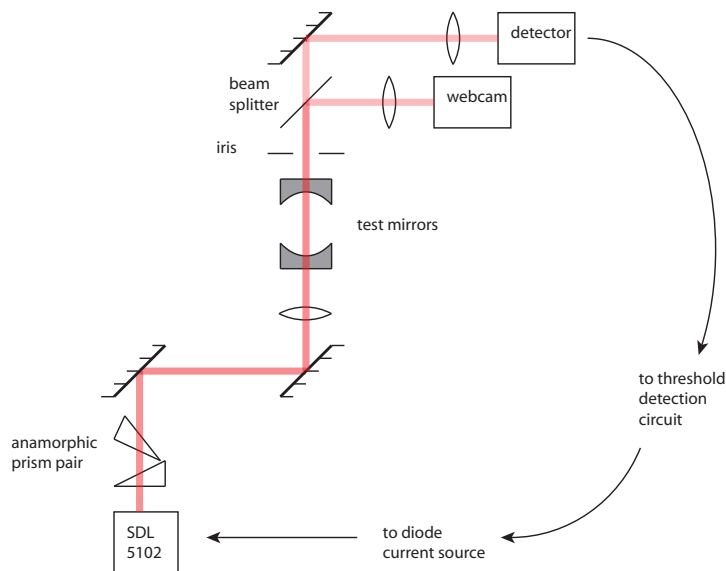


Figure 7.2: A simple breadboard setup for self-locking cavity ringdown, implemented both at Advanced Thin Films and in our lab for testing mirror coatings

SDL-5102 diode is driven by a commercial diode laser current supply (TMD-219 from Power Technology) which can be switched off via a TTL signal. Again, the testing components are simply the diode, a prism pair, two lenses, a detector (Thorlabs PDA10A), and the cavity mirrors. The cavity mirrors are mounted in Newport mirror mounts with a 7.75 mm to 1 inch adapter machined at ATF. The detector signal goes to a variable gain amplifier which sets the turn-off threshold, followed by a monostable multivibrator circuit (adapted from one built by former graduate student James Chou) which provides the TTL signal for the current supply.

Alignment of the system can be done very quickly and reliably. The diode output is first attenuated and then aligned into the detector. The second cavity mirror is placed in the center of the beam path and adjusted so as to align its reflection with the incoming light. (Using an IR viewer, one can sometimes see the diode output light “flash” when feedback is achieved. Alternatively, the very small amount of transmitted light visible on the output detector — with the attenuation now removed — becomes suddenly noisier.) Finally, the first cavity mirror is placed in the beam path, and its retroreflection is also aligned into the diode. Once the retroreflection is

nearly aligned, transmission peaks become visible on the output detector, and both cavity mirrors can then be adjusted so as to maximize transmission. Sometimes it is necessary to tap the optical table or the mirror mounts in order for the cavity to find a laser mode to which it can lock; at ATF, this source of vibration was conveniently provided by the somewhat noisy HEPA filter on the optical table.

For low transmission mirrors, an iris after the second cavity mirror can eliminate scattered light into the detector. It is also useful to pick off some cavity output light with a beam splitter and focus it onto a camera (in our case, a USB-connected webcam from which we removed the lens) in order to image the cavity mode. The cavity mirrors can then be tweaked so as to maximize the  $\text{TEM}_{00}$  mode rather than higher-order modes, which may have different ringdown times as they sample larger areas of the mirror surface. The mirror adapters can be rotated within their mounts in order to sample the mirror coating in different locations and thus characterize its uniformity. It may also be useful to place one of the mounts on a translation stage for this purpose.

One note about reflected light from the cavity: this method relies on that reflection as feedback to lock the diode laser, but as the laser comes into resonance with the cavity, the reflected power and thus the feedback signal drops, creating an unstable situation. Researchers concerned with stable locking have employed techniques including multiple cavity modes [120], waveplates and polarizers [121], and spatial filtering [122] in order to address this issue. For our purposes, we only require the laser to lock to the cavity for long enough to trigger the cavity ringdown, so this level of sophistication is unnecessary. However, in the future, one might consider using a beam splitter to bring some of the reflected cavity light to a second detector and then implementing a loss partitioning scheme similar to that in Section 7.2.2.5.

### 7.2.3.2 Scattering losses in air

Finally, the test cavities we have built using this self-locking scheme have been several cm long, convenient for accurately measuring cavity length with calipers. In this situation, however, air loss becomes a small but non-negligible issue. Here I am grateful

for the help of David Robichaud, a graduate student in Caltech’s Okimura group who uses cavity ringdown spectroscopy to study atmospheric free radical chemistry. In Robichaud’s air loss calculations, he considers only Rayleigh scattering in the atmosphere, i.e., by  $\text{N}_2$  and  $\text{O}_2$  (other less significant sources of atmospheric attenuation could be due to Mie scattering of aerosols and to absorption). Rayleigh scattering is the limit of Mie theory in the case where particle size is much smaller than the optical wavelength. The Rayleigh extinction coefficient due to scattering is given by

$$a_s(\lambda) = \left(\frac{2\pi}{\lambda}\right)^4 \frac{(n^2(\lambda) - 1)^2}{6\pi N}, \quad (7.4)$$

where  $\lambda$  is the wavelength of light,  $n(\lambda)$  is the index of refraction, and  $N$  is the density of scatterers [123]. Note that  $a_s(\lambda) = N\sigma(\lambda)$ , where  $\sigma(\lambda)$  is the scattering cross-section.

We can calculate  $N$  in units of  $\text{m}^{-3}$  from the ideal gas law: if  $T = 296$  K and  $P = 1$  atm, then  $N = 2.48 \times 10^{25}/\text{m}^3$ . The refractive index of air at 852 nm is about 1.000269 [124]. Using equation (7.4), we find  $a_s = 1.83 \times 10^{-8}$ . The attenuation due to Rayleigh scattering is then given by  $I(x) = I(0)e^{-a_s x}$ , where  $I(x)$  is the intensity of light at distance  $x$  from the source. So for each mirror bounce, i.e., each trip of distance  $d$  within a cavity of length  $d$ , the light is attenuated by a factor of  $e^{-a_s d} \simeq (1 - a_s d) = (1 - l_{\text{Rayleigh}})$ . If  $d$  is 10 cm, then  $l_{\text{Rayleigh}} = 0.18$  ppm, and  $l_{\text{Rayleigh}} + l + T = \mathcal{L}_{\text{total}}$ , where  $\mathcal{L}_{\text{total}}$  is the per-mirror loss inferred from cavity ringdown.

## 7.3 Results of the coating runs

### 7.3.1 REO

Our agreement with REO was for “best effort” fabrication, coating, and coning of two sets of mirrors. Each set consisted of ten mirrors with 5 cm radius of curvature (ROC) and five mirrors with 10 cm ROC. In both cases, the target  $S + A$  losses were  $< 2$  ppm; for the first (high transmission) set, the target transmission was  $15 \pm 2.5$

ppm at 852 nm, while for the second (low transmission) set, the goal was  $T = 0.1 - 0.5$  ppm. An additional specification was for  $R > 99.9\%$  at 936 nm, so that the cavity mirrors could support a magic-wavelength FORT as in lab 11. (In order to achieve this for the high transmission mirrors, the center wavelength of the coating would in fact be higher than 852 nm, though the transmission at 852 nm would still meet our target.)

Once I had arrived in Boulder, REO did a test run of high and low transmission mirrors. The initial high transmission mirrors were found to have  $T = 8-10$  ppm at 852 nm, so the coating engineers shifted the design parameters to aim for a higher transmission in a second test run, which then met specifications. Sam Richman was perplexed by a  $\sim 25\%$  discrepancy between my ringdown data and transmission measurements done on the REO spectrophotometer, but after the same discrepancy was found to hold for some 15 ppm mirrors which he characterized at 633 nm, we concluded that the spectrophotometer calibration was at fault, further evidence for the necessity of on-site ringdown measurements. Meanwhile, the test run for low transmission mirrors was consistent with our targets for  $T$  and  $l$ , and so the final coating run replicated this design.

After the completion of the final coating runs, I characterized the mirrors before they were coned. One unfortunate fact of the final high transmission coating was an unusual number of large defects at 200x magnification, noticed by the technicians who first inspected the mirrors. The result was that while my best measurements indicated  $T = 15.5-16$  ppm and  $l = 1.5-2$  ppm, I also observed  $l$  as high as 5 ppm. On two different pairs of mirrors, I did a series of four or five different ringdown measurements, each time adjusting the beam position on the mirrors. Variation of loss across a single mirror pair was consistent with the 17-21 ppm variation I observed across different pairs, indicating that mirrors weren't wholly "good" or "bad"; rather, all mirrors had defects that needed to be avoided. REO technicians planned to use microscope inspection in order to cull the mirrors with the fewest number of defects for coning. In contrast, measured losses of the low transmission run were very consistent, in agreement with their defect-free appearance under the microscope. Measured total

coating run	superpolishing run	measured $T, l$
RN# L3-2029,L3-2030	5 cm: LT# IK838	$T = 15.5 - 16$ ppm
	10 cm: LT# IK716	$l = 1.4 - 1.7$ ppm
RN# L3-2034,L3-2039	5 cm: LT# IK839	$T = 0.1 - 0.2$ ppm
	10 cm: LT# IK840	$l = 1.4 - 1.7$ ppm

Table 7.1: Measured transmission and losses for coating and superpolishing runs at REO, April 2005

losses of 1.6–1.8 ppm along with inferred transmission  $T = 0.1$ – $0.2$  ppm (consistent with spectrophotometer data) suggested that  $S + A = 1.4$ – $1.7$  ppm.

The REO machinist struggled with the coning process, and only about a third of the mirrors weren't visibly damaged afterwards. In her thesis, Christina Hood speculated about possible damage to the mirror coatings from the machining process [21], but I found that the surviving mirrors had not experienced any measurable degradation in finesse. Moreover, for the high transmission set, the large number of mirrors initially coated allowed enough coned ones to be produced with no major defects in the central millimeter. I was able to select ten high- and low-transmission 5 cm ROC mirrors which met our ringdown standards, and the 10 cm mirrors were then chosen by microscope inspection. Table 7.1 lists the coating and superpolishing run numbers for these mirrors.

During my 2005 visits, I emphasized our hope to push the scattering and absorption losses to new lows. There was certainly interest in this project among the metrology staff and coating engineers, who were curious to understand whether minimum losses were dominated by scattering or by absorption. In their opinion, the primary suspect was absorption: while scattering decreases with better superpolishing of the substrates, they doubted that there was further room for improvement in that direction. Absorption, on the other hand, may be due to impurities in the metal targets inside the ion beam sputtering chamber, or sputtering of the chamber surfaces at the edges of the ion beam target.

In the following months, Sam Richman undertook a series of experiments at REO to explore the possibility of loss reduction. Test parameters included the use of different coating materials, sputtering chambers, and deposition settings. Mirrors were

coated at both 1064 nm and 633 nm, two wavelengths at which in-house characterization is straightforward. If the results of these experiments were promising, he hoped to proceed with an 852 nm coating run which we could then characterize ourselves. However, Sam was unfortunately not able to see any significant improvements in mirror losses.

### 7.3.2 ATF

In addition to our order for mirror coating and coning, we were also able to purchase superpolished substrates from REO which we could provide to Ramin Lalezari at ATF. The 5 cm and 10 cm ROC substrates were from the same batches (IK716, IK838, IK839, IK840) as those coated at REO. Ramin would then undertake a series of five coating runs using these substrates, again hoping to minimize scattering and absorption. This project included constructing new tooling for holding the substrates, which he hoped would minimize point defects during coating.

In early August of 2005, I returned to Colorado for ringdown measurements at ATF. The first test run had been completed just before my arrival and had a target transmission of 5 ppm, though in fact total losses were found to be only 5–5.5 ppm and rough partitioning of transmission and reflection suggested  $T \sim 2.9$  ppm,  $S + A \sim 2.3$  ppm. The second coating run took place while I was there and had a target transmission of 0.6 ppm, but total losses per mirror were 2.9–3.2 ppm, and partitioning suggested  $T \sim 0.3$  ppm,  $S + A \sim 2.6$  ppm. (The measured transmissions for the two runs were self-consistent; that is, if  $T$  were in fact 3 ppm instead of 5 for the first run, then we would expect the transmission for the second run also to be around half of its target value.)

A third coating run in September 2005 included superpolished substrates purchased from General Optics to compare with those from REO. However, both substrate types from this run had total losses of approximately 3 ppm, no better than the mirrors from the second run.

As Ramin and his colleagues had exhausted their ideas for reducing losses, the

project remained on hold until late 2006. At that time, ATF had made recent progress on mirror losses at other wavelengths by reducing contaminants in the coating film due to parts of the chamber being sputtered. Ramin hoped that they could apply what they had learned to a new coating run, which took place in January 2007. Dal and I both traveled to Longmont, where we set up the new test apparatus (Section 7.2.3) and discussed possible approaches to mirror coning with Ramin and Jeff. The mirrors from this run were found to have  $L \approx 2.7$  ppm, or  $l = 2.2$  ppm incorporating estimated transmission and air losses. These mirrors were later re-annealed at 500 C, but with no measurable improvements.

Finally, a fifth run in March 2007 used a higher purity SiO<sub>2</sub> target within the coating chamber. This batch was noticeably cleaner than past runs under microscope inspection, and both Ramin's initial measurements and subsequent tests here at Caltech confirmed that  $l = 1.7$ – $1.9$  ppm. For the first time, the ATF coatings demonstrated losses as low as those measured at REO. However, spectrophotometer data indicates that the mirrors from this run are not as reflective at 936 nm as we would need to support a FORT, so in order to obtain suitable cavity mirrors, a new low-transmission coating run would be required, as well as a corresponding high-transmission run.

ATF does not have the capabilities to cone these mirrors down to the tapered 3 mm / 1 mm dimensions which we have used in the past. With assistance from Ramin, Dal has been pursuing some promising options for having this machining done by a third party.

## 7.4 Single-sided cavity calculations

Given the effort put into mirror development, it is worth considering quantitatively what impact these new mirrors could have on our experiments. One important benchmark is the probability that a photon generated within a cavity will be transmitted

by the “open” (high-transmission) mirror. This is given by

$$P_{trans} = \frac{T_o}{T_c + T_o + 2l}, \quad (7.5)$$

where  $T_o$  and  $T_c$  are transmission through the “open” and “closed” mirrors, respectively. For the current lab 11 cavity,  $T_o = T_c = 4.3$  ppm,  $l = 2.9$  ppm, and  $P_{trans} = 0.30$  [42]. This constitutes the most significant loss in our output detection path. If, instead,  $T_o = 15.5$  ppm,  $T_c = 0.1$  ppm, and  $l = 1.5$  ppm, based on the REO coating run measurements, then  $P_{trans} = 0.83$ , a nearly threefold improvement. This transmission probability also governs the reverse process, that is, the acceptance of a resonant photon into the cavity by a STIRAP process [31].<sup>1</sup> Thus, in order to improve the efficiency of the coherent state transfer process described in Chapter 3, and especially for future experiments in which a photon extracted from one cavity is mapped into another (or the same) cavity, a single-sided cavity using currently available mirrors would be very useful.

More problematic is the question of experiments which rely on reflecting a photon back from the cavity input. For example, Ref. [44] describes a reflection-based scheme for QND measurement of photon number: an atom with ground states  $|a\rangle$ ,  $|b\rangle$  and excited state  $|e\rangle$  within an optical cavity is prepared in a superposition of the two ground states, and the cavity is tuned to the  $|b\rangle \rightarrow |e\rangle$  transition. If a photon resonant with this transition is sent to the cavity, then it can be detected afterwards by a rotation on the atom followed by measurement in the basis  $\{|a\rangle, |b\rangle\}$ . This can be seen by considering the two ground state cases separately; the photon causes a phase flip only if the atom is in  $|a\rangle$ :

$$|a\rangle \rightarrow -|a\rangle \quad (7.6)$$

$$|b\rangle \rightarrow |b\rangle, \quad (7.7)$$

---

<sup>1</sup>One might imagine that only the ratio of  $T$  to  $l$  at the photon input port need be considered. However, by a time-reversal symmetry argument, both ports must be taken into account, since the cavity can emit photons through either mirror. Thus, in order to map photons efficiently into a symmetric cavity, both mirrors would ideally be used as inputs. A single-sided cavity allows us instead to use just one mirror.

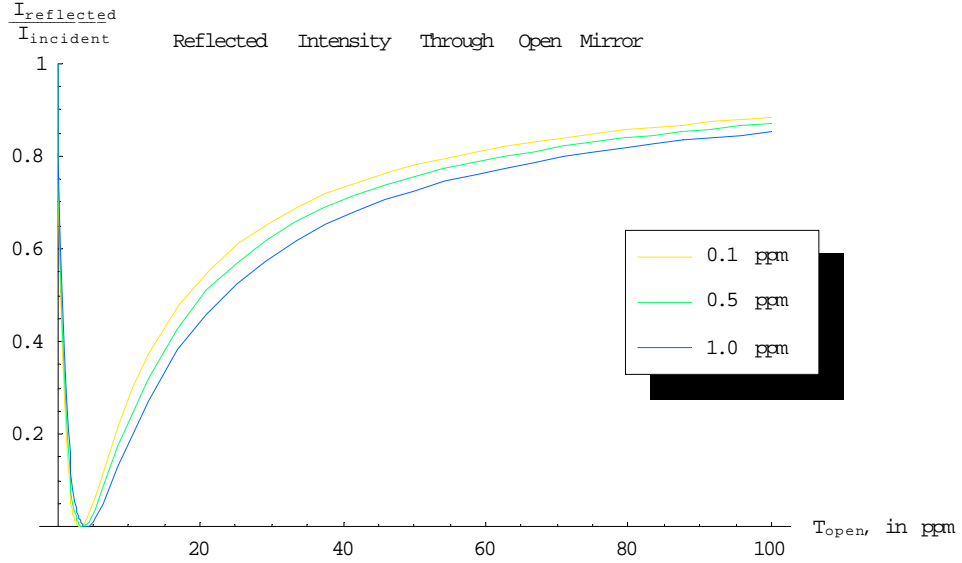


Figure 7.3: Fraction of incident intensity that is reflected from the transmissive mirror of an asymmetric cavity. Here both mirrors are assigned scattering and absorption losses  $l = 1.5$  ppm, and  $T_o$  is plotted from 0 to 100 ppm for three values of  $T_c$ : 0.1 ppm, 0.5 ppm, and 1.0 ppm.

so that  $|b\rangle + |a\rangle$  is mapped to  $|b\rangle - |a\rangle$  only in the presence of a photon. A  $\pi/2$  rotation subsequently maps

$$|b\rangle + |a\rangle \rightarrow |b\rangle \quad (7.8)$$

$$|b\rangle - |a\rangle \rightarrow |a\rangle, \quad (7.9)$$

two orthogonal states which can be distinguished quickly and efficiently via state detection with a probe laser. [30]

For lossy mirrors, however, the probability that a resonant photon is reflected from an empty cavity (that is, when the atom is in  $|0\rangle$ , dark to the cavity transition) is given by

$$P_{refl} = \left( \frac{T_c - T_o + 2l}{T_c + T_o + 2l} \right)^2. \quad (7.10)$$

This function has a minimum at zero when the impedance-matching condition  $T_o = T_c + 2l$  is satisfied. It is plotted in Figure 7.4 as a function of open mirror transmission for  $l = 1.5$  ppm,  $T_c = \{0.1, 0.5, 1\}$  ppm. We see that for our target transmission,

$T_o = 15$  ppm, only about 40% of the incident light is reflected. In the QND scheme, a photon would always reflect when the atom was in  $|b\rangle$ , but would be lost more than half the time when the atom was in  $|a\rangle$ .

We could, of course, increase the transmission of the open mirror to improve the reflection efficiency. The problem is the corresponding decline in cavity finesse and increase in  $\kappa$ ; we gradually move out of the strong coupling regime. The QND protocol requires strong coupling so that photons coupled to the  $|b\rangle \rightarrow |e\rangle$  transition are completely off-resonant when an atom in  $|b\rangle$  is present in the cavity. In this case, the loss of strong coupling would mean a state-dependent phase shift less than  $\pi$  and nonorthogonal final atomic states.

## 7.5 Outlook

Unfortunately, neither REO nor ATF have been able to produce mirrors with losses smaller than those of the 1991 supermirror run [8]. However, at this point, both companies have the capability to produce mirrors with  $l < 2$  ppm and a more thorough understanding of what contributes to loss in their facilities. When the coning process is successful, it seems to have no measurable effect on cavity finesse, and by outsourcing the coning to a skilled glass machinist, we may be able to avoid losing mirrors in the process. Using a simple new technique for cavity ringdown, we are now able to characterize mirrors quickly and reliably, with possible extensions to loss partitioning.

# Bibliography

- [1] P. Zoller et al., *Eur. Phys. J. D* **36**, 203 (2005).
- [2] J. I. Cirac, P. Zoller, H. J. Kimble, and H. Mabuchi, *Phys. Rev. Lett.* **78**, 3221 (1997).
- [3] E. T. Jaynes and F. W. Cummings, *Proc. IEEE* **51**, 89 (1963).
- [4] K. M. Birnbaum, *Cavity QED with multilevel atoms*, PhD thesis, California Institute of Technology, Pasadena, CA, 2005.
- [5] K. M. Birnbaum, A. S. Parkins, and H. J. Kimble, *Phys. Rev. A* **74**, 063802 (2006).
- [6] H. Carmichael, *An Open Systems Approach to Quantum Optics*, Springer, 1993.
- [7] R. J. Thompson, G. Rempe, and H. J. Kimble, *Phys. Rev. Lett.* **68**, 1132 (1992).
- [8] G. Rempe, R. J. Thompson, H. J. Kimble, and R. Lalezari, *Opt. Lett.* **17**, 363 (1992).
- [9] A. E. Siegman, *Lasers*, University Science Books, Sausalito, CA, 1986.
- [10] H. J. Metcalf and P. van der Straten, *Laser Cooling and Trapping*, Springer, 2nd edition, 2001.
- [11] H. Mabuchi, Q. A. Turchette, M. S. Chapman, and H. J. Kimble, *Opt. Lett.* **21**, 1393 (1996).
- [12] J. Ye, D. W. Vernooy, and H. J. Kimble, *Phys. Rev. Lett.* **83**, 4987 (1999).

- [13] J. McKeever et al., Phys. Rev. Lett. **90**, 133602 (2003).
- [14] J. McKeever, A. Boca, A. D. Boozer, J. R. Buck, and H. J. Kimble, Nature **425** (2003).
- [15] A. D. Boozer, A. Boca, J. R. Buck, J. McKeever, and H. J. Kimble, Phys. Rev. A **70** (2004).
- [16] J. McKeever et al., Science **303**, 1992 (2004).
- [17] A. Boca et al., Phys. Rev. Lett. **93**, 233603 (2004).
- [18] J. McKeever, J. R. Buck, A. D. Boozer, and H. J. Kimble, Phys. Rev. Lett. **93**, 143601 (2004).
- [19] A. D. Boozer, *Raman transitions in cavity QED*, PhD thesis, California Institute of Technology, Pasadena, CA, 2005.
- [20] C. J. Hood, T. W. Lynn, A. C. Doherty, A. S. Parkins, and H. J. Kimble, Science **287**, 1447 (2000).
- [21] C. J. Hood, *Real-time measurement and trapping of single atoms by single photons*, PhD thesis, California Institute of Technology, Pasadena, CA, 2000.
- [22] T. W. Lynn, *Measurement and control of individual quanta in cavity QED*, PhD thesis, California Institute of Technology, Pasadena, CA, 2003.
- [23] T. W. Lynn, K. Birnbaum, and H. J. Kimble, J. Opt. B: Quantum Semiclass. Opt. **7**, S215 (2005).
- [24] L. Tian and H. J. Carmichael, Phys. Rev. A **46**, R6801 (1992).
- [25] S. Rebić, S. M. Tan, A. S. Parkins, and D. F. Walls, J. Opt. B: Quant. Semiclass. Opt. **1**, 490 (1999).
- [26] S. Rebić, A. S. Parkins, and S. M. Tan, Phys. Rev. A **65**, 043806 (2002).
- [27] S. Rebić, A. S. Parkins, and S. M. Tan, Phys. Rev. A **65**, 063804 (2002).

- [28] K. M. Birnbaum et al., *Nature* **436**, 87 (2005).
- [29] A. Boca, *Experiments in cavity QED: Exploring the interaction of quantized light with a single trapped atom*, PhD thesis, California Institute of Technology, Pasadena, CA, 2005.
- [30] A. D. Boozer, A. Boca, R. Miller, T. E. Northup, and H. J. Kimble, *Phys. Rev. Lett.* **97**, 083602 (2006).
- [31] A. D. Boozer, A. Boca, R. Miller, T. E. Northup, and H. J. Kimble, *Phys. Rev. Lett.* **98**, 193601 (2007).
- [32] A. D. Boozer, R. Miller, T. E. Northup, A. Boca, and H. J. Kimble, *Phys. Rev. A* **76**, 063401 (2007).
- [33] C. Monroe et al., *Phys. Rev. Lett.* **75**, 4011 (1995).
- [34] D. Leibfried, R. Blatt, C. Monroe, and D. Wineland, *Rev. Mod. Phys.* **75**, 281 (2003).
- [35] S. E. Hamann et al., *Phys. Rev. Lett.* **80**, 4149 (1998).
- [36] H. Perrin, A. Kuhn, I. Bouchoule, and C. Salomon, *Europhys. Lett.* **42**, 395 (1998).
- [37] V. Vuletić, C. Chin, A. J. Kerman, and S. Chu, *Phys. Rev. Lett.* **81**, 5768 (1998).
- [38] A. D. Boozer, (in preparation).
- [39] J. McKeever, *Trapped atoms in cavity QED for quantum optics and quantum information*, PhD thesis, California Institute of Technology, Pasadena, CA, 2004.
- [40] D. W. Vernooy, *Cold atoms in cavity QED for quantum information processing*, PhD thesis, California Institute of Technology, Pasadena, CA, 2000.

- [41] R. W. P. Drever et al., *Appl. Phys. B* **31**, 97 (1983).
- [42] C. J. Hood, H. J. Kimble, and J. Ye, *Phys. Rev. A* **64**, 033804 (2001).
- [43] T. Pellizzari, S. A. Gardiner, J. I. Cirac, and P. Zoller, *Phys. Rev. Lett.* **75**, 3788 (1995).
- [44] L.-M. Duan and H. J. Kimble, *Phys. Rev. Lett.* **92**, 127902 (2004).
- [45] H.-J. Briegel, *The Physics of Quantum Information: Quantum Cryptography, Quantum Teleportation, Quantum Computation*, chapter 6.2, pages 192–197, Springer, Berlin, 2000.
- [46] P. Maunz et al., *Nature* **428**, 50 (2004).
- [47] J. A. Sauer, K. M. Fortier, M. S. Chang, C. D. Hamley, and M. S. Chapman, *Phys. Rev. A* **69**, 051804 (2004).
- [48] S. Nußmann et al., *Nature Physics* **1**, 122 (2005).
- [49] R. Miller et al., *Journal of Physics B: Atomic, Molecular and Optical Physics* **38**, S551 (2005).
- [50] G. R. Guthöhrlein, M. Keller, K. Hayasaka, W. Lange, and H. Walther, *Nature* **414**, 49 (2001).
- [51] A. B. Mundt et al., *Phys. Rev. Lett.* **89**, 103001 (2002).
- [52] B.-G. Englert, J. Schwinger, A. O. Barut, and M. O. Scully, *Europhys. Lett.* **14**, 25 (1991).
- [53] S. Haroche, M. Brune, and J. M. Raimond, *Europhys. Lett.* **14**, 19 (1991).
- [54] M. J. Holland, D. F. Walls, and P. Zoller, *Phys. Rev. Lett.* **67**, 1716 (1991).
- [55] P. Storey, M. Collett, and D. Walls, *Phys. Rev. Lett.* **68**, 472 (1992).
- [56] R. Quadt, M. Collett, and D. F. Walls, *Phys. Rev. Lett.* **74**, 351 (1995).

- [57] A. M. Herkommer, V. M. Akulin, and W. P. Schleich, *Phys. Rev. Lett.* **69**, 3298 (1992).
- [58] A. M. Herkommer, H. J. Carmichael, and W. P. Schleich, *Quantum and Semi-classical Optics: Journal of the European Optical Society Part B* **8**, 189 (1996).
- [59] W. Ren and H. J. Carmichael, *Phys. Rev. A* **51**, 752 (1995).
- [60] M. O. Scully, G. M. Meyer, and H. Walther, *Phys. Rev. Lett.* **76**, 4144 (1996).
- [61] D. W. Vernooy and H. J. Kimble, *Phys. Rev. A* **55**, 1239 (1997).
- [62] D. W. Vernooy and H. J. Kimble, *Phys. Rev. A* **56**, 4287 (1997).
- [63] A. C. Doherty, A. S. Parkins, S. M. Tan, and D. F. Walls, *Phys. Rev. A* **57**, 4804 (1998).
- [64] A. S. Parkins and H. J. Kimble, *J. Opt. B: Quantum Semiclass. Opt.* **1**, 496 (1999).
- [65] A. S. Parkins and H. J. Kimble, Teleporting an atomic wavepacket, in *Frontiers of Laser Physics and Quantum Optics: Proceedings of the International Conference on Laser Physics and Quantum Optics*, edited by Z. Hu, S. Xie, S.-Y. Zhu, and M. O. Scully, page 321, Springer, 2000.
- [66] A. S. Parkins and H. J. Kimble, *Phys. Rev. A* **61**, 052104 (2000).
- [67] D. Boiron et al., *Phys. Rev. A* **53**, R3734 (1996).
- [68] W. Alt et al., *Phys. Rev. A* **67**, 033403 (2003).
- [69] A. C. Doherty and K. Jacobs, *Phys. Rev. A* **60**, 2700 (1999).
- [70] C. H. Bennett, *Phys. Today* **48**, 24 (1995).
- [71] A. K. Ekert, *Phys. Rev. Lett.* **67**, 661 (1991).
- [72] V. Giovannetti, S. Lloyd, and L. Maccone, *Science* **306**, 1330 (2004).

- [73] H.-J. Briegel, W. Dür, J. I. Cirac, and P. Zoller, *Phys. Rev. Lett.* **81**, 5932 (1998).
- [74] J. Oreg, F. T. Hioe, and J. H. Eberly, *Phys. Rev. A* **29**, 690 (1984).
- [75] J. R. Kuklinski, U. Gaubatz, F. T. Hioe, and K. Bergmann, *Phys. Rev. A* **40**, 6741 (1989).
- [76] A. S. Parkins, P. Marte, P. Zoller, and H. J. Kimble, *Phys. Rev. Lett.* **71**, 3095 (1993).
- [77] N. V. Vitanov, M. Fleischhauer, B. Shore, and K. Bergmann, Coherent manipulation of atoms and molecules by sequential laser pulses, in *Advances in Atomic, Molecular, and Optical Physics*, volume 46, pages 55–190, Academic Press, 2001.
- [78] L.-M. Duan and H. J. Kimble, *Phys. Rev. Lett.* **90**, 253601 (2003).
- [79] M. Keller, B. Lange, K. Hayasaka, W. Lange, and H. Walther, *Nature* **431**, 1075 (2004).
- [80] M. Hijlkema et al., *Nature Physics* **3**, 253 (2007).
- [81] P. Grangier, B. Sanders, and J. Vuckovic, *New Journal of Physics* **6** (2004).
- [82] T. Wilk, S. C. Webster, H. P. Specht, G. Rempe, and A. Kuhn, *Phys. Rev. Lett.* **98**, 063601 (2007).
- [83] T. Wilk, S. C. Webster, A. Kuhn, and G. Rempe, *Science* **317**, 488 (2007).
- [84] T. G. Walker and W. Happer, *Rev. Mod. Phys.* **69**, 629 (1997).
- [85] D. Budker et al., *Rev. Mod. Phys.* **74**, 1153 (2002).
- [86] C. Audoin, *Metrologia* **29**, 113 (1992).
- [87] J. Laurat, K. S. Choi, H. Deng, C. W. Chou, and H. J. Kimble, *Phys. Rev. Lett.* **99**, 180504 (2007).

- [88] C.-W. Chou et al., *Science* **316**, 1316 (2007).
- [89] A. Kastler, Nobel Prize Lecture, 1966.
- [90] W. Demtröder, *Laser Spectroscopy: Basic Concepts and Instrumentation*, chapter 10, pages 567–608, Springer-Verlag, Berlin, 1982.
- [91] W. Happer, *Rev. Mod. Phys.* **44**, 169 (1972).
- [92] L. S. Cutler, United States Patent 4,425,653, 1980.
- [93] B. Wang et al., *Phys. Rev. A* **75**, 051801 (2007).
- [94] D. J. Wineland et al., *Royal Society of London Philosophical Transactions Series A* **361**, 1349 (2003).
- [95] P. Cladé et al., *Phys. Rev. Lett.* **96**, 033001 (2006).
- [96] T. L. Gustavson, P. Bouyer, and M. A. Kasevich, *Phys. Rev. Lett.* **78**, 2046 (1997).
- [97] I. Dotsenko et al., *Applied Physics B: Lasers and Optics* **78**, 711 (2004).
- [98] M. H. Anderson et al., *Phys. Rev. Lett.* **64**, 1346 (1990).
- [99] K. P. Dinse, M. P. Winters, and J. L. Hall, *J. Opt. Soc. Am. B* **5**, 1825 (1988).
- [100] S. Lathi, S. Kasapi, and Y. Yamamoto, *Opt. Lett.* **21**, 1600 (1996).
- [101] T. Yabuzaki, T. Mitsui, and U. Tanaka, *Phys. Rev. Lett.* **67**, 2453 (1991).
- [102] J. R. Buck, Jr., *Cavity QED in microsphere and Fabry-Perot cavities*, PhD thesis, California Institute of Technology, Pasadena, CA, 2003.
- [103] S. J. van Enk, N. Lutkenhaus, and H. J. Kimble, *Phys. Rev. A* **75**, 052318 (2007).
- [104] L. Allen and J. H. Eberly, *Optical Resonance and Two-Level Atoms*, Dover, New York, 1987.

- [105] Y. S. Au, *Birefringent Cavity for CQED*, Undergraduate thesis, California Institute of Technology, Pasadena, CA, 2006.
- [106] A. Öttl, S. Ritter, M. Köhl, and T. Esslinger, *Rev. Sci. Inst.* **77**, 063118 (2006).
- [107] W. Wohlleben, F. Chevy, K. Madison, and J. Dalibard, *Eur. Phys. J. D* **15**, 237 (2001).
- [108] J. A. Sauer, *Cold atom manipulation for quantum computing and control*, PhD thesis, Georgia Institute of Technology, 2004.
- [109] K. Fortier, personal communication, 2005.
- [110] S. T. Bannerman, *Vibration isolation for cavity quantum electrodynamics*, Undergraduate thesis, California Institute of Technology, Pasadena, CA, 2006.
- [111] A. Takamori et al., *Classical and Quantum Gravity* **19**, 1615 (2002).
- [112] C. Wieman, G. Flowers, and S. Gilbert, *Am. J. Phys.* **63**, 317 (1995).
- [113] J. Fortagh, A. Grossmann, T. W. Hänsch, and C. Zimmermann, *Journal of Applied Physics* **84**, 6499 (1998).
- [114] P. della Porta, C. Emili, and S. J. Hellier, *Alkali metal generation and gas evolution from alkali metal dispensers*, Technical report, IEEE Conference on Tube Techniques, New York, 1968.
- [115] L. Cattaneo, C. Maeda, and R. Petersen, *Alkamax application note vol. 1*, Technical report, SAES Getters, 2004.
- [116] J.-P. Bacher et al., *Journal of Vacuum Science and Technology A: Vacuum, Surfaces, and Films* **21**, 167 (2003).
- [117] G. Li et al., *Appl. Opt.* **45**, 7628 (2006).
- [118] D. Berns, personal communication, 2004.
- [119] S. Richman, personal communication, 2006.

- [120] B. Dahmani, L. Hollberg, and R. Drullinger, *Opt. Lett.* **12**, 876 (1987).
- [121] C. E. Tanner, B. P. Masterson, and C. E. Wieman, *Opt. Lett.* **13**, 357 (1988).
- [122] D. A. King and R. J. Pittaro, *Opt. Lett.* **23**, 774 (1998).
- [123] P. W. Milonni and J. H. Eberly, *Lasers*, John Wiley and Sons, 1988.
- [124] J. A. Stone and J. H. Zimmerman, *Engineering Metrology Toolbox*,  
<http://emtoolbox.nist.gov/Wavelength/Documentation.asp>.